# Emerging Circularly Polarized Luminescence and Circular Dichroism from Achiral Oligo- and Polyfluorenes Endowed with Helicity and Chirality of Soluble Cellulose Derivatives

（可溶性セルロース誘導体によって付与されたアキラルな
オリゴ/ポリフルオレンの円偏光発光と円二色性の発生）

**Guo Sibo**

**郭　思博**

**Nara Institute of Science and Technology**

**Graduate School of Materials Science**

**Advanced Polymer Science Laboratory**

**(Prof. Fujiki Michiya)**

**2017**

## Index

**CHAPTER 1. GENERAL INTRODUCTION ..... 1**

1.1 Materials with Helical Structure ..... 1

1.2 Optical Activity Transfer ..... 4

1.3 Polysaccharides and Cellulose ..... 7

1.4 Molecular Twist in Polyfluorene ..... 9

1.5 Purpose of This Research ..... 12

1.6 References ..... 13

**CHAPTER 2. EXPERIMENTAL DETAILS AND MATERIALS USED IN THIS THESIS ..... 16**

2.1 Cellulose Triacetate (**CTA**), Cellulose Acetate Butyrate (**CABu**), and Cellulose Triphenyl Carbamate (**CTPC**) ..... 16

2.2 9,9-Dialkylfluorene (FL) Oligomers and Polymers ..... 18

**2.3 HYBRID FILMS OF SOLUBLE CELLULOSES WITH DIALKYLFLUORENE DERIVATIVES ..... 19**

2.4 Characterization ..... 21

2.4.1 Circular Dichroism (CD), UV-visible, Circularly Polarized Luminescence (CPL), and Photoluminescence (PL) Spectra ..... 21

2.4.2 One-Dimensional (1D) and Two-Dimensional (2D) A (FT) Nuclear Magnetic Resonance (NMR) Spectra ..... 21

2.4.3 FT-Infrared (FT-IR) Spectra ..... 21

2.4.4 Wide-Angle X-ray Diffraction (WAXD) ..... 22

2.4.5 Computational Modeling and Calculations ..... 22

2.4.6 Differential scanning calorimetry (DSC) ..... 22

2.5 References ..... 23

**CHAPTER 3. CHIRALITY TRANSFER EXPERIMENTS FROM CELLULOSE ALKYL ESTERS ..... 24**

3.1 CD Inversion Capability of **CTA** and **CABu** ..... 24

3.2 From **CTA** to FL Oligomers and Polymers ..... 25

3.3 From **CABu** to FL Oligomers and Polymers ..... 28

3.4 Chirality Transfer Capability as a Function of FL Repeating Unit ..... 31

3.5 Photoinduced racemization Capability as a Function of FL Repeating Unit ..... 34

3.6 Effect of Ester Groups on Chiral Transfer ..... 36

3.7 References ..... 37

**CHAPTER 4. CHIRALITY TRANSFER EXPERIMENTS FROM CELLULOSE TRIPHENYL**

**CARBAMATE** ..... **38**
4.1 Divergence of CD Spectra of **CTPC** in THF and $CH_2Cl_2$ ..... 38
4.2 Solvent-Driven CD Inversion Capability of **CTPC** ..... 39
4.3 Solvent-Driven CPL Inversion Capability of **CTPC** ..... 41
4.4 Chirality Transfer Capability as a Function of Fluorene Repeating Unit ..... 43
4.5 Solvent Dependent Chirality Transfer Capability of **CTPC** ..... 45
4.6 References ..... 46

**CHAPTER 5. MECHANISTIC ASPECTS OF CHIRALITY TRANSFER CAPABILITY** ..... **47**
5.1 Intermolecular Interactions between **CTA/CABu** and Fluorene Derivatives ..... 47
5.1.1 Polysaccharide Helicity Transfer versus Glucose Chirality Transfer ..... 47
5.1.2 WAXD Analysis of **CTA** and **CABu** Films ..... 49
5.1.3 The Origin of Bisignate CD Band as an Evidence of Twisted Fluorene Main-Chain ..... 50
5.1.4 C-H/O=C Interactions between Dioctylfluorene Oligomer and **CTA** by Computer Modeling ..... 56
5.1.5 1D-/2D-NMR for Intermolecular C-H/O=C Interactions ..... 59
5.2 Inter- and Intramolecular Interactions of **CTPC** and Fluorene Systems ..... 63
5.2.1 Side-Chain Dependence of **CTPC** ..... 63
5.2.2 WAXD Analysis for Intermolecular Interactions ..... 65
5.2.3 DSC Analysis for NH/O=C Interactions ..... 66
5.2.4 Solubility for Side-Chain Dependence of **CTPC** ..... 68
5.2.5 Computer-Assisted Modeling of **CTPC** and Oligofluorene ..... 69
5.3 Reference ..... 74

**CHAPTER 6. CONCLUDING REMARKS** ..... **76**

**APPENDIX** ..... **78**

**LIST OF PUBLICATIONS AND CONFERENCES** ..... **115**

**PRESENTED WORKS** ..... **116**

**ACKNOWLEDGEMENTS** ..... **117**

## Chapter 1. General Introduction

### 1.1 Materials with Helical Structure

Helical structures, which use chiral reactants and have twistability, are often found in natural molecules,[1] oligomers,[2] polymers,[3] and supramolecules[4] and play important roles in recognition functions,[4] optical amplifiers,[5] and autocatalytic reactions.[6] For instance, the right-handed double helix of DNA[7] is known to show the transition from a β-helix to a right-handed α-helix for proteins[8]. The biological helical units assemble to set up supramolecular helical structures.[9] For a long time, researchers have conducted many studies to develop a large variety of helical molecules, oligomers, and polymers. Remarkable developments have been made during the past few decades.

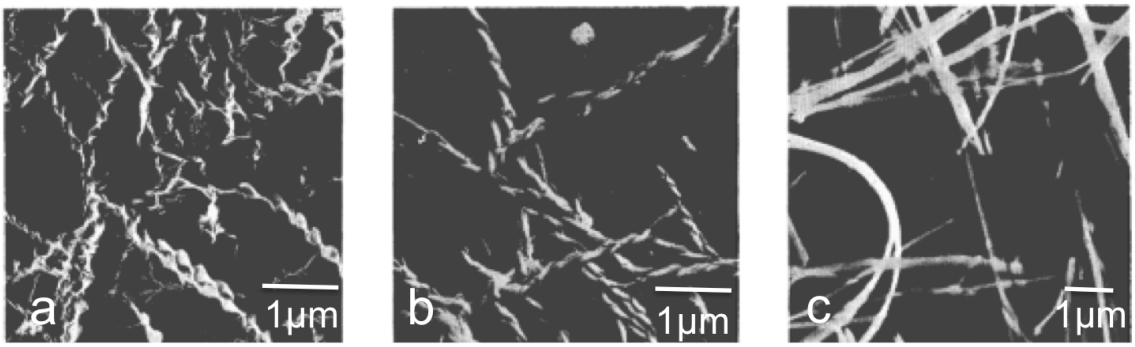


**Figure 1.1.** Scanning electron microscopy (SEM) images of self-assembled helices (a and b) and flat ribbons (c) of lithium 12-hydroxystearate. (Reproduced with permission from Tachibana, T.; Kambara, H. Enantiomorphism in the Helical Aggregate of Lithium 12-Hydroxystearate. *J. Am. Chem. Soc.,* **1965**, *87*, 3015−3016. Copyright 1965 American Chemical Society.)

In 1965, Tachibana and Kambara noted for the first time the helical handedness and direction of lithium 12-hydroxystearate assemblies.[10] They used the enantiomers and racemate and found that the D- and L-forms of the conformations transformed into right- and left-handed fibers and that no helical conformations formed from the racemate (Figure 1.1).

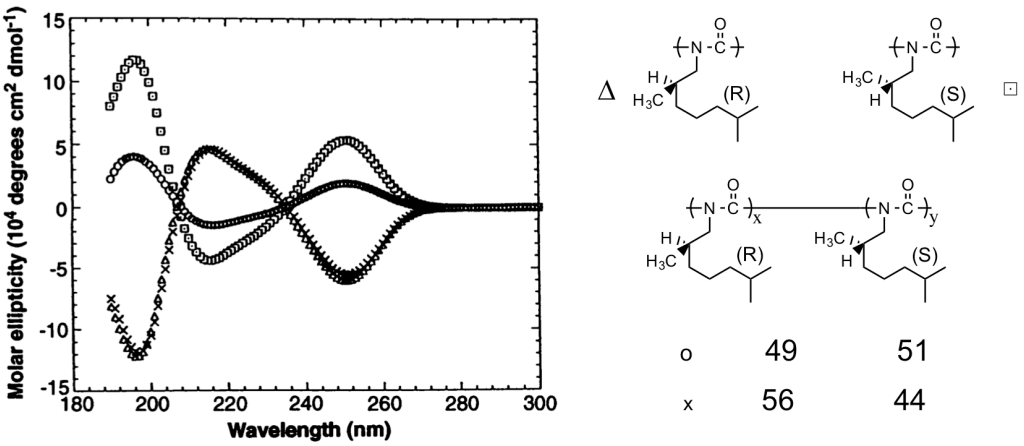


**Figure 1.2.** Circular dichroism (CD) spectra of the homopolymers and copolymers of (R)- and (S)-2,6-dimethylheptyl isocyanates in hexane solution at room temperature plotted as the molar ellipticity against wavelength. (Reproduced with permission from Green, M. M.; Garetz, B. A.; Munoz, B.; Chang, H.; Hoke, S.; Cooks, R. G. Majority rules in the copolymerization of mirror image isomers. *J. Am. Chem. Soc.,* **1995**, *117*, 4181-4182. Copyright 1995 American Chemical Society.)

Green et al. observed the first example of a synthetic helical polymer system in 1988.[11] They discovered the excellent features of the dynamic helicity of polyisocyanates and that the right- and left-handed helical conformations were not interconvertible (Figure 1.2). The chirality was amplified in the dynamic helical polyisocyanates due to a small chiral bias between the monomer units; thus, these polymers produced large helix conformations.

Starting with these pioneering studies, the number of synthetic polymers with controlled helix conformations has decreased, and these polymers can be categorized into two types: static helical polymers and dynamic helical polymers.[12] Examples include poly(triphenylmethyl methacrylate) (**PTrMA**)[13] and polychloral;[14] the high steric repulsion between their bulky side groups is high enough to maintain their helical conformations. The static helical polymers can be synthesized using helix-selective polymerization of the monomers with chiral catalysts or initiators.

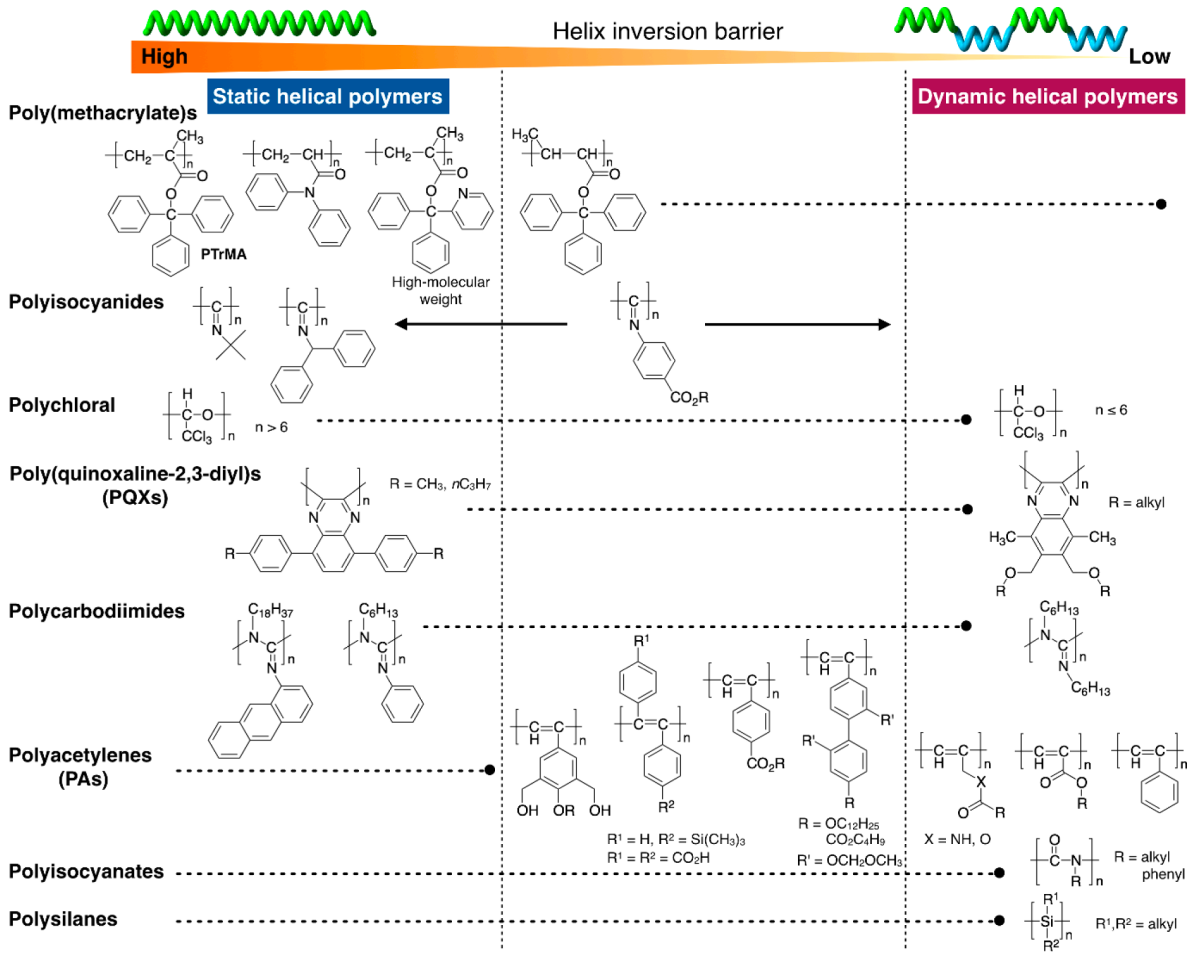


**Figure 1.3.** Representative examples of static and dynamic helical polymers that differ through their helix inversion barriers. (Reproduced with permission from Yashima, E.; Ousaka, N.; Taura, D.; Shimomura, K.; Ikai, T.; Maeda, K. Supramolecular Helical Systems: Helical Assemblies of Small Molecules, Foldamers, and Polymers with Chiral Amplification and Their Functions. *Chem. Rev.*, **2016**, *116*, 13752–13990. Copyright 2016 American Chemical Society.)

On the other hand, dynamic helical polymers can be transformed between the right- and left-helical conformations through the low helix inversion obstacle.[12] Therefore, specific lead units in the polymer chains can significantly amplify the helical characteristics through inter/intramolecular interactions.[15]

### 1.2 Optical Activity Transfer

When chirality is employed during the molecular assembly, it is possible to design a molecule with switchable optical activity due to chirality transfer.[16] The application of chirality transfer has been widely studied because it is simple and easy to operate and has the advantage of avoiding complicated syntheses,[17] which are used for optical and chiral materials with specific properties.[18] To absorb left and right circularly polarized light differently, such optical activity could be caused by a conformation change.[19]

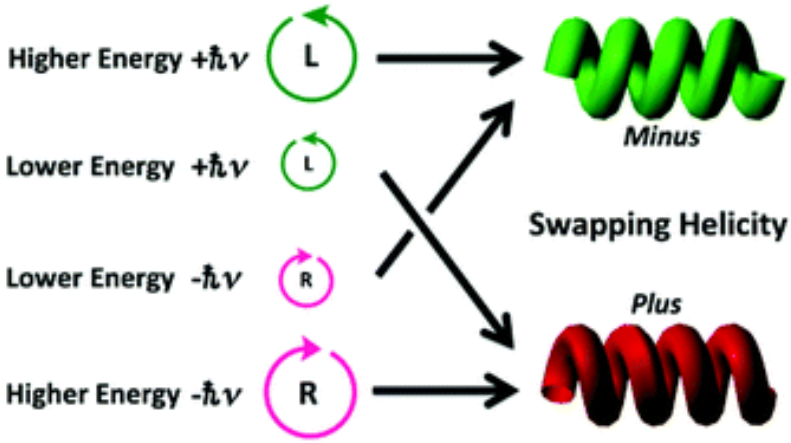


**Figure 1.4.** The choice of higher and lower circular polarized photon energies caused the signs to switch in the chiroptical polarization of the particles. (Reproduced with permission from Fujiki, M.; Donguri, Y.; Zhao, Y.; Nakao, A.; Suzuki, N.; Yoshida, K.; Zhang, W.Photon Magic: Chiroptical Polarisation, Depolarisation, Inversion, Retention and Switching of Non-Photochromic Light-Emitting Polymers in Optofluidic Medium. *Polym. Chem.*, **2015**, *6*, 1627-1638. Copyright 2015 The Royal Society of Chemistry.)

In 2015, Fujiki *et al.* employed circularly polarized (CP)-photon chirality transfer experiments with six different energies irradiated through poly[(9,9-di-*n*-octylfluoren-2,7-diyl)- *alt*-bithiophene] (**PF8T2**) as *m*m-sized polymeric assorted aggregates in chloroform–methanol cosolvents.[20] This approach revealed the capability of photophysically controlling the inversion, retention and switching of the ground and/or photoexcited states.

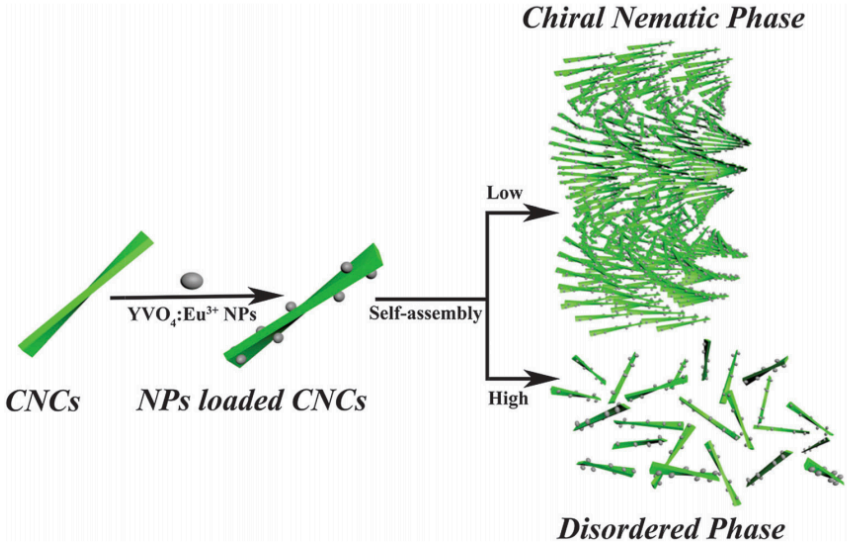


**Figure 1.5.** The form approach for CNC chiral rods and $YVO_4:Eu^{3+}$ NPs. (Reproduced with permission from Chu, G.; Wang, X.; Chen, T.; Xu, W.; Wang, Y.; Song, H.; Xu, Y. Chiral Electronic Transitions of $YVO_4:Eu^{3+}$ Nanoparticles in Cellulose-based Photonic Materials with Circularly Polarized Excitation. *J. Mater. Chem. C*, **2015**, *3*, 3384-3390. Copyright 2015 The Royal Society of Chemistry.)

In 2015, Xu et al. made a novel chiral nematic luminescent film using YVO4:$Eu^{3+}$ NPs attached to the surface of cellulose nanocrystals (CNCs) through hydrogen bonding and van der Waals interactions.[21] The hybrid film exhibited a CPL with a high $g_{CPL}$ value.

Recently, we demonstrated that non-charged rod-like helical polysilanes with *right*- and *left*-helix senses could become ultraviolet (UV) light-scissable helix scaffolding, allowing the instant generation of CD-active/CPL-active poly(di-*n*-octylfluorene) (**PF8**) as aggregates.[22] This result led us to propose that non-charged, non-polar CD-silent/CPL-silent oligomers and polymers may become CD-active/CPL-active after becoming embedded into polysaccharide films—even non-charged, less-polar polysaccharides carrying alkyl esters — through intermolecular attractive forces.

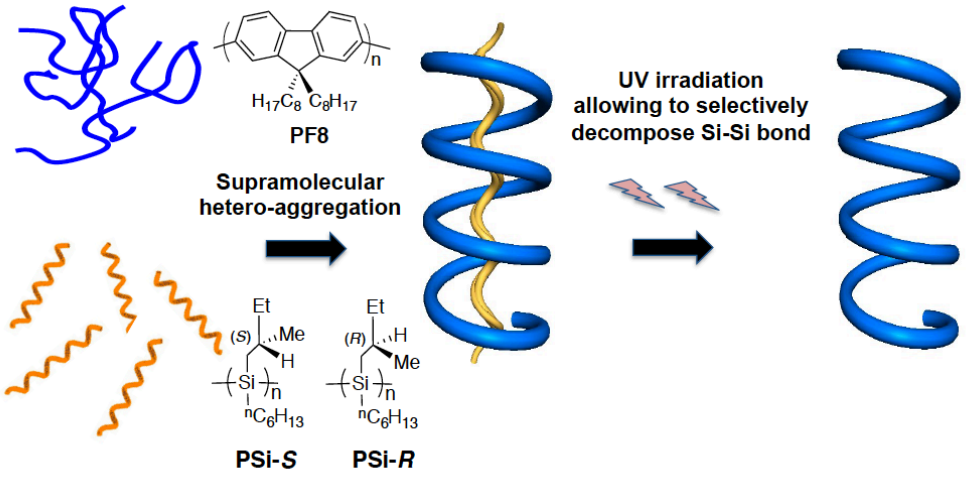


**Figure 1.6.** The preparation of CPL- and CD-active dioctylpolyfluorene using chiral polysilanes and removal due to a polysilane-selective photoscissoring reaction at 313 nm. (Reproduced with permission from Rahim, N. A. A.; Fujiki, M. Aggregation-Induced Scaffolding: Photoscissable Helical Polysilane Generates Circularly Polarized Luminescent Polyfluorene. *Polym. Chem.*, **2016**, *7*, 4618–4629. Copyright 2016 The Royal Society of Chemistry.)

Thus, the chirality transfer system has a wide range of applications for chiroptical photoswitching, signal amplification, displays and sensors. The mechanism of helical transfer is an important issue in not only theoretical research but also materials science and technology.

### 1.3 Polysaccharides and Cellulose

Polysaccharides are found in all plants and animals, which are an abundant organic compound on earth.[23] Most carbohydrates are produced in plants as structural components of cell walls and constitute important energy reserves for animals.[24] Polysaccharides are chains of carbohydrate units, which form in conformations from tens to thousands of units.[25] The characteristics of polysaccharides play important roles in the food, pharmaceutical, and textile industries and have very important structure functions.[26]

As a typical polysaccharide, cellulose is the basic structure in plant cells.[27] Cellulose is the most abundant renewable organic material on earth, which widely exists in plants, algae, fungi, and bacteria.[28] The properties of cellulose arise from its superior mechanical strength,[29] controllable surface chemistry,[30] and chirality.[21] However, it cannot be dissolved in water and general organic solvents due to its intra- and intermolecular hydrogen bonds (Figure 1.7).[31]

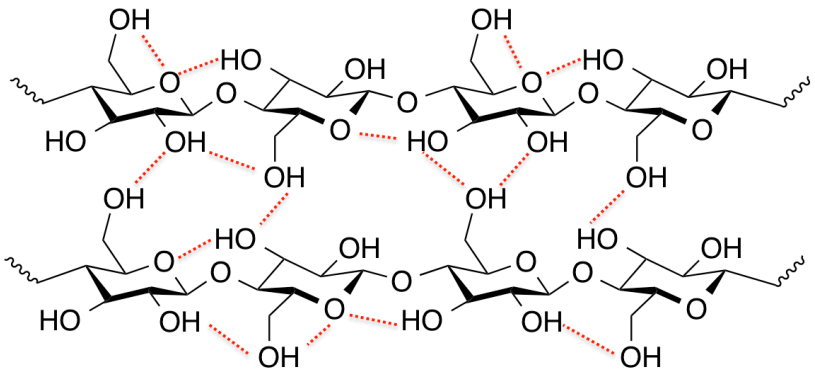


**Figure 1.7.** The intermolecular and intramolecular hydrogen bonds in cellulose.

A notable method of cellulose dissolution is the chemical modification of the side chains on the polymer.[32] The solubility of the cellulose derivatives depends on the type and degree of chemical modification, and most of the derivatives are soluble in general organic solvents, such as $CHCl_3$, DMSO, and THF, etc.[33] For example, cellulose triacetate (**CTA**), a cellulose derivative, is applied to the films and fibers in optical devices.[34] It is widely used in protective films for polarizing plates and liquid crystal displays for high transparency and low birefringence.[35]

Cellulose derivatives are also widely used in chiral stationary phases (CSPs).[36] For example, the phenylcarbamates of cellulose, synthesized by the modification of the

hydroxy groups with various phenyl isocyanates, have significant chiral recognition abilities.[37] In 1984, a CSP based on a natural polymer, cellulose triphenylcarbamate (**CTPC)**, was developed by Okamoto et al.[38] On the basis of the X-ray structural analysis[39] and the structure optimizations from molecular mechanics (MM) and molecular dynamic (MD) calculations,[40] **CTPC** showed a similar left-handed 3/2 helix. The enantiomers interacted with the carbamate groups through hydrogen bonds and dipole−dipole interactions.[41]

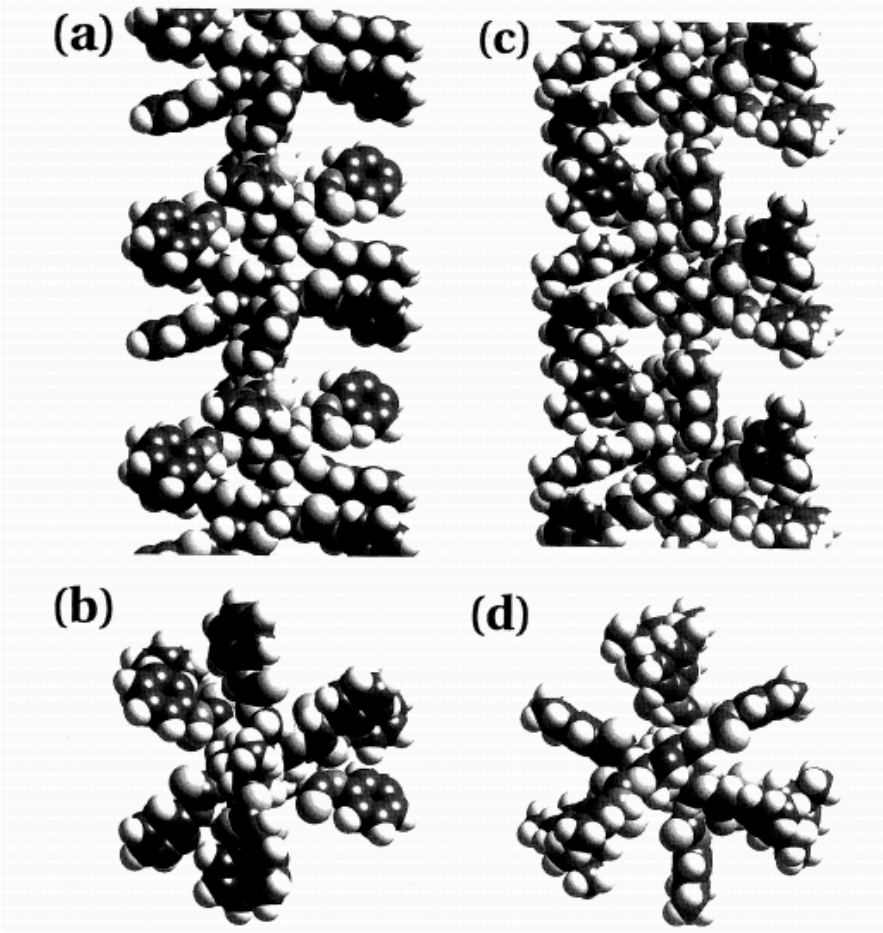


**Figure 1.8.** Optimized structures of (a) cellulose triphenylcarbamate and 3,5-dimethylphenylcarbamate from cellulose (b) perpendicular to (bottom) and along (top) the helix axis. (Reproduced with permission from Yamamoto, C.; Yashima, E.; Okamoto, Y. Computational Studies on Chiral Discrimination Mechanism of Phenylcarbamate Derivatives of Cellulose. *Bull. Chem. Soc. Jpn.* **1999**, *72*, 1815−1825. Copyright 1999 The Chemical Society of Japan Chemical Society.)

### 1.4 Molecular Twist in Polyfluorene

Polyfluorene is a typical π-conjugated polymer material and is used in light-emitting diodes (LED) and plastic solar cells.[42] It has been studied due to its large PL quantum efficiency and excellent chemical and thermal stability.[43] It is worth noting that fluorene is a typical CD-silent material with dynamic helicity.[44] The CD signals of fluorene may be canceled due to their axial switching between *P*- and *M*-conformations via free rotation. However, chirality changes due to external reactions are possible.

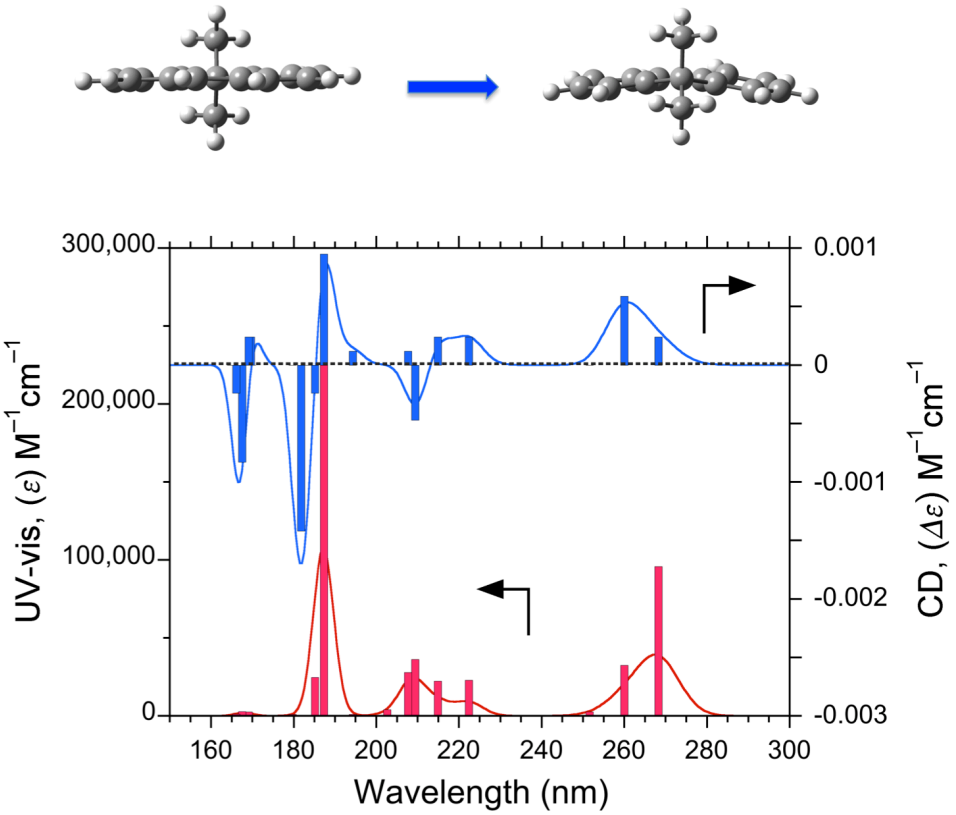


**Figure 1.9.** Simulated CD/UV-vis spectra and conformation change of 9,9-dimethylfluorene with a full width at half maximum of 0.1 eV.

Because the twist of the molecular backbone is central to understanding the optical activity, we employed a conformation simulation of 9,9-dimethylfluorene as a monomer model using Gaussian 09 software with TD-DFT calculations at the B3LYP/6-31G(d) level. When the fluorene molecules on the aromatic rings are not planar, it is possible to produce a chiral structure, although the CD sign is very weak (Figure 1.9).

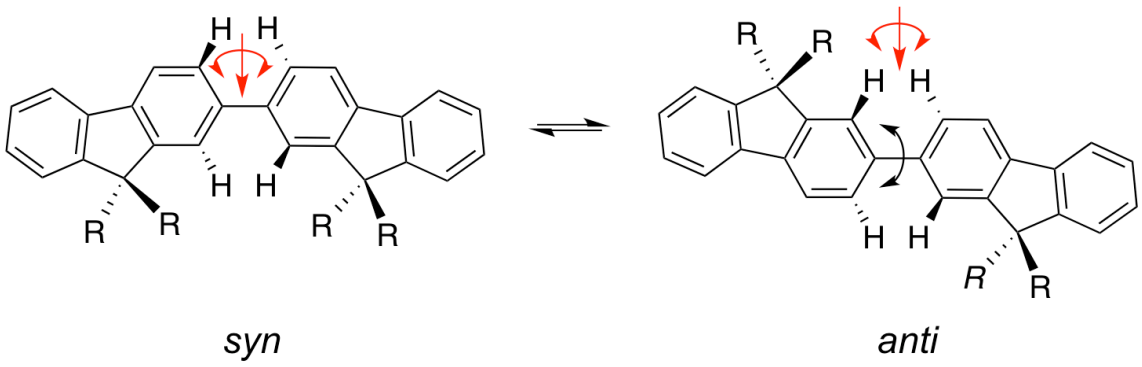


**Figure 1.10.** Dihedral angle changes between neighbor units in a fluorene dimer.

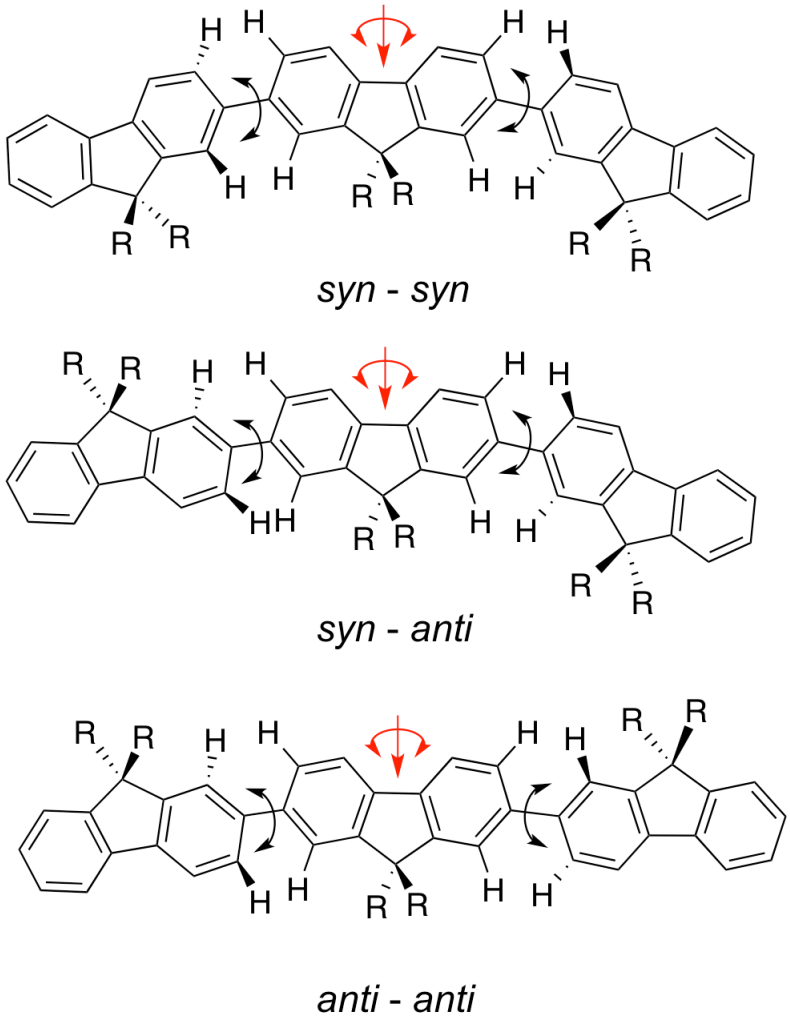


**Figure 1.11.** Dihedral angle changes between neighbor units in a fluorene trimer.

For fluorene dimers, we found a twist between neighbor units for the interactions of the CH groups. In addition, the dihedral angle only changed from *syn* to *anti* (Figure 1.10). This structure will show the same chiral direction.[45]

However, for trimers and more identical precursors in oligomers and polymers, dihedral angle changes have several styles with two kinds of direction selections (Figure 1.11): *syn* (left/right)-*syn* (left/right) style, *syn* (left/right)-*anti* (left/right) style, and *anti* (left/right)-*anti* (left/right) style. We considered the stability and optical activity differences in the fluorene oligomers and polymers depending on the dihedral angles of the main chain.

## 1.5 Purpose of This Research

The main purpose of this work is to establish and elucidate the chirality transfer between cellulose derivatives and fluorene derivatives in the film state. To achieve this objective, the author demonstrates two kinds of chirality transfer and inversion systems: (i) main chain helicity and/or D-glucose chirality of **CTA**/cellulose acetate butyrate (**CABu)** and (ii) helicity swapping induced by **CTPC** with solvent-induced on-off switching hydrogen bonds of carbamoyl groups.

In Chapter 3, the chirality transfer from **CTA** and **CABu** to 9,9-di-*n*-alkylfluorene oligomers and polymers is discussed. **CTA** and **CABu**, the common framework of $\beta(1\rightarrow4)$ linked D-glucose residues, are known to prefer right- and left-handed helicity, respectively. Actually, the preferential helicity toward the opposite screw sense, regardless of the common D-framework, allows the 9,9-dialkylfluorene derivatives to reveal circularly polarized luminescence (CPL) and circular dichroism (CD) signals with opposite signs.

In Chapter 4, a helix inversion of poly(9,9-di-*n*-hexylfluorene) (**PF6**) (and its fluorene oligomers) endowed with main chain helicity and/or D-glucose local chirality of **CTPC** will be discussed. This effect was proven by the CD and CPL spectra of PF6 embedded in the hybridized film. Although **CTPC** adopted left-hand helical conformations in the solid state, the helix preference of **PF6** was tailored by the choice of THF and $CH_2Cl_2$.

Lastly, Chapter 5 discusses the mechanisms of chirality transfer in the two systems. The intermolecular interactions between cellulose derivatives and fluorenes and the intramolecular structure change were investigated. Additionally, we employed a new structural calculation of two dihedral angles to discuss the optical activity of fluorene.

## 1.6 References


(1) Ribó, J. M.; Crusats, J.; Sagués, F.; Claret, J.; Rubires, R. *Science* **2001**, *292*, 2063−2066.

(2) de Greef, T. F. A.; Meijer, E. W. *Nature* **2008**, *453*, 171−173.

(3) Zou, G.; Jiang, H.; Kohn, H.; Manaka, T.; Iwamoto, M. *Chem. Commun.* **2009**, *37*, 5627−5629.

(4) Finn, M. G. *Chirality* **2002**, *14*, 534–540.

(5) Riehl, J. P.; Richardson, F. S. *Chem. Rev.,* **1986***, 86,* 1-16.

(6) Oda, M.; Nothofer, H. G.; Lieser, G.; Scherf, U.; Meskers, S. C. J.; Neher, D. *Adv. Mater*. **2000**, *12*, 362−365.

(7) Watson, J. D.; Crick, F. H. C. *Nature* **1953**, *171*, 737−738.

(8) Pauling, L.; Corey, R. B.; Branson, H. R. *Proc. Natl. Acad. Sci. U. S. A*. **1951**, *37*, 205−211.

(9) He, Y.; Ye, T.; Su, M.; Zhang, C.; Ribbe, A. E.; Jiang, W.; Mao, C. *Nature* **2008**, *452*, 198-201.

(10) Tachibana, T.; Kambara, H. *J. Am. Chem. Soc.,* **1965**, *87*, 3015−3016.

(11) Green, M. M.; Andreola, C.; Muñoz, B.; Reidy, M. P.; Zero, K. *J. Am. Chem. Soc.* **1988**, *110*, 4063−4065.

(12) Yashima, E.; Ousaka, N.; Taura, D.; Shimomura, K.; Ikai, T.; Maeda, K. *Chem. Rev.* **2016**, *116*, 13752–13990.

(13) Okamoto, Y.; Suzuki, K.; Ohta, K.; Hatada, K.; Yuki, H. *J. Am. Chem. Soc.* **1979**, *101*, 4763−4765

(14) Corley, L. S.; Vogl, O. *Polym. Bull.* **1980**, *3*, 211−217.

(15) Ohtake, T.; Tanaka, H. *Polymer J.* **2015**, *48*, 25–37.

(16) Nakano, Y.; Ichiyanagi, F.; Naito, M., Yang, Y.; Fujiki, M. *Chem. Comm.*, **2012**, *48*, 6636−6638.

(17) Zhao, Y.; Rahim, N. A. A.; Xia, Y.; Fujiki, M.; Song, B.; Zhang, Z.; Zhu, X. *Macromolecules*, **2016**, *49*, 3214–3221.

(18) Cornelissen, J. J.; Rowan, A. E.; Nolte, R. J.; Sommerdijk, N. A. *Chem. Rev.*, **2001**, *101*, 4039−4070.

(19) Koe, J. R.; Fujiki, M.; Motonaga, M.; Nakashima, H. *Macromolecules*, 2001, 34, 1082−1089.

(20) Fujiki, M.; Donguri, Y.; Zhao, Y.; Nakao, A.; Suzuki, N.; Yoshida, K.; Zhang, W. *Polym. Chem.*, **2015**, *6*, 1627-1638.

(21) Chu, G.; Wang, X.; Chen, T.; Xu, W.; Wang, Y.; Song, H.; Xu, Y. *J. Mater. Chem. C*, **2015**, *3*, 3384-3390.

(22) Rahim, N. A. A.; Fujiki, M. *Polym. Chem.*, **2016**, *7*, 4618–4629.

(23) Gandini, A.; Lacerda, T. M.; Carvalho, A. J.; Trovatti, E. *Chem. Rev.* **2015**, *116*, 1637-1669.

(24) Heuer, A. H.; Fink, D. J.; Laraia, V. J.; Arias, J. L.; Calvert, P. D.; Kendall, K.; Messing, G. L.; Blackwell, J.; Rieke, P. C.; Thompson, D. H.; Wheeler, A. P.; Veis, A.; Caplan, A. I. *Science* **1992**, *255*,1098.

(25) Arias, J. L.; Fernández, M. S. *Chem. Rev.* **2008**, *108*, 4475-4482.

(26) Habibi, Y.; Lucia, L. A.; Rojas, O. J. *Chem. Rev.* **2010**, *110*, 3479-3500.

(27) Mäki-Arvela, P.; Salmi, T.; Holmbom, B.; Willför, S.; Murzin, D. Y. Chem. Rev. 111, 5638-5666.

(28) Eyley, S.; Thielemans, W. *Nanoscale* **2014**, *6*, 7764-7779.

(29) Nakagaito, A. N.; Yano, H. *Appl. Phys. A.* **2004**, *78*, 547-552.

(30) Barbey, R.; Lavanant, L.; Paripovic, D.; Schüwer, N.; Sugnaux, C.; Tugulu, S.; Klok, H. A. *Chem. Rev.* **2009**, *109*, 5437-5527.

(31) Sen, S.; Martin, J. D.; Argyropoulos, D. S. *ACS Sustainable Chem. Eng.* **2013**, *1*, 858-870.

(32) Pinkert, A.; Marsh, K. N.; Pang, S.; Staiger, M. P. *Chem. Rev.* **2009,** *109*, 6712-6728.

(33) Aoki, D.; Nishio, Y. *Cellulose* **2010**, *17*, 963-976.

(34) Soeta, H.; Fujisawa, S.; Saito, T.; Berglund, L.; Isogai, A. *ACS Appl. Mater. Interfaces*. **2015**, *7*, 11041–11046.

(35) Abd Manaf, M. E.; Tsuji, M.; Shiroyama, Y.; Yamaguchi, M. *Macromolecules* **2011**, *44*, 3942-3949.

(36) Okamoto, Y.; Kaida, Y. *J. Chromatogr. A* **1994**, *666*, 403–419.

(37) Shen, J.; Okamoto, Y. *Chem. Rev.* **2016**, *116*, 1094–1138.

(38) Okamoto, Y.; Kawashima, M.; Hatada, K. *J. Am. Chem. Soc.* **1984**, *106*, 5357−5359.

(39) Chankvetadze, B.; Yashima, E.; Okamoto, Y. *Chem. Lett.* **1993**, 617−620.

(40) Yamamoto, C.; Yashima, E.; Okamoto, Y. *Bull. Chem. Soc. Jpn.* **1999**, *72*, 1815−1825.

(41) Okamoto, Y.; Ohashi, T.; Kaida, Y.; Yashima, E. *Chirality* **1993**, *5*, 616−621.

(42) Coffey, D. C.; Ginger, D. S. *Nature Mater.* **2006**, *5*, 735-740.

(43) Pei, Q.; Yang, Y. *J. Am. Chem. Soc.* **1996**, *118*, 7416–7417.

(44) Wang, Y.; Sakamoto, T.; Nakano, T. *Chem. Commun.* **2012**, *48*, 1871-1873.

(45) Wang, L., Suzuki, N., Liu, J., Matsuda, T., Rahim, N. A. A., Zhang, W., Fujiki, M.; Zhang, Z.; Zhang, N.; Zhu, X. *Polym. Chem.* **2014**, *5*, 5920-5927.

## Chapter 2. Experimental Details and Materials Used in this Thesis

### 2.1 Cellulose Triacetate (CTA), Cellulose Acetate Butyrate (CABu), and Cellulose Triphenyl Carbamate (CTPC)

For the helical structures of the cellulose derivatives, we chose three kinds of cellulose derivatives as chirality providers: cellulose triacetate (**CTA**) (Wako Pure Chemicals, Osaka, Japan, the first grade, $M_w$ = 60 000), cellulose acetate butyrate (**CABu**) (Sigma-Aldrich, St. Louis, MO, US, $M_w$ = 65 000) and cellulose triphenyl carbamate (**CTPC**) (Scheme 2.1).

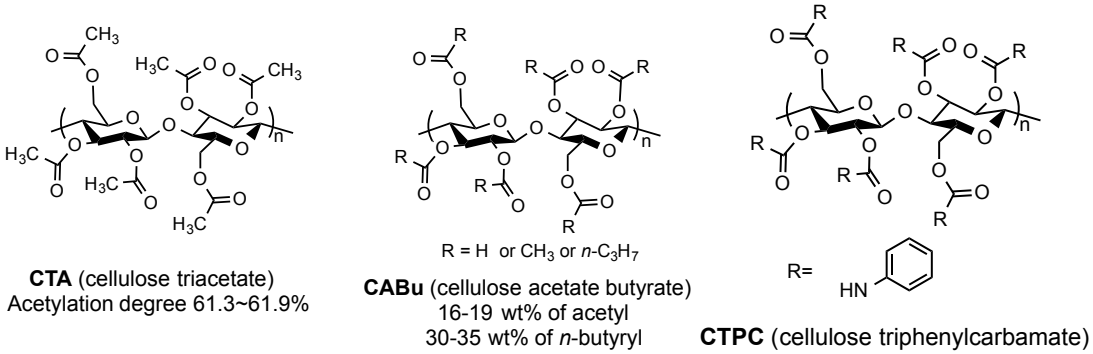


**Scheme 2.1.** Chemical structures of cellulose triacetate (**CTA**), cellulose acetate butyrate (**CABu**), and cellulose triphenyl carbamate (**CTPC**).

The synthesis process of **CTPC** is shown in Scheme 2.2.[1] Microcrystalline cellulose (1 g) (Sigma-Aldrich, St. Louis, MO, US) was vacuum dried at 60°C for 12 h, 50 mL of pyridine (Dehydrated, Wako Pure Chemicals, Osaka, Japan) was added, and the mixture was heated under reflux for 12 h. After the addition of 8 mL of phenyl isocyanate (Sigma-Aldrich, St. Louis, MO, US), refluxing was continued for 48 h, and then the mixture was allowed to cool. The cellulose derivative was precipitated with 400 mL of anhydrous methanol and allowed to stand. After filtering and washing with methanol several times, the product was vacuum dried at 60°C for 12 h, and 2.95 g of

**CTPC** was obtained (95% yield). The purity was characterized with elemental analysis and $^{1}$H-NMR spectra.[2,3]

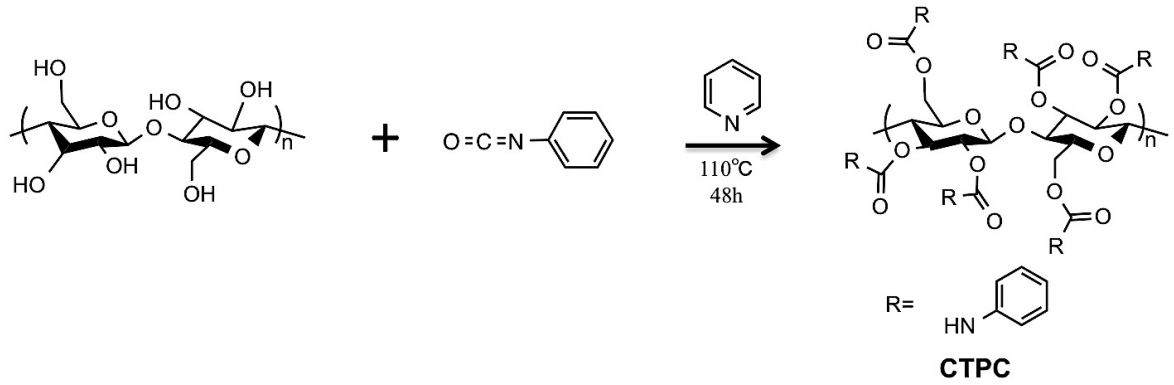


**Scheme 2.2.** Synthesis process for cellulose triphenyl carbamate (**CTPC**).

## 2.2 9,9-Dialkylfluorene (FL) Oligomers and Polymers

A series of fluorene derivatives were prepared (Scheme 2.3). 9,9-Dimethylfluorene (**F1**) (TCI, Tokyo, Japan) and 9,9-di-n-propylfluorene dimer (**F2**) (Excition Inc. US) were used without further purification. 9,9-Di-n-hexylfluorene trimer (**F3**), 9,9-di-n-hexylfluorene pentamer (**F5**), and 9,9-di-n-hexylfluorene heptamer (**F7**) were purchased from American Dye Source Inc. Poly(9,9-di-*n*-hexylfluorene) (**PF6**) (Sigma-Aldrich, $M_w$ = 69 400 ($DP_w$ = 208), $M_n$ = 15 700 ($DP_n$ = 47)) and poly(9,9-di-*n*-octylfluorene) (**PF8**) (Sigma-Aldrich, $M_w$ = 141 120 ($DP_w$ = 362) and $M_n$ = 78 400 ($DP_n$ = 201))[4] were used without further purification.

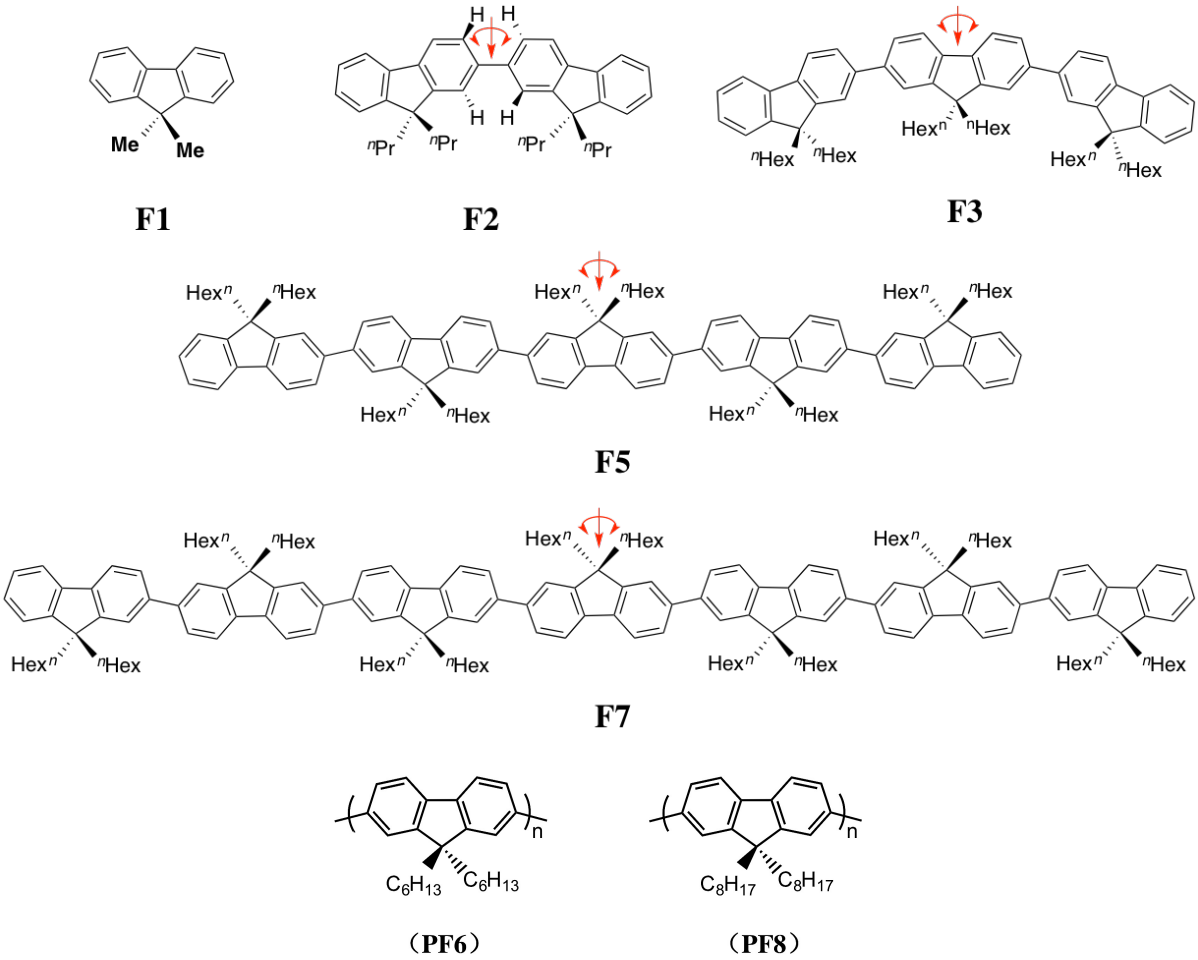


**Scheme 2.3.** Chemical structures of the fluorene derivatives in this work.

### 2.3 Hybrid Films of Soluble Celluloses with Dialkylfluorene Derivatives

We made **CTA/CABu** hybrid films for different mechanisms of chirality transfer. First, 10 mg of fluorene derivatives and 10 mg of cellulose derivatives (**CTA** or **CABu**) were dissolved in 1.0 mL of $CHCl_3$ independently at 50°C for 5 h, and the samples were left for 6 h at room temperature. After these mixtures were completely dissolved, the two solutions were mixed at room temperature to obtain the desired fractions of the fluorene/**CTA** (1/100 by w/v) and fluorene/**CABu** (1/100 by w/v); the mixed solutions were kept in glass vials in the dark. The hybridized films were deposited onto polished circular quartz plates (25 mm in diameter and 1 mm thick) by spin coating using a 1HD7 spin coater (MIKASA, Japan). To reduce the formation of defects and voids, 40 μL of the solution was placed on the center of the plate and spun under 2 000 rpm for 1 min.

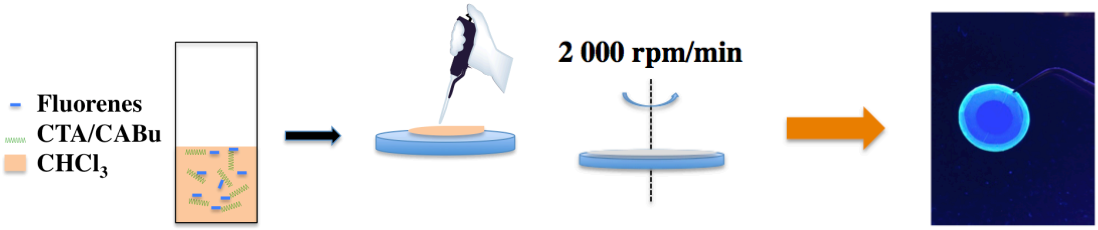


**Figure 2.1.** The production process of the **CTA/CABu** hybrid film.

**CTPC** hybrid films were formed using a similar method. We made the **CTPC** hybrid film after dissolved in THF and $CH_2Cl_2$ to achieve different mechanisms of chirality transfer. First, 10 mg of fluorene derivatives and 10 mg of **CTPC** were dissolved in 1.0 mL of $CH_2Cl_2$ and 1.0 mL of THF independently at 50°C for 5 h, and the samples were left for 6 h at room temperature. After these mixtures were completely dissolved, the two solutions were mixed at room temperature to obtain the desired fractions the fluorene/**CTPC** (1/1 by v/v) in THF and fluorene/**CTPC** (1/1 by v/v) in $CH_2Cl_2$; the

mixed solutions were kept in glass vials in the dark. The hybridized films were deposited onto polished circular quartz plates (25 mm in diameter and 1 mm thick) by spin coating using a 1HD7 spin coater (MIKASA, Japan). To reduce the formation of defects and voids, 40 μL of the solution was placed on the center of the plate and spun at 2 000 rpm for 1 min. Double-sided coatings were used in this research to remove false signals.

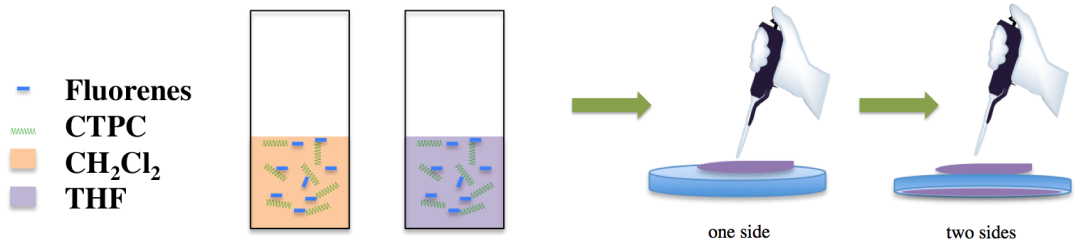


**Figure 2.2.** The production process of the **CTPC** hybrid films.

## 2.4 Characterization

### 2.4.1 Circular Dichroism (CD), UV-visible, Circularly Polarized Luminescence (CPL), and Photoluminescence (PL) Spectra

Film samples were placed on cylindrical quartz plates in a sample housing at room temperature. UV-vis absorption and CD spectra were recorded using a JASCO (Tokyo, Japan) J-820 spectropolarimeter at room temperature. The experimental parameters were simultaneously obtained with a bandwidth of 2.0 nm, a scanning rate of 100 nm $min^{-1}$, and a sampling point of 1.0 nm. CPL and PL spectra were recorded at room temperature on a JASCO CPL-200 spectrofluoropolarimeter with bandwidths of 10 nm for excitation and emission, a scanning rate of 100 nm $min^{-1}$, and sampling data points of 0.5 nm. The absolute CPL amplitude was calibrated with fresh D-/L-camphor solutions at bandwidths of 3000 *m*m for excitation and emission.

### 2.4.2 One-Dimensional (1D) and Two-Dimensional (2D) Fourier Transform (FT) Nuclear Magnetic Resonance (NMR) Spectra

The hybridized polymers were characterized with cross-polarization magic angle spinning (CP/MAS) $^{13}$C-NMR and heteronuclear correlation (HETCOR) $^{1}$H-$^{13}$C-NMR spectra in the solid state at room temperature with a 400 MHz JEOL (Akishima-Tokyo, Japan) ECX-400P FT-NMR spectrometer. The film samples were pulverized into powders by immersion in liquid nitrogen, enabling CP/MAS solid-state 1D $^{13}$C-NMR and 2D HETCOR $^{1}$H-/$^{13}$C-NMR measurements.

### 2.4.3 FT-Infrared (FTIR) Spectra

IR spectra were recorded on a $CaF_2$ plate using a Horiba FT-730 infrared spectrometer (Horiba, Ltd., Kyoto, Japan) over a wavenumber range between 900 and 4000 $cm^{-1}$ with a resolution of 2 $cm^{-1}$ and a scanning speed of 5 mm/s for 128 scans.

2.4.4 Wide-Angle X-ray Diffraction (WAXD)

Wide-angle X-ray diffraction (WAXD) data were collected using a Rigaku RINT-TTR III/NM instrument (Akishima-Tokyo, Japan) with an X-ray wavelength of 1.5418 Å, Cu$K_\alpha$ radiation with a Ni filter, an interval scan of $2\theta = 0.05°$ and a scanning speed of 2 deg $min^{-1}$. The instrument was operated at 40 kV and 25 mA. Specimens on a Si-crystal substrate were prepared by casting in chloroform solutions.

2.4.5 Computational Modeling and Calculations

All of the model structures were simulated in this work, which permitted us to explore all possible intermolecular interactions between the fluorenes and cellulose derivatives by MD using a Forcite module with a universal force field (UFF) in Materials Studio, ver.7 (Accelrys, now, BIOVIA, San Diego, CA, US) and a DFT calculation with the B3LYP and 6-31G(d) basis set in the Gaussian 09 package (Gaussian Inc., Wallingford, CT, US). [5] Twenty transition states (singlets) for the **fluorene trimer** were obtained with the TD-DFT method with the B3LYP and 6-31G(d) basis set.[6]

2.4.6 Differential Scanning Calorimetry (DSC)

Differential scanning calorimetry (DSC) data were collected using an HITACHI DSC6200 (Hitachi High-Tech Science Corporation, Japan) on an Al container with a scanning speed of 10°C/min from 0°C to 180°C.

## 2.5 References


(2) Okamoto, Y.; Aburatani, R.; Kaida, Y.; Hatada, K. *Chem. Lett.*, **1988**, *209*, 1125–1128.

(3) Yamamoto, C.; Yashima, E.; Okamoto, Y. *J. Am. Chem. Soc.*, **2002**, *124*, 12583–12589.

(4) Fulmer, G. R.; Miller, A. J.; Sherden, N. H.; Gottlieb, H. E.; Nudelman, A.; Stoltz, B. M.; Goldberg, K. I. *Organometallics*, **2010**, *29*, 2176–2179.

(5) Rahim, N. A. A.; Fujiki, M. *Polym. Chem.* **2016**, *7*, 4618–4629.

(6) Frisch, M. J.; Trucks, G. W.; Schlegel, H. B.; Scuseria, G. E.; Robb, M. A.; Cheeseman, J. R.; Scalmani, G.; Barone, V.; Mennucci, B.; Petersson, G. A.; Nakatsuji, H.; Caricato, M.; Li, X.; Hratchian, H. P.; Izmaylov, A. F.; Bloino, J.; Zheng, G. J.; Sonnenberg, J. L.; Hada, M.; Ehara, M.; Toyota, K.; Fukuda, R.; Hasegawa, J.; Ishida, M.; Nakajima, T.; Honda, Y.; Kitao, O.; Nakai, H.; Vreven, T.; Montgomery, Jr., J. A.; Peralta, J. E.; Ogliaro, F.; Bearpark, M.; Heyd, J. J.; Brothers, E.; Kudin, K. N.; Staroverov, V. N.; Keith, T.; Kobayashi, R.; Normand, J.; Raghavachari, K.; Rendell, A.; Burant, J. C.; Iyengar, S. S.; Tomasi, J.; Cossi, M.; Rega, N.; Millam, J. M.; Klene, M.; Knox, J. E.; Cross, J. B.; Bakken, V.; Adamo, C.; Jaramillo, J.; Gomperts, R.; Stratmann, R. E.; Yazyev, O.; Austin, A. J.; Cammi, R.; Pomelli, C.; Ochterski, J. W.; Martin, R. L.; Morokuma, K.; Zakrzewski, V. G.; Voth, G. A.; Salvador, P.; Dannenberg, J. J.; Dapprich, S.; Daniels, A. D.; Farkas, O.; Foresman, J. B.; Ortiz, J. V.; Cioslowski, J.; Fox, D. J. GAUSSAIAN09 (Rev.D.01), Gaussian, Inc., Wallingford CT, 2013.

(7) Suzuki, N.; Fujiki, M.; Kimpinde-Kalunga, R. K.; Koe, J. R. *J. Am. Chem. Soc.* **2013**, *135*, 13073–13079.

## Chapter 3. Chirality Transfer Experiments from Cellulose Alkyl Esters

### 3.1 CD Inversion Capability of CTA and CABu

We demonstrate a versatile approach capable of obtaining chiroptically elaborate films, including a series of CD-active/CPL-active fluorene oligomers and polymers induced by the point chirality and/or helicity of **CTA** and **CABu** as host chiral polymers, even if the CD-silent/CPL-silent polymers in dilute solutions were employed. Although **CTA** and **CABu** are commonly composed of D-glucose subunits with β-linkages,[1,2] **CTA** and **CABu** are known to prefer right- and left-helix directions, respectively (**Figure 3.1**).[3]

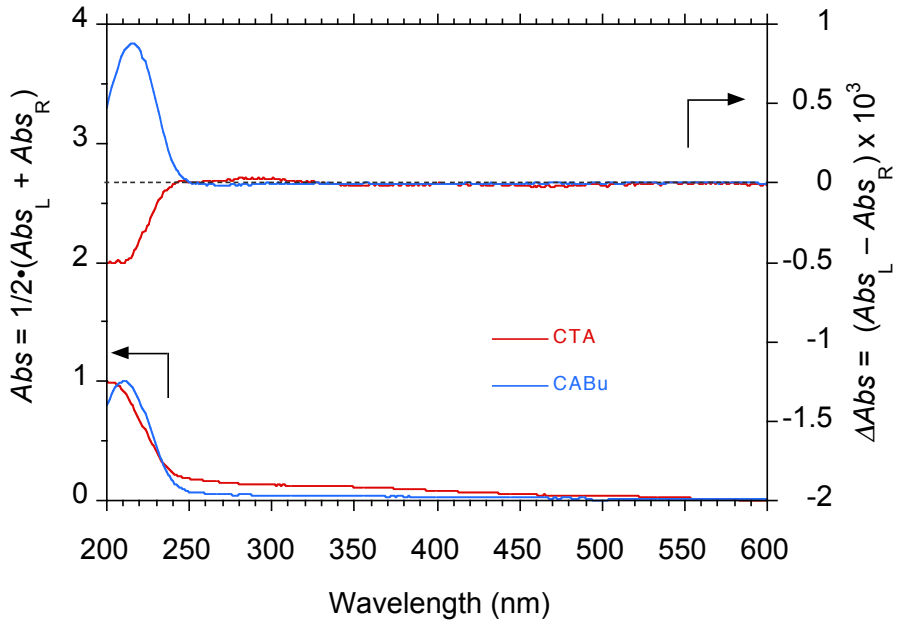


**Figure 3.1.** Normalized CD/UV-vis spectra of the **CTA**/**CABu** thin films.

**CTA** and **CABu** provided a range of different helical chirality transfer geometries and environments, affording a study their mechanisms. We hypothesized that **CTA** and **CABu** could provide various helicity and point-chirality transfer capabilities.

### 3.2 From CTA to FL Oligomers and Polymers

The UV-vis and CD spectra at the $S_0 \rightarrow S_1$ transition of the fluorene derivatives in **CTA** are shown in Figure 3.2. The CD spectra in the other **CTA** films hybridized with fluorenes revealed similar tendencies associated with the same chiroptical (+) and (–) signs at the first and second Cotton bands, respectively.[4]

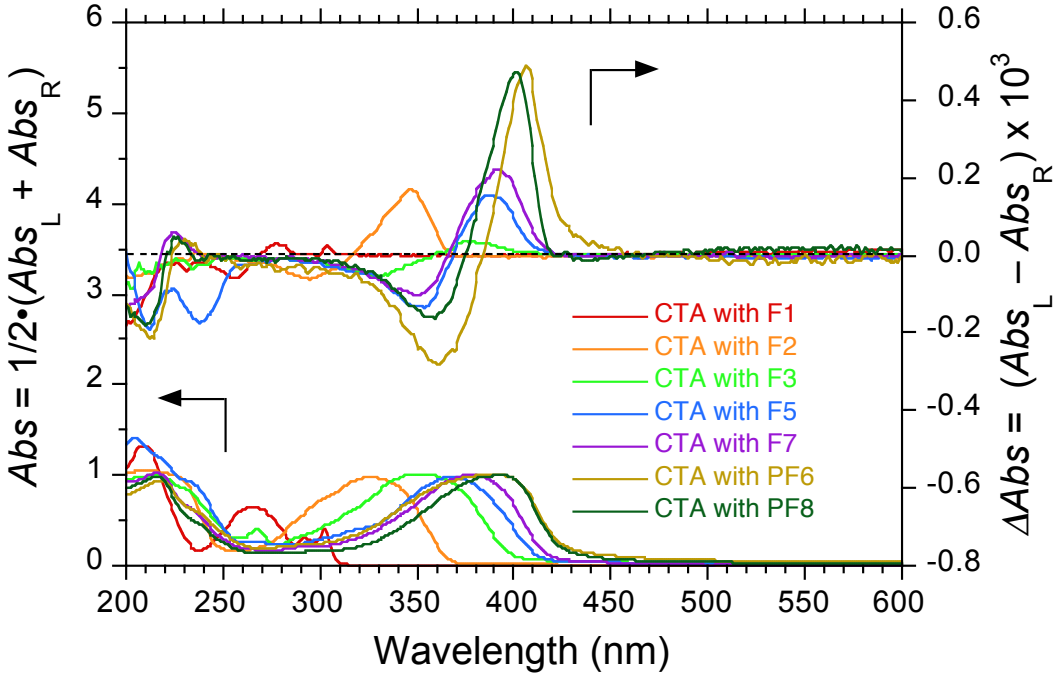


**Figure 3.2.** Normalized CD/UV-vis spectra of the **CTA** thin films including fluorenes at 293 K on a quartz substrate.

In the **CTA-F1** film, a weak CD signal had a (+) sign at the first Cotton band ($g_{CD}$ = +0.08 $\times 10^{-3}$ at 304 nm). In the **CTA-F2** film, a bisignate CD signal had a (+) sign at the first Cotton band ($g_{CD}$ = +0.24 $\times 10^{-3}$ at 345 nm), (–) sign at the second Cotton band ($g_{CD}$ = -0.06 $\times 10^{-3}$ at 295 nm), and was zero at 317 nm. In the **CTA-F3/F5/F7** film, a bisignate weak CD signal had a (+) sign at the first Cotton band ($g_{CD}$ = +0.04 $\times 10^{-3}$ at 375 nm for **F3**, $g_{CD}$ = +0.21 $\times 10^{-3}$ at 385 nm for **F5,** and $g_{CD}$ = +0.25 $\times 10^{-3}$ at 390 nm for **F7**) and a (–) sign at the second Cotton band ($g_{CD}$ = -0.08 $\times 10^{-3}$ at 330 nm for **F3**, $g_{CD}$ =

-0.14 $\times 10^{-3}$ at 350 nm for **F5**, and $g_{CD}$ = -0.16 $\times 10^{-3}$ at 360 nm for **F7**) associated with a zero-cross-point at 360 nm/365 nm/368 nm. In the **CTA-PF8** film, a bisignate CD signal had a (+) sign at the first Cotton band ($g_{CD}$ = +0.54 $\times 10^{-3}$ at 400 nm), (–) sign at the second Cotton band ($g_{CD}$ = -0.18 $\times 10^{-3}$ at 358 nm), and a zero point at 375 nm. Among these fluorene oligomers and polymers, **PF6** afforded the largest $g_{CD}$ value at the first and second Cotton bands, reaching $g_{CD}$ = +0.59 $\times 10^{-3}$ at 407 nm and $g_{CD}$ = –0.36 $\times 10^{-3}$ at 361 nm.

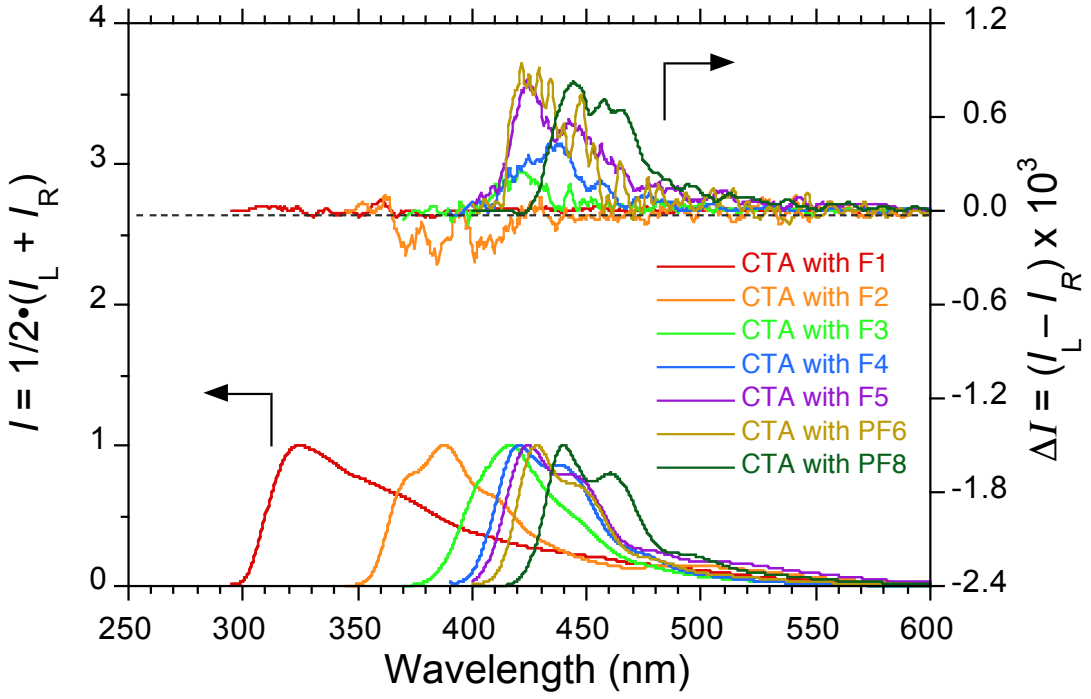


**Figure 3.3.** Normalized CPL/PL spectra of the **CTA** thin films including fluorenes at 293 K on a quartz substrate.

Next, the representative CPL and PL spectra of the fluorenes in **CTA** are depicted in Figure 3.3. The sign and $g_{CPL}$ magnitude of the CPL signals reflected the lowest photoexcited chirality. The luminescence dissymmetry factors ($g_{CPL}$) were -0.40 $\times$ $10^{-3}$ (at 380 nm) for **F2**, 0.28$\times$ $10^{-3}$ (at 415 nm) for **F3**, 0.51$\times$ $10^{-3}$ (at 435 nm) for **F5**, 0.79$\times$

$10^{-3}$ (at 425 nm) for **F7**, 0.89× $10^{-3}$ (at 425 nm) for **PF6** and 0.9 × $10^{-3}$ (at 423 nm) for **PF8**. All fluorene derivatives adopted a certain chiral twisted conformation with a preferred helicity in the photoexcited state. Emerging CPL characteristic arose from the bisignate CD amplitudes led by the twisted fluorene rings in the ground state when a helical creation immobilized by the **CTA** matrix in the ground state was maintained, even in the photoexcited state.

The induced CD/CPL signals from the fluorene derivatives showed an efficient induction of **CTA** chirality and/or its main chain helicity was possible for a series of achiral (CD/CPL-silent) fluorene derivatives via the intermolecular interactions.

### 3.3 From CABu to FL Oligomers and Polymers

For comparison, we also show the UV-vis and CD spectra at the $S_0 \rightarrow S_1$ transition of the fluorene derivatives in **CABu** (Figure 3.3). Similarly, the *right*-handed helicity[2,3] and/or pointed chirality of the **CABu** was efficiently transferred to the fluorene oligomers and polymers. The bisignate CD profiles associated with the (+) and (–) signs at the first and second Cotton bands of the oligomers in **CABu** were almost similar to those in **CTA** films, except **F1**, **PF6**, and **PF8.**

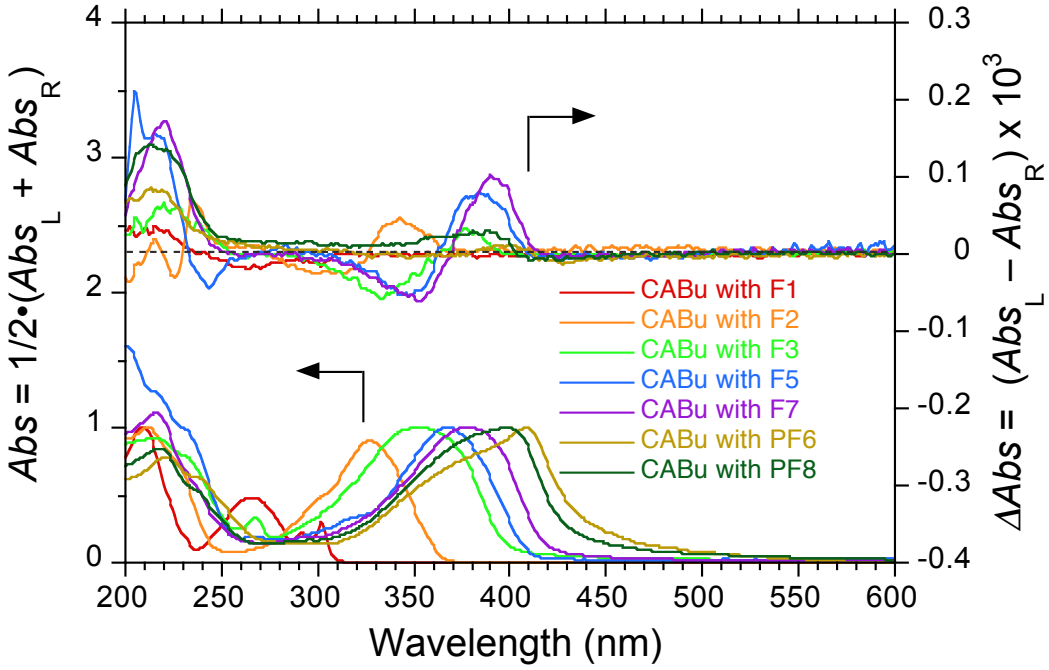


**Figure 3.4.** Normalized CD/UV-vis spectra of the **CABu** thin films including fluorenes at 293 K on a quartz substrate.

In the **CABu-F1** film, the weak CD signal had a (-) sign at the first Cotton band ($g_{CD}$ = -0.04 $\times 10^{-3}$ at 304 nm). In the **CABu-F2** film, a bisignate CD signal had a (+) sign at the first Cotton band ($g_{CD}$ = +0.07 $\times 10^{-3}$ at 345 nm), (–) sign at the second Cotton band ($g_{CD}$ = -0.05 $\times 10^{-3}$ at 309 nm), and a zero point at 327 nm. In the **CABu-F3** (**F5**/**F7**) film, the $g_{CD}$ value at the first and second Cotton bands were $g_{CD}$ = +0.04 $\times 10^{-3}$ at 378 nm ($g_{CD}$ =

+0.07 $\times 10^{-3}$ at 383 nm for **F5**, $g_{CD}$ = +0.11 $\times 10^{-3}$ at 390 nm for **F7**) and $g_{CD}$ = -0.08$\times 10^{-3}$ at 333 nm ($g_{CD}$ = -0.05 $\times 10^{-3}$ at 347 nm for **F5**, $g_{CD}$ = -0.06 $\times 10^{-3}$ at 353 nm for **F7**). In contrast, the first Cotton band had a (-) signs ($g_{CD}$ = -0.03 $\times 10^{-3}$ at 420 nm and $g_{CD}$ = -0.03 $\times 10^{-3}$ at 412 nm), and the second Cotton band had a (+) sign ($g_{CD}$ = +0.01 $\times 10^{-3}$ at 400 nm and $g_{CD}$ = +0.03 $\times 10^{-3}$ at 390 nm) for **PF6** and **PF8.** The **PF6** and **PF8** exhibited opposite bisignate CD profiles with (–) and (+) signs at the first and second Cotton bands, respectively. Nevertheless, shorter fluorene oligomers, including **F2, F3**, **F5**, and **F7**, exhibited the same (+) and (–) signs for the first and second Cotton bands, respectively, disregarding the **CTA** and **CABu** that preferred the opposite helix sense.

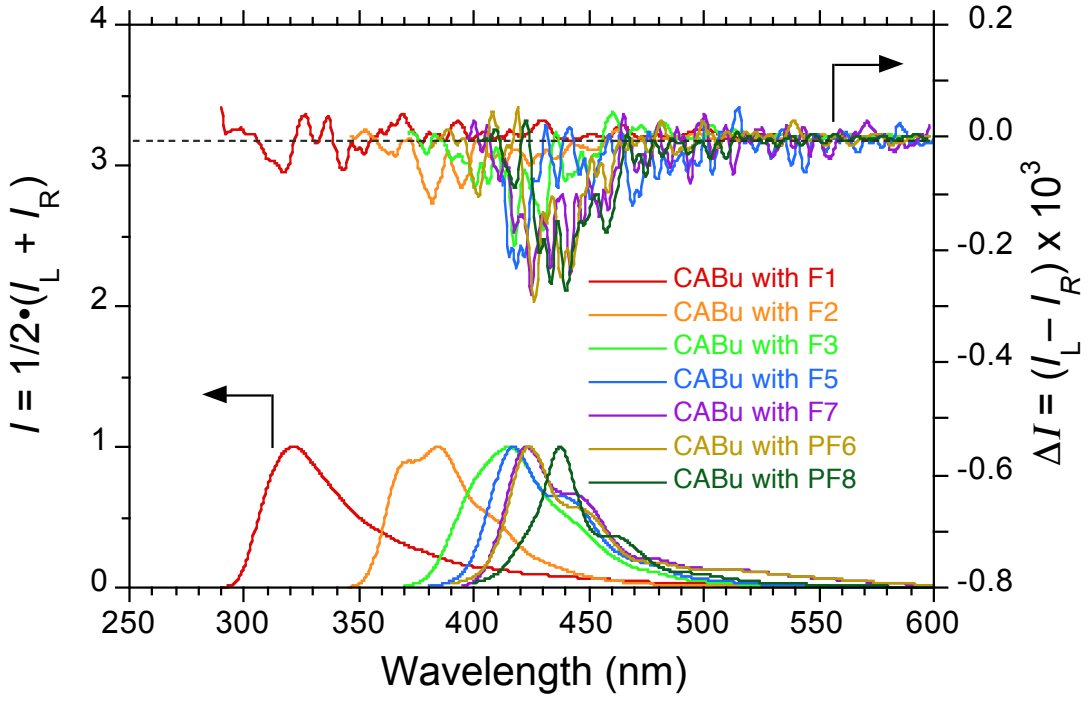


**Figure 3.5.** Normalized CPL/PL spectra of the **CABu** thin films including fluorenes at 293 K on a quartz substrate.

The representative CPL and PL spectra of the fluorenes are depicted in Figure 3.5. Similarly, all fluorene derivatives adopted a twisted conformation with a preferred

helicity in the photoexcited state. The $g_{CPL}$ values were -0.14 $\times 10^{-3}$ at 381 nm for **F2**, -0.15 $\times 10^{-3}$ at 381 nm for **F3**, -0.25 $\times 10^{-3}$ at 418 nm for **F5**, -0.24 $\times 10^{-3}$ at 425 nm for **F7**, -0.24 $\times 10^{-3}$ at 425 nm for **PF6**, and -0.23 $\times 10^{-3}$ at 430 nm for **PF8**. Noticeably, the CPL sign in the photoexcited state was opposite of the CD sign at the first Cotton CD band in the ground state for **F2**, **F3**, **F5** and **F7**. This anomaly in **CABu** may have originated from a conflict between the main chain helicity and D-glucose chirality, which oppositely induced helicity to the fluorene rings, depending on the fluorene ring numbers. The helix and/or chirality inducing capabilities of **CABu** were rather weak when compared to those of **CTA**.

### 3.4 Chirality Transfer Capability as a Function of FL Repeating Unit

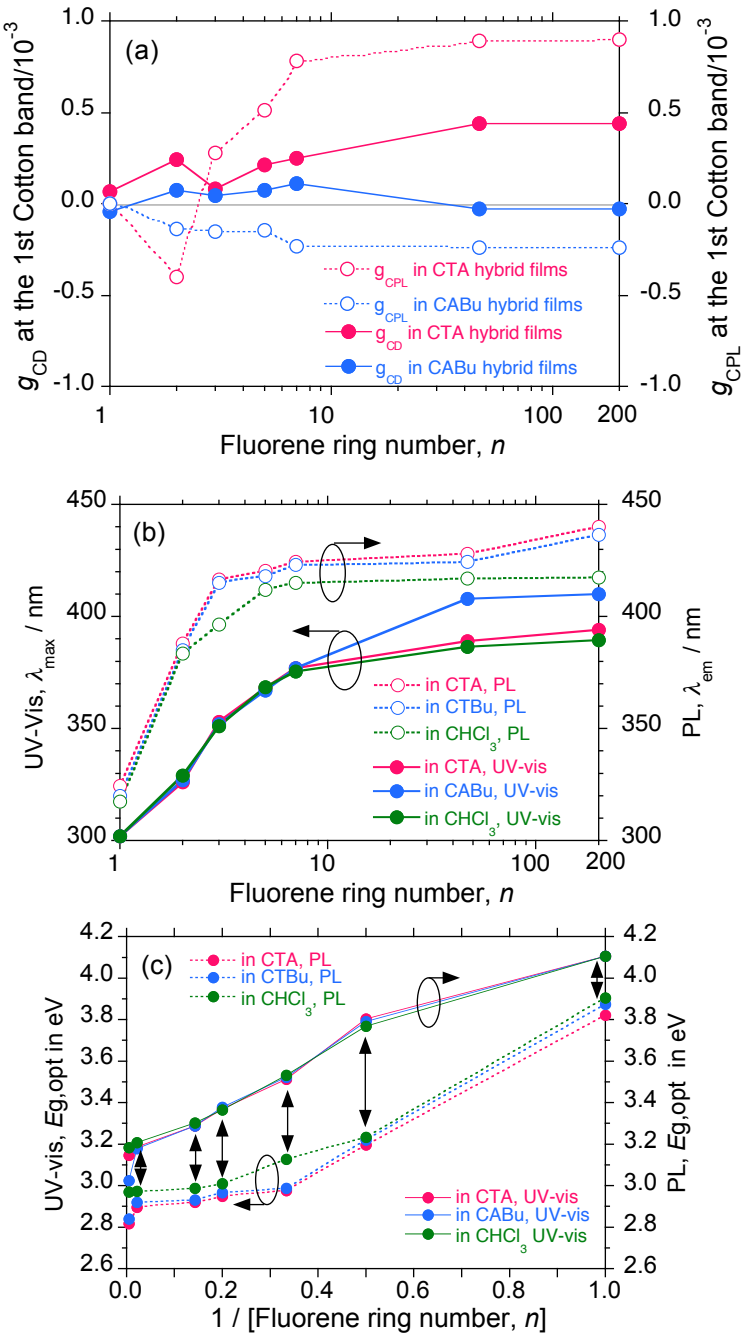


**Figure 3.6** (a) The $g_{CD}$ and $g_{CPL}$ values at the first Cotton band of the CD and CPL spectra as a function of the fluorene ring number ($n$) in the **CTA** and **CABu** films. (b)The $\lambda_{max}$ ($S_0 \rightarrow S_1$ transition) and $\lambda_{em}$ values ($S_1 \rightarrow S_0$ transition) in the **CTA**, **CABu,** and chloroform solution as functions of the fluorene ring number. (c) The optical bandgap, Eg, opt, obtained from the $\lambda_{max}$ and $\lambda_{em}$ values for the **CTA**, **CABu**, and chloroform solution as a function of the reciprocal fluorene ring number. The arrows indicate Stokes' shifts.

Moreover, the $|g_{CPL}|$ and $|g_{CD}|$ values in **CTA** and **CABu** tended to be nonlinearly enhanced when the fluorene repeating units increased and approached constant values (Figure 3.6a). This indicates that the helicity and/or chirality inducing capabilities are enhanced with fluorene repeating units due to intermolecular non-covalent helix/chiral interactions with **CTA** and **CABu**. Based on the CD spectral signs induced by **CTA** and **CABu**, we assumed that five chiral centers of the D-glucose repeating units were deterministic factors of the twist sense in shorter fluorene oligomers with $n$ = 3, 5, and 7 at the ground states, while a preference for the helix sense in longer D-glucose structures was more crucial for longer polyfluorenes ($n$ > 47) than the chiral centers. Conversely, the opposite helicity between **CTA** and **CABu** induced the opposite CPL sign to the fluorene oligomers but the same CPL sign to **PF6** and **PF8**.

When the $\pi$-electron in the $\pi$-conjugated molecular wires was delocalized, the $S_0 \rightarrow S_1$ transition energy was lowered. The degree of twisting in a one-dimensional semiconductor should be responsible for the charge carrier mobility within lower optical bandgap (*Eg, opt*) polymers, as proven by the redshift of PL and UV-vis bands.[5] The *Eg, opt* values obtained with $\lambda_{max}$ and $\lambda_{em}$ values in the series of the dialkylfluorene oligomers and polymers in the **CTA** and **CABu** films and in chloroform were approximately linearly lowered as a function of the reciprocal fluorene ring number ($n^{-1}$), except for monomers with $n^{-1}$ = 1.0 (Figure 3.6c, filled circles). Moreover, Stokes's shift between the *Eg, opt* from $\lambda_{max}$ and *Eg, opt* from $\lambda_{em}$ values tended to be small when the repeating number of fluorene rings increased. This indicates that very minimal reorganization of the fluorene main chains in the photoexcited and ground states occurred when the number of fluorene rings increased.[6]

The *Eg, opt* values from the $\lambda_{em}$ values of **PF6** and **PF8** in the **CTA** and **CABu** films

considerably redshifted by ≈ 0.16 eV (≈ 1300 $cm^{-1}$), compared to those in the chloroform (Figure 3.6c), indicating the great suppression of the twisted distortion of the fluorene rings in these films in the photoexcited states. Although the planarization of fluorene rings in the photoexcited states causes redshifts, the existence of inherent C-H/H-C repulsions between the rings should prevent planarization in the photoexcited and ground states.[7]

### 3.5 Photoinduced racemization Capability as a Function of FL Repeating Unit

To determine whether the helical fluorenes induced by **CTA** in the photoexcited and the ground states existed stably, photoexcitation-induced racemization experiments of the CPL-active fluorene derivatives in the **CTA** film (0.2 $cm^2$ in area) under aerobic conditions were conducted by continuously irradiating an unpolarized UV-light source at 320 nm for **F2**, 350 nm for **F3**, 360 nm for **F7**, and 370 nm for **PF6** and **PF8**. A Xe-Hg arc lamp CPL-200 spectrometer was used as the UV-light source.

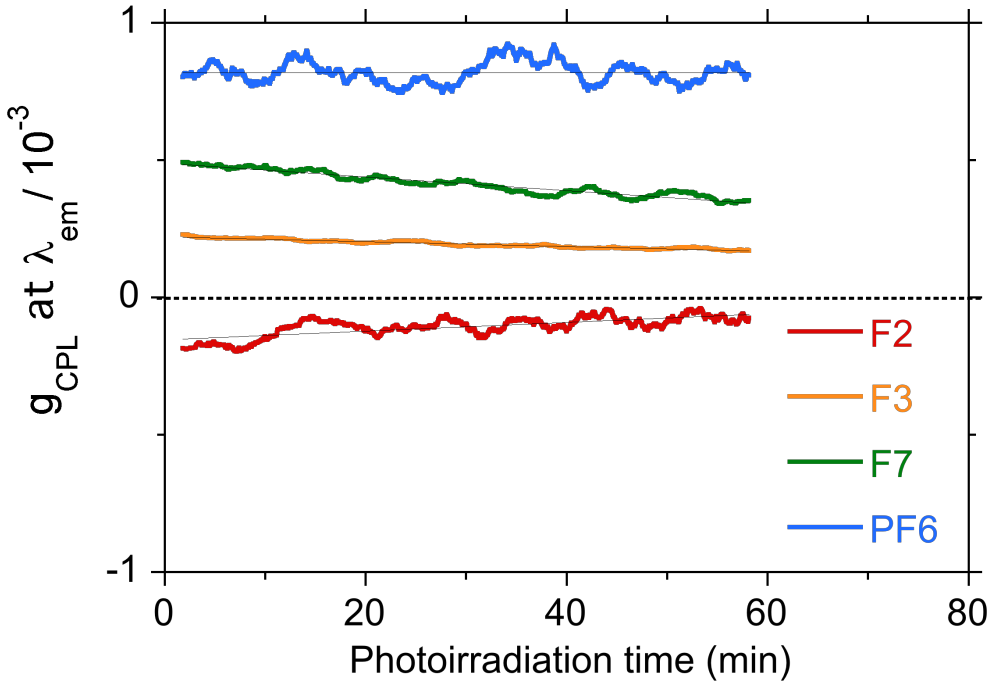


**Figure 3.7.** The change in the $g_{CPL}$ values of **F2** (orange), **F3** (red), **F7** (green), and **PF6** (blue) in **CTA** films at 293 K on a quartz substrate upon unpolarized light irradiation at the $Max_{CPL}$ wavelength. The raw data were obtained with a built-in program of a JASCO CPL-200 spectrofluoropolarimeter and plotted as $g_{CPL}$ = ellipticity (mdeg) /14320/ PL (DC in volts).

The changes in the $g_{CPL}$ values of **F2**, **F3**, **F7**, and **PF6** as a function of the photoirradiation time for 0–60 min upon unpolarized UV-light irradiation are displayed in Figure 3.7. The time-course $g_{CPL}$ magnitude values were evaluated at the CPL extremum.[8] The photoexcitation-induced racemization rate greatly depended on the

number of fluorene rings.[9] **PF6** embedded in the **CTA** films resulted in the greatest stability in the photoexcited state, maintaining the initial PL intensity after prolonged irradiation of 60 min. For comparison, **F2** in **CTA** caused rapid racemization and decreased to ≈45% of the initial $g_{CPL}$ value after 60 min of photoirradiation. Maintaining the $g_{CPL}$ value in the **CTA** film greatly depended on the number of fluorene rings in the following order: **PF6** >> **F7** > **F3** > **F2**.

### 3.6 Effect of Ester Groups on Chiral Transfer

We used **CTA-PF6** solutions that were dissolved in ethyl acetate (**EA**) and $CHCl_3$, respectively. In Figure 3.8, the films showed a switching Cotton effect during the CD/CPL experiments due to the specific proportions in the mixtures.

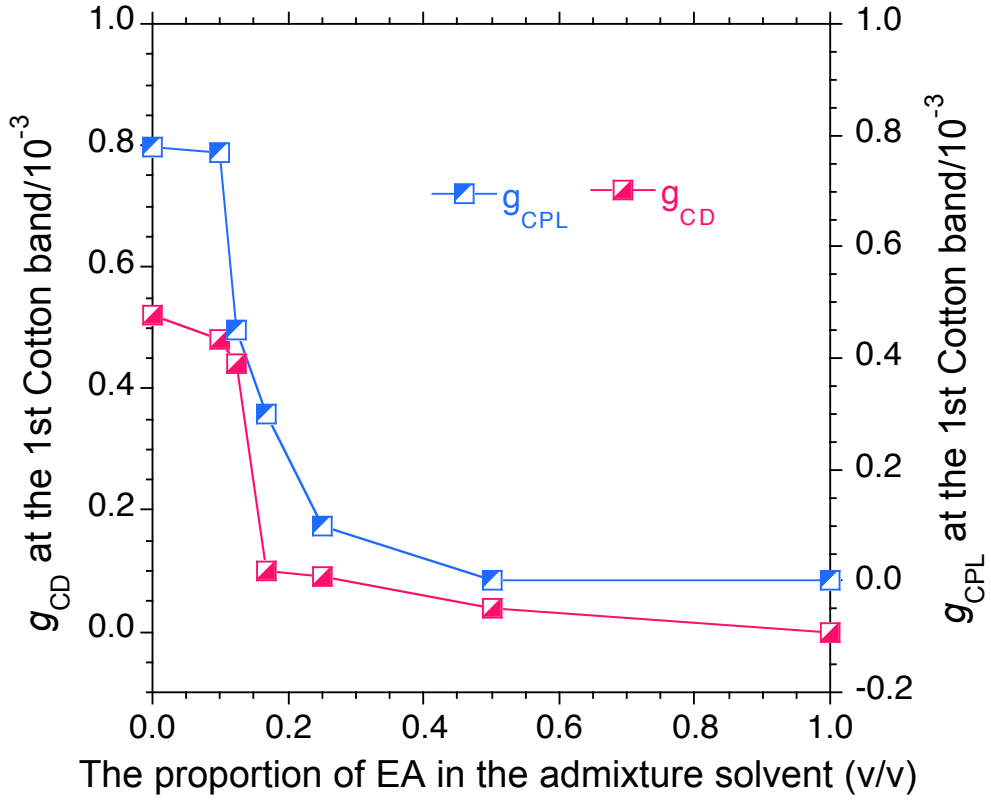


**Figure 3.8.** The $g_{CPL}$ values the **CTA-PF6** hybrid films at the first Cotton band as a function of the **EA** volume fraction. Excitation occurred at 355 nm.

The $g_{CPL}$ and $g_{CD}$ values in the **CTA** tended to decrease when the **EA** volume increased and approached constant values (Figure 3.8). The results indicate that the helicity and/or chirality inducing capabilities were enhanced by fluorene due to the intermolecular CO/HC interactions with **CTA**.

## 3.7 References


(1) Stipanovic, A. J.; Sarko, A. Molecular and Crystal Structure of Cellulose Triacetate I: A Parallel Chain Structure. *Polymer* **1978**, *19*, 3–8.

(2) Onofrei, M. D.; Dobos, A. M.; Ioan, S. In *Polymer Nanocomposites: Fundamentals and Applications*, Thakur, V. K. Ed., Wiley: Weinheim, Germany, Chapter 14, Nanocellulose Polymer Nanocomposites, pp 355–391.

(3) Dubois, J. C.; Barny, P. L.; Mauzac, M.; Noel, C. In. *Handbook of Liquid Crystals, Fundamentals High Regular weigt Liquid Crystal*, Demus, D., Goodby, J. W., Gray, G. W., Spiess, H. S., Vill, V., Eds.; Wiley-VCH Press: New York, **1998**; Vol 3, Chapter 2, pp 207–269.

(4) Eliel, E. L.; Wilen, S. H.; Mander, L. N. In *Stereochemistry of Organic Compounds*, Wiley-Interscience: New York, NY, **1994**. Chapter 13, pp 991–1118.

(5) Zyung, T.; Hwang, D. H.; Kang, I. N.; Shim, H. K.; Hwang, W. Y.; Kim, J. J. *Chem. Mater.* **1995**, *7*, 1499-1503.

(6) Tirapattur, S.; Belletête, M.; Drolet, N.; Leclerc, M.; Durocher, G. *Macromolecules* **2002**, *35*, 8889–8895.

(7) Kim, J. Y.; Lee, K.; Coates, N. E.; Moses, D.; Nguyen, T. Q.; Dante, M.; Heeger, A. J. *Science* **2007**, *317*, 222-225.

(8) Andrew, T. L.; Swager, T. M. *Macromolecules* **2008**, *41*, 8306-8308.

(9) Amara, J. P.; Swager, T. M. *Macromolecules* **2006**, *39*, 5753-5759.

(10) Oda, M.; Nothofer, H. G.; Scherf, U.; Šunjić, V.; Richter, D.; Regenstein, W.; Neher, D. *Macromolecules* **2002**, *35*, 6792–6798.

## Chapter 4. Chirality Transfer Experiments from Cellulose Triphenyl carbamate

### 4.1 Divergence of CD Spectra of CTPC in THF and $CH_2Cl_2$

Fluorene is a typical CD-silent material with a dynamic helicity. The presence of **CTPC** confers chiral characteristics to fluorene derivatives by an efficient transfer mechanism. Although the main chains of **CTPC** exhibited M-helix conformations,[1,2] fluorene derivatives showed helix inversion when dissolved in $CH_2Cl_2$ and THF (Figure 4.2, 4.3). We found great differences in **CTPC** in the CD spectra under the same concentration (Figure 4.1) and considered that the side chains of the **CTPC** led to a hypothesis for the helix inversion.[3]

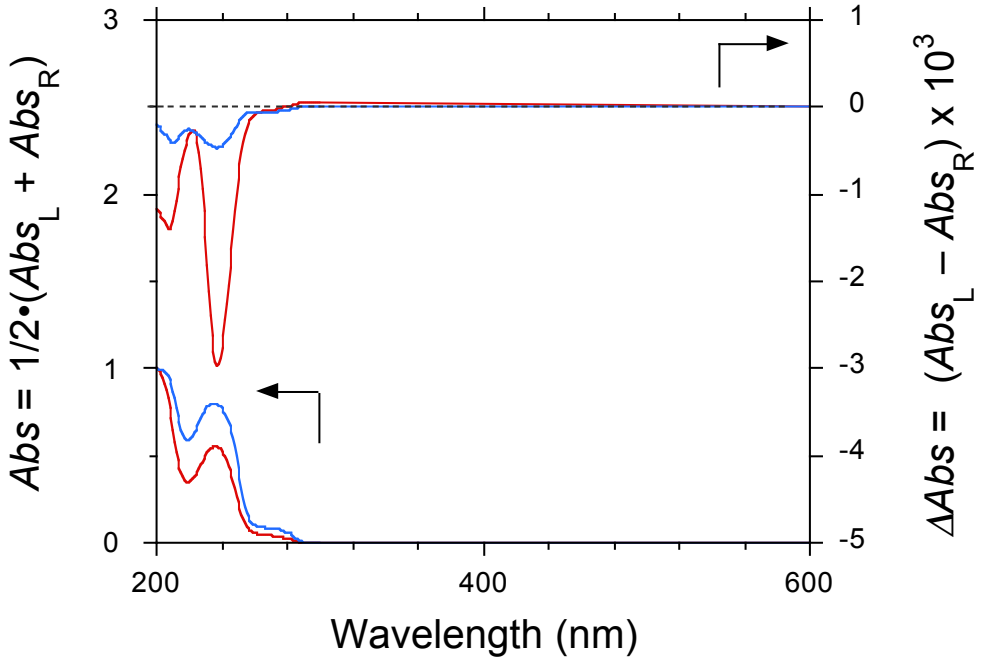


**Figure 4.1.** Normalized CD/UV-vis spectra of **CTPC** thin films after dissolved in THF (red) and $CH_2Cl_2$ (blue).

### 4.2 Solvent-Driven CD Inversion Capability of CTPC

The UV-vis and CD spectra of fluorene films with **CTPC** are shown in Figure 4.2. We found that the 9,9-di-n-hexylfluorene oligomer and polymer exhibited ideal mirror-overturn CD spectral characteristics that were optically active.

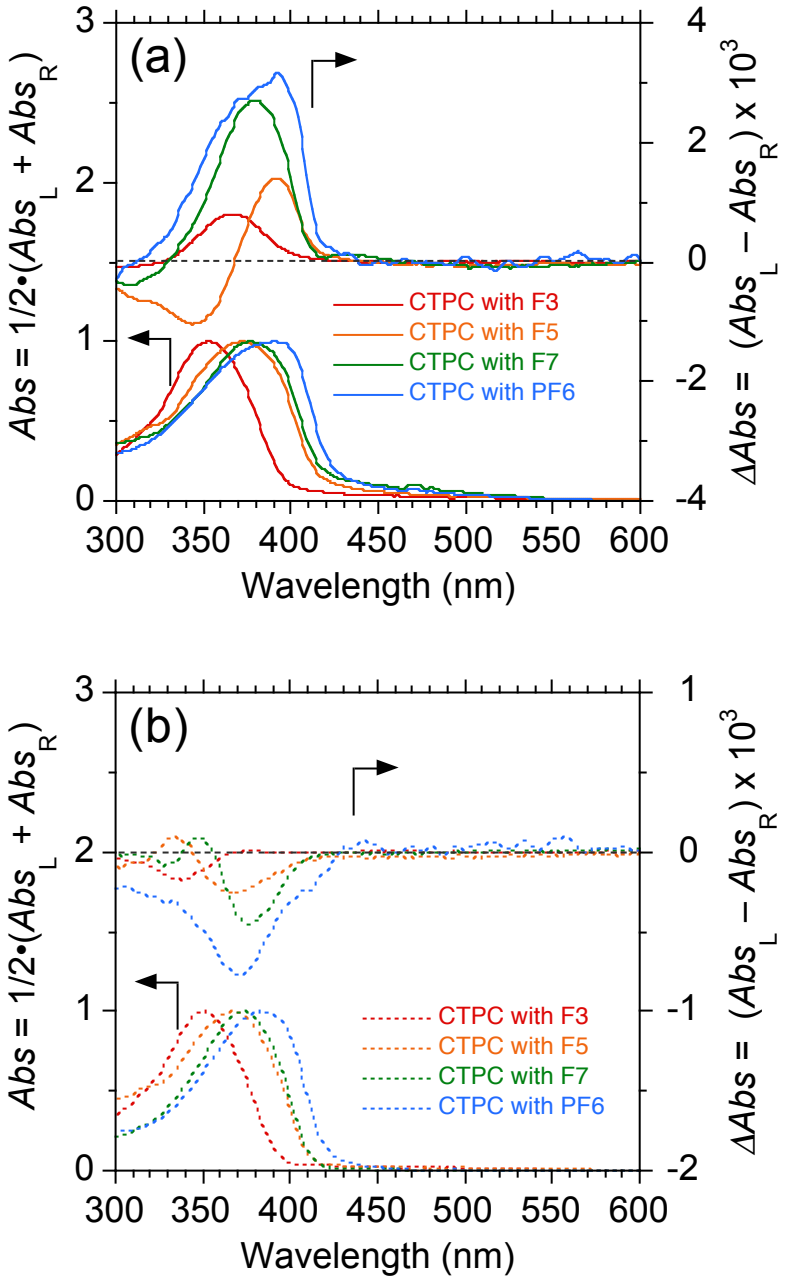


**Figure 4.2.** CD and UV-vis spectra of **F3**, **F5**, **F7**, and **PF6** with **CTPC** after dissolved in THF (a) and $CH_2Cl_2$ (b).

As shown in Figure 4.1, the fluorene oligomers and polymers exhibited intense positive Cotton effects, which constructed a P-helicity structure with its units twisted by chirality transfer in THF. The spectra were ascribed to the dihedral angles between the fluorene units when a helical conformation was induced by **CTPC**. Interestingly, the mirror-overturn Cotton effect appeared after dissolved in $CH_2Cl_2$. The negative signal indicated that the fluorene oligomers and polymers retained an M-helical structure with **CTPC** in $CH_2Cl_2$.

In the **CTPC-F5**, **CTPC-F7,** and **CTPC-PF6** films, a series of CD signals had (+) signs after dissolved in THF at the first Cotton band (Figure 4.1a): $g_{CD} = +3.17 \times 10^{-3}$ at 392 nm for **F3**, $g_{CD} = +1.68 \times 10^{-3}$ at 392 nm for **F5**, and $g_{CD} = +2.72 \times 10^{-3}$ at 380 nm for **F7**. Otherwise, a series of CD signals had (-) signs after dissolved in $CH_2Cl_2$ at the first Cotton band (Figure 4.1b): $g_{CD} = -0.83 \times 10^{-3}$ at 392 nm for **F3**, $g_{CD} = -0.26 \times 10^{-3}$ at 392 nm for **F5**, and $g_{CD} = -0.46 \times 10^{-3}$ at 380 nm for **F7**. Moreover, **PF6** afforded the largest $g_{CD}$ value at the first Cotton band, reaching $g_{CD} = +3.17 \times 10^{-3}$ at 392 nm after dissolved in THF and $g_{CD} = -0.83 \times 10^{-3}$ at 392 nm after dissolved in $CH_2Cl_2$.

The results demonstrate that macromolecular chirality transfer is possible between helical **CTPC** and non-helical fluorene oligomers and polymers due to the different solvent effects.[4]

### 4.3 Solvent-Driven CPL Inversion Capability of CTPC

Next, the CPL and PL spectra are show to demonstrate the helical structures of the fluorene derivatives for comparison in Figure 4.3. The CPL spectra exhibited mirror profiles in the films after dissolved in THF and $CH_2Cl_2$, meaning the opposite formation of helicity occurred due to chirality transfer.

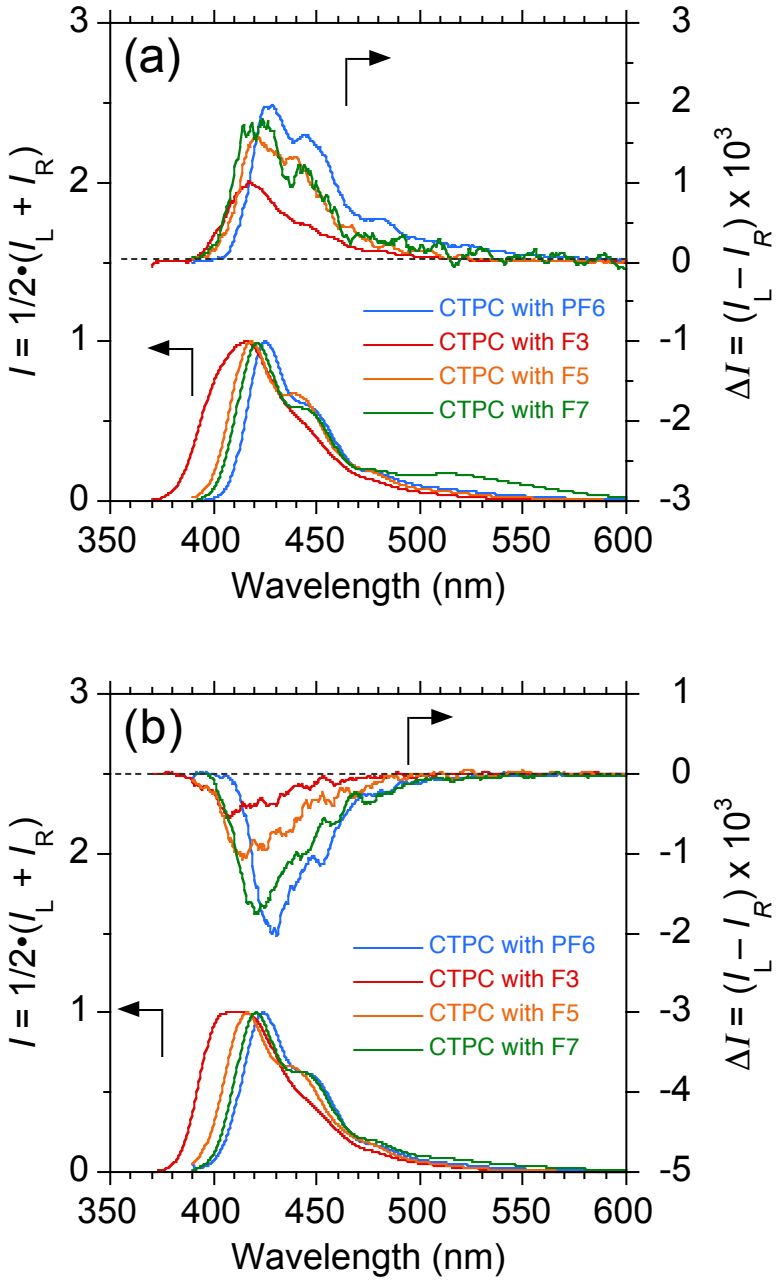


**Figure 4.3.** CPL and PL spectra of fluorene with **CTPC** after dissolved in THF (a) and $CH_2Cl_2$ (b).

The solvent effects that create M- and P-signs possess helix conformations.[5] The independent Cotton effect in the **CTPC-PF6** hybrid film resulted in the emission of left-handed circularly polarized light with P-helicity ($g_{CPL}$= +2.06×$10^{-3}$ at 428 nm) from the unit-twist on main chain due to THF (Figure 4.3a). This result is constant with the evidence that **PF6** had a structure change with P-helicity, which was confirmed by the same positive Cotton effect observed in the CD spectra. Meanwhile, the film exhibited a negative Cotton effect in the CPL spectra ($g_{CPL}$= -2.35×$10^{-3}$ at 430 nm), demonstrated by the emission of right-handed circularly polarized light with M-helicity due to $CH_2Cl_2$ (Figure 4.3b). Further, **F3**, **F5**, and **F7** had similar shapes in the CPL spectra (Figure 4.3). The luminescence dissymmetry factors ($g_{CPL}$) due to THF were $g_{CPL}$= +1.02 ×$10^{-3}$ at 417 nm for **F3**, $g_{CPL}$= +1.59 ×$10^{-3}$ at 419 nm for **F5**, and $g_{CPL}$= +1.87 ×$10^{-3}$ at 424 nm for **F7**. The luminescence dissymmetry factors ($g_{CPL}$) due to $CH_2Cl_2$ were $g_{CPL}$= -0.55 ×$10^{-3}$ at 408 nm for **F3**, $g_{CPL}$= -1.09 ×$10^{-3}$ at 414 nm for F5, and $g_{CPL}$= -1.77 ×$10^{-3}$ at 421 nm for **F7**.

On the basis of these results, we considered that **CTPC** might be an exceptional provider for demonstrating helix inversion induced by changing solvents.[6] It is easy to implement chirality transfer and helical directionality with this solvent effect.

### 4.4 Chirality Transfer Capability as a Function of Fluorene Repeating Unit

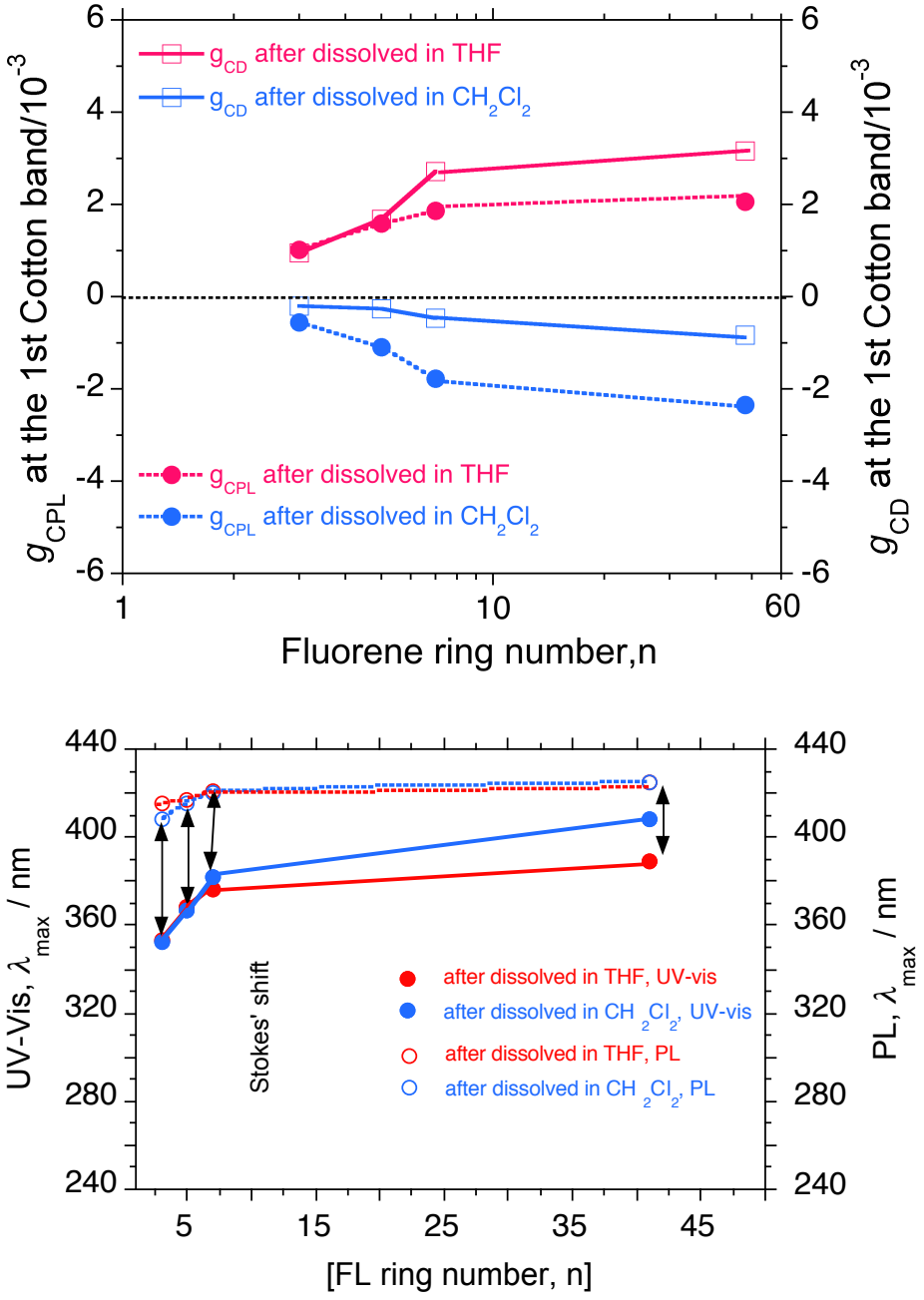


**Figure 4.4** (a) The $g_{CD}$ and $g_{CPL}$ values at the first Cotton band of the CD and of CPL spectra. (b) The $\lambda_{max}$ ($S_0 \rightarrow S_1$ transition) and $\lambda_{em}$ values ($S_1 \rightarrow S_0$ transition) of **CTPC** after dissolved in THF and $CH_2Cl_2$. The $\lambda_{max}$ ($S_0 \rightarrow S_1$ transition) and $\lambda_{em}$ values ($S_1 \rightarrow S_0$ transition) of CTPC after dissolved in THF and $CH_2Cl_2$ as functions of the fluorene ring number ($n$).

The $|g_{CPL}|$ and $|g_{CD}|$ values after dissolved in THF and $CH_2Cl_2$ tended to be linearly enhanced, when the fluorene repeating units increased, and they approached constant values (Figure 4.4a). This indicates that the helix and/or chirality inducing capabilities were enhanced due to the fluorene repeating units due to intermolecular non-covalent helix/chiral interactions with **CTPC**. Based on the CD spectral signs of **CTPC** using THF and $CH_2Cl_2$, we assumed that the side chains of **CTPC** were a deterministic factor of the twist sense in the fluorene oligomers and polymers in the ground states. In addition, the solvent effect induced the opposite CPL signs in the fluorene oligomers and polymers.

When $\pi$-electrons in $\pi$-conjugated molecular wires delocalize, the $S_0 \rightarrow S_1$ transition energy is lowered. The degree of twisting in a one-dimensional semiconductor should be responsible for charge carrier mobility in lower optical bandgap (*Eg, opt*) polymers, as indicated by the redshifts in PL and UV-vis bands.[7] The *Eg, opt* values obtained with the $\lambda_{max}$ and $\lambda_{em}$ values for the series of dialkylfluorene oligomers and polymers in the **CTPC** films after dissolved in THF and $CH_2Cl_2$ approximately linearly decreased as a function of the reciprocal fluorene ring number ($n$) (Figure 4.4b). The Stokes's shift between the *Eg, opt* from $\lambda_{max}$ and *Eg, opt* from $\lambda_{em}$ values tended to be smaller when the repeating number of fluorene rings increased. This indicates that very minimal reorganization in the fluorene main chain occurred in the photoexcited and ground states when the number of fluorene rings increased.[8]

### 4.5 Solvent Dependent Chirality Transfer Capability of CTPC

We used two kinds of **CTPC-PF6** solutions, which were dissolved in THF and $CH_2Cl_2$, respectively. In Figure 4.5, the films show a switching Cotton effect from the CPL experiments due to the proportion of the 0.5 mL THF-$CH_2Cl_2$ mixture. The unique CPL switching ability of the **CTPC-PF6** films is the first example in the field of solvent effect-induced films of chromophoric polymers.

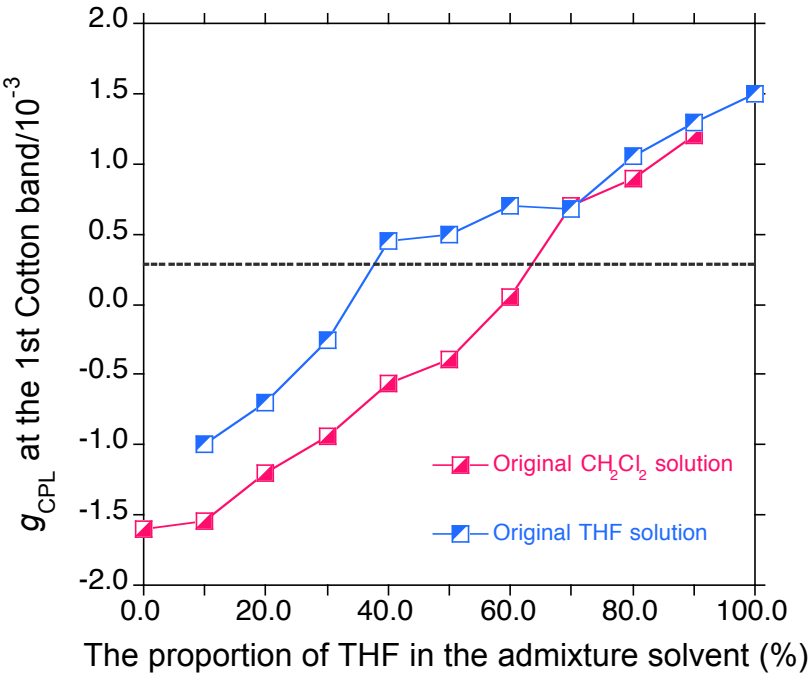


**Figure 4.5.** The $g_{CPL}$ values of the **CTPC-PF6** hybrid films at the first Cotton band as a function of the THF volume fraction. Excitation occurred at 355 nm.

Surprisingly, with the increase in the THF proportion, the $g_{CPL}$ showed linearly enhancement of the inversion. It was noted that although **CTPC** was a typical left-handed helix polymer, we considered that this inversion was due to the conformation changes of the side chains in **CTPC**.

## 4.6 References


(1) Chankvetadze, B.; Yashima, E.; Okamoto, Y. *Chem. Lett.* **1993**, 617−620.

(2) Yamamoto, C.; Yashima, E.; Okamoto, Y. *Bull. Chem. Soc. Jpn.* **1999**, *72*, 1815−1825.

(3) Shen, J.; Okamoto, Y. *Chem. Rev.* **2016**, *116*, 1094–1138.

(4) Nagata, Y.; Nishikawa, T.; Suginome, M. *J. Am. Chem. Soc.* **2014**, *136*, 15901–15904.

(5) Nagata, Y.; Nishikawa, T.; Suginome, M. *J. Am. Chem. Soc.* **2015**, *137*, 4070–4073.

(6) Dubois, J. C.; Barny, P. L.; Mauzac, M.; Noel, C. In. *Handbook of Liquid Crystals, Fundamentals High Regular weigt Liquid Crystal*, Demus, D., Goodby, J. W., Gray, G. W., Spiess, H. S., Vill, V., Eds.; Wiley-VCH Press: New York, **1998**; Vol 3, Chapter 2, pp 207–269.

(7) Zyung, T.; Hwang, D. H.; Kang, I. N.; Shim, H. K.; Hwang, W. Y.; Kim, J. J. *Chem. Mater.* **1995**, *7*, 1499-1503.

(8) Tirapattur, S.; Belletête, M.; Drolet, N.; Leclerc, M.; Durocher, G. *Macromolecules* **2002**, *35*, 8889–8895.

## Chapter 5. Mechanistic Aspects of Chirality Transfer Capability

### 5.1 Intermolecular Interactions between CTA/CABu and Fluorene Derivatives

5.1.1 Polysaccharide Helicity Transfer *versus* Glucose Chirality Transfer

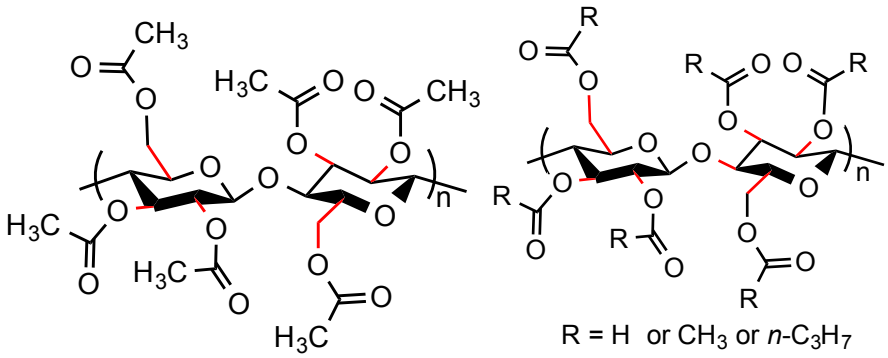


**Scheme 5.1** Chiral centers of the **CTA** and **CABu** side chains marked as red lines.

We noted that **CTA** and **CABu**, though possessing five chiral centers per pyranose ring, preferred left- and right-handed helicity in dilute $CHCl_3$.[1,2] We assumed that the three acetate groups per pyranose attached to these chiral centers offered chirality/helicity transfer capabilities[3] to the fluorenes. Although each acetate group itself was not chiral, their restricted rotational freedom along the C–O and C–C bonds (**Scheme 5.1**) led to the twisted geometry of the fluorene main chain in a preferred screw sense, as proven by the bisignate CD spectra.

Our demonstration has proven that helicity and/or chirality transfer protocols endowed by **CTA** and **CABu** are versatile, short-step approaches, that enable the thin film fabrication of CPL-/CD-functioned oligomers and polymers with a desired helix sense without the use of any chiral catalysts, long-step syntheses, and chiral side chains with (S)- or (R)-chirality.[4] In the series of fluorene oligomers, the (+) or (–) CPL sign was determined by choosing the helix preference of **CTA** and **CABu**, although the (+) CD sign at the first Cotton band was unchanged due to the dominant factor of the D-glucose

chiralities.

5.1.2 WAXD Analysis of **CTA** and **CABu** Films

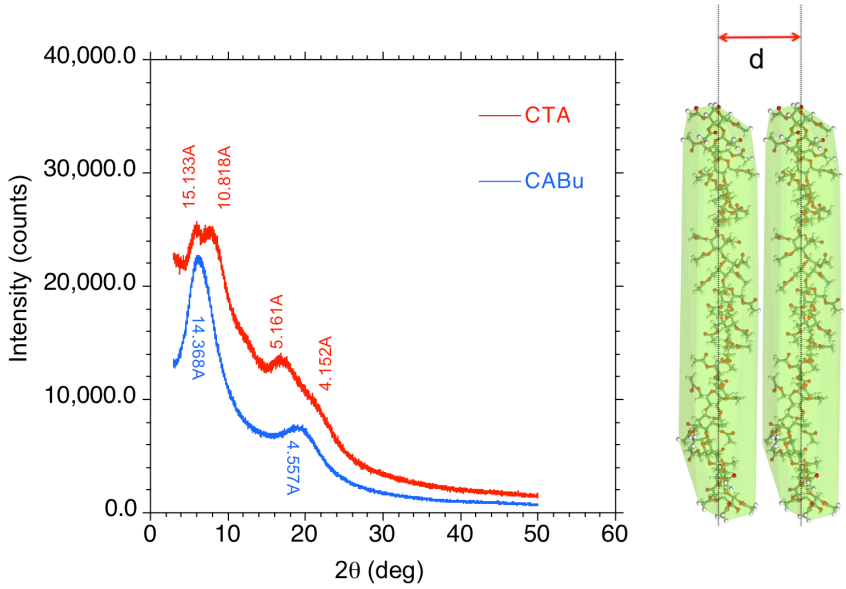


**Figure 5.1.** Comparison of the WAXD profiles of the **CTA** (red) and **CABu** (blue) on a Si substrate cast from a chloroform solution in air.

Although the similar scenario between **CABu** and the fluorenes was possible, the capability of helicity and/or chirality transfer might have been rather weak because the C-H/O=C interactions between the *n*-alkyl C-*H* and *n*-butylate *O*=C groups may have been suppressed due to the existence of bulkier *n*-butylate groups and due to a mixture of the *n*-butylate and acetyl groups. The difference between **CABu** and **CTA** is reflected in the WAXD profiles of the **CTA** and **CABu** films deposited on Si substrates, as given in Figure 5.1. The **CTA** film had two distinct diffraction peaks at 10.818 Å and 15.133 Å and two broad peaks at 4.152 and 5.1613 Å, while the **CABu** film had two broad peaks at 14.368 Å and 4.55 Å, indicating an inherently glassy state.[5] Actually, the $|g_{CD}|$ values in **CABu** were greatly reduced relative to those in **CTA**.

5.1.3 The Origin of the Bisignate CD Band as Evidence of the Twisted Fluorene Main Chain

Because the twist of the polymer backbone is central to understanding the optical activity, we searched for the global and local minimum conformations of the 9,9-dimethylfluorene trimer using MM calculations with a grid scan method as a function of two dihedral angles with an increment of 20° to calculate the CD spectra of these conformers (Figure 3.7).

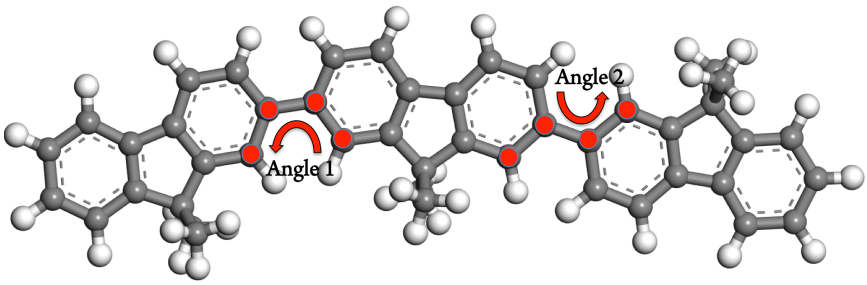


**Figure 5.2.** The standard dihedral angles in the trimer model.

Next, a potential energy surface scan method, followed by structural optimizations at torsion angles between the neighboring fluorene units, was carried out using DFT calculations at the B3LYP/6-31G(d) level.[6] The calculated potential energy surfaces associated with all the transition dipoles and magnetic moments as a function of the torsion angles are given (Figure 3.8). The calculated CD signals of the fluorene trimer arose from the twisted fluorene units. The four stable conformers with the lowest energy were assigned as ID33 (Figure 5.4), ID38 (Figure 5.5), ID83 (Figure 5.6), and ID88 (Figure 5.7).

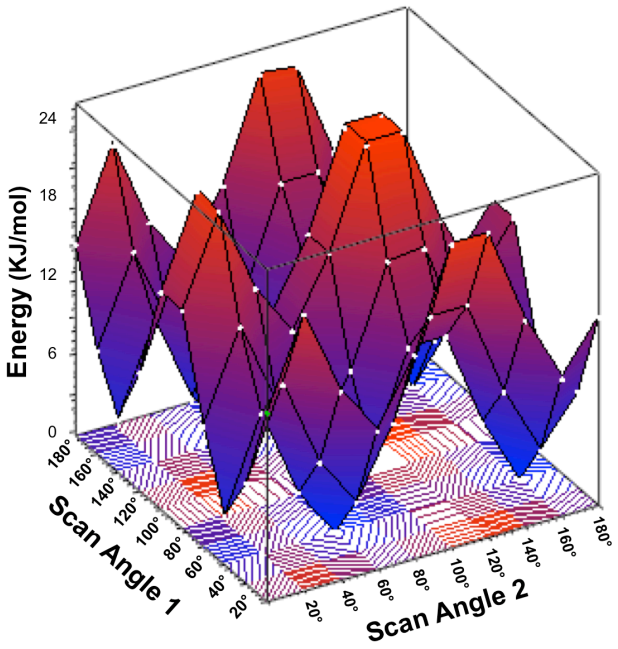


**Figure 5.3.** Potential energy surface scan of the trimer model.

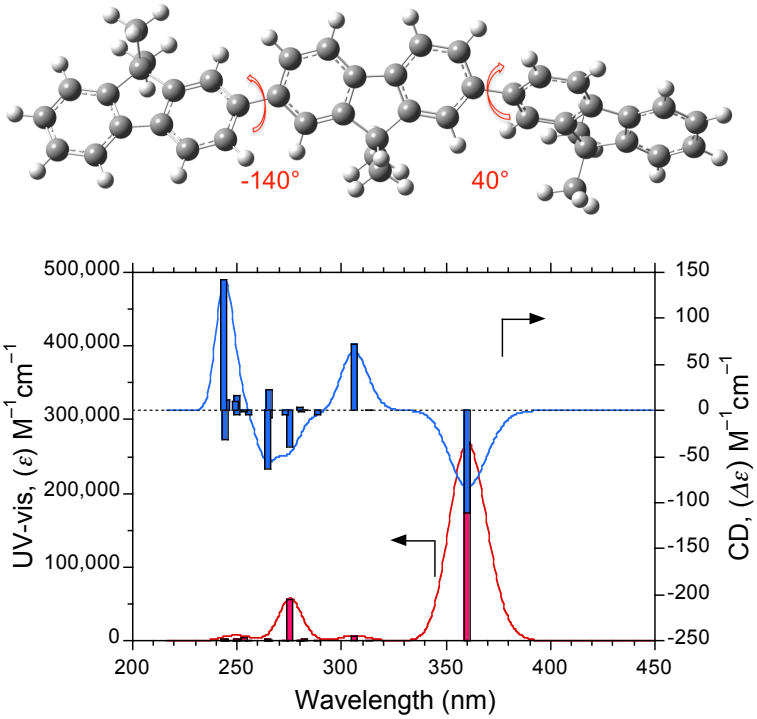


**Figure 5.4.** Simulated CD and UV-vis spectra of ID33 with a full width at half maximum of 0.1 eV.

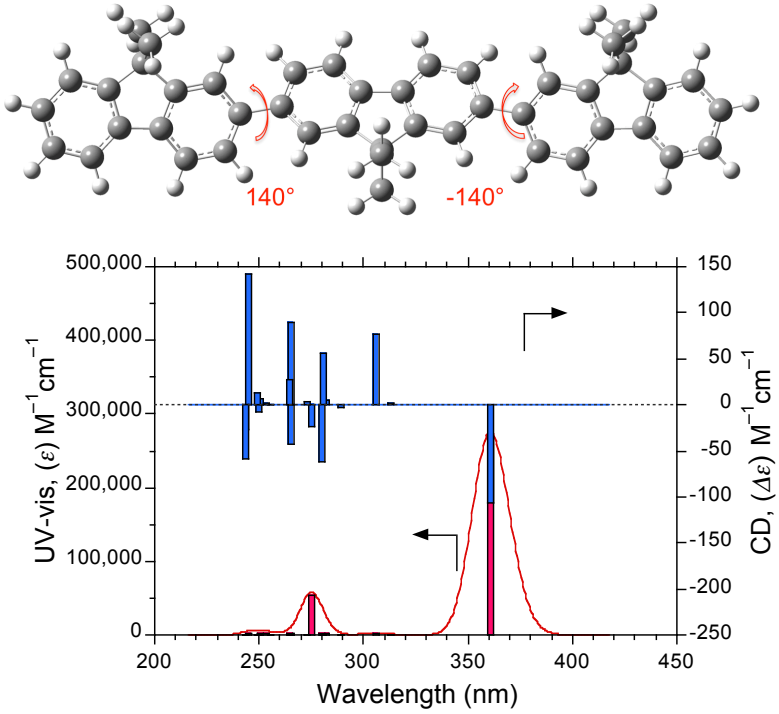


**Figure 5.5.** Simulated CD and UV-vis spectra of ID38 with a full width at half maximum of 0.1 eV.

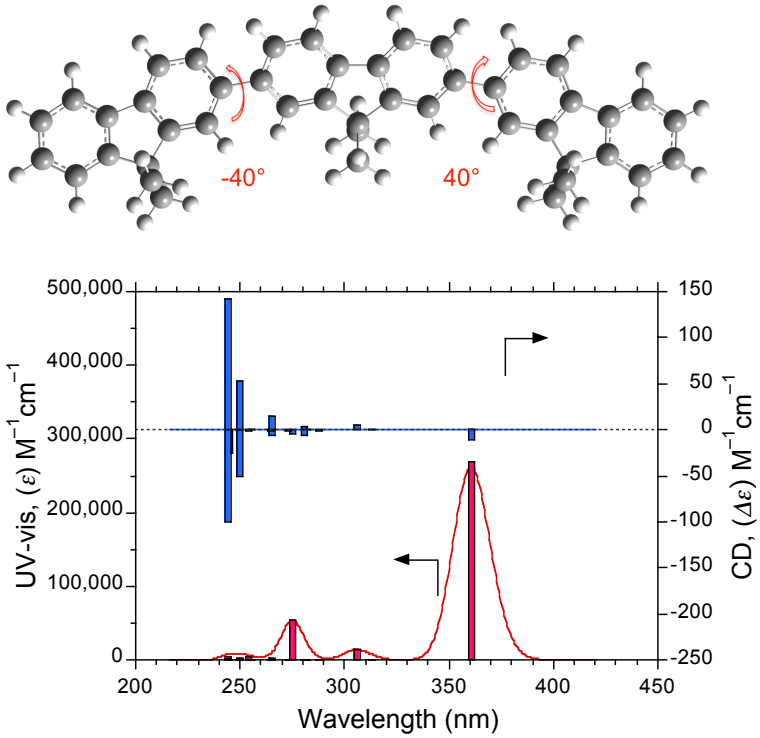


**Figure 5.6.** Simulated CD and UV-vis spectra of ID83 with a full width at half maximum of 0.1 eV.

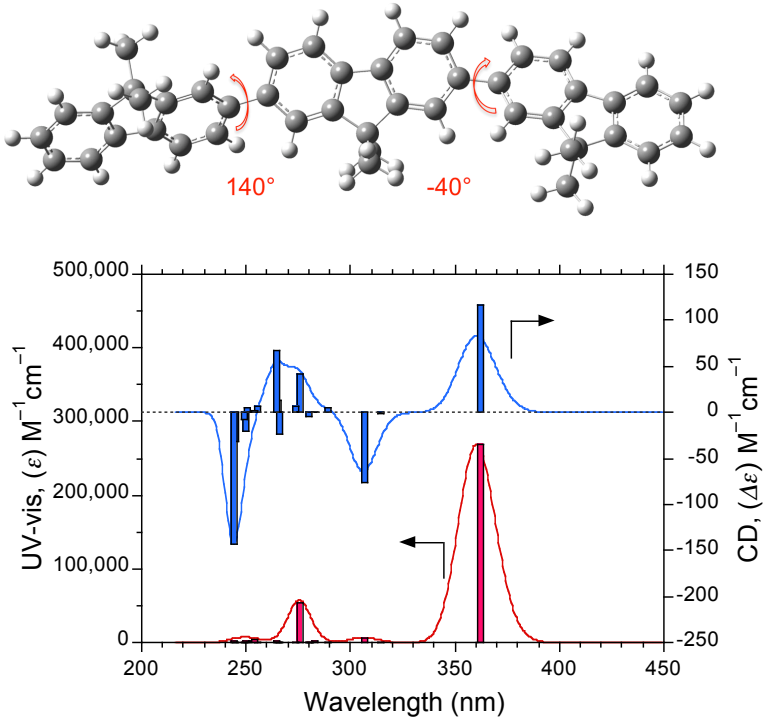


**Figure 5.7.** Simulated CD and UV-vis spectra of ID88 with a full width at half maximum of 0.1 eV.

Among these, the ID88 data set afforded simulated CD and UV-vis spectra with a full width at half maximum of 0.1 eV because the inherent C-H/H-C repulsions between the fluorine rings were responsible for the twisted geometry. It is evident that the calculated CD spectra of the 9,9-dimethyfluorene trimer as a model of **F3** in the **CTA** and **CABu** films revealed bisignate signal with $g_{CD} = +0.31 \times 10^{-3}$ at the first Cotton band of 362.47 nm and $g_{CD} = -9.34 \times 10^{-3}$ at the second Cotton of 306.81 nm. These CD magnitudes and signs agreed well the following experimental results: in **CTA**, $g_{CD} = +0.08 \times 10^{-3}$ at 375 nm and $g_{CD} = -0.04 \times 10^{-3}$ at 330 nm (Figures 3.2), while, in **CABu**, $g_{CD} = +0.04 \times 10^{-3}$ at 378 nm and $g_{CD} = -0.08 \times 10^{-3}$ at 333 nm (Figure 3.4).

The (+) CD and UV π–π* bands at 362.47 nm were ascribed to the electric dipole enabled and magnetic-dipole allowed $S_0 \rightarrow S_1$ transitions. This transition occurred parallel to the long axis of the fluorene and occurred from the HOMO (anti-symmetric

wavefunction to the pseudo-$\sigma_h$ plane) to the LUMO (symmetric to the $\sigma_h$ plane) (98%). In contrast, the (–) sign CD and weak UV $\pi$–$\pi^*$ bands at 306.81 nm were ascribed to the electric dipole forbidden magnetic transitions with phantom $S_0 \rightarrow S_2$ transition with f = 0.0008. These transition were perpendicular to the fluorene long axis, occurring from the HOMO–1 (symmetric) to the LUMO (symmetric) (57%) and from the HOMO (anti-symmetric) to the LUMO+1 (anti-symmetric) (38%) (Figure 5.8).

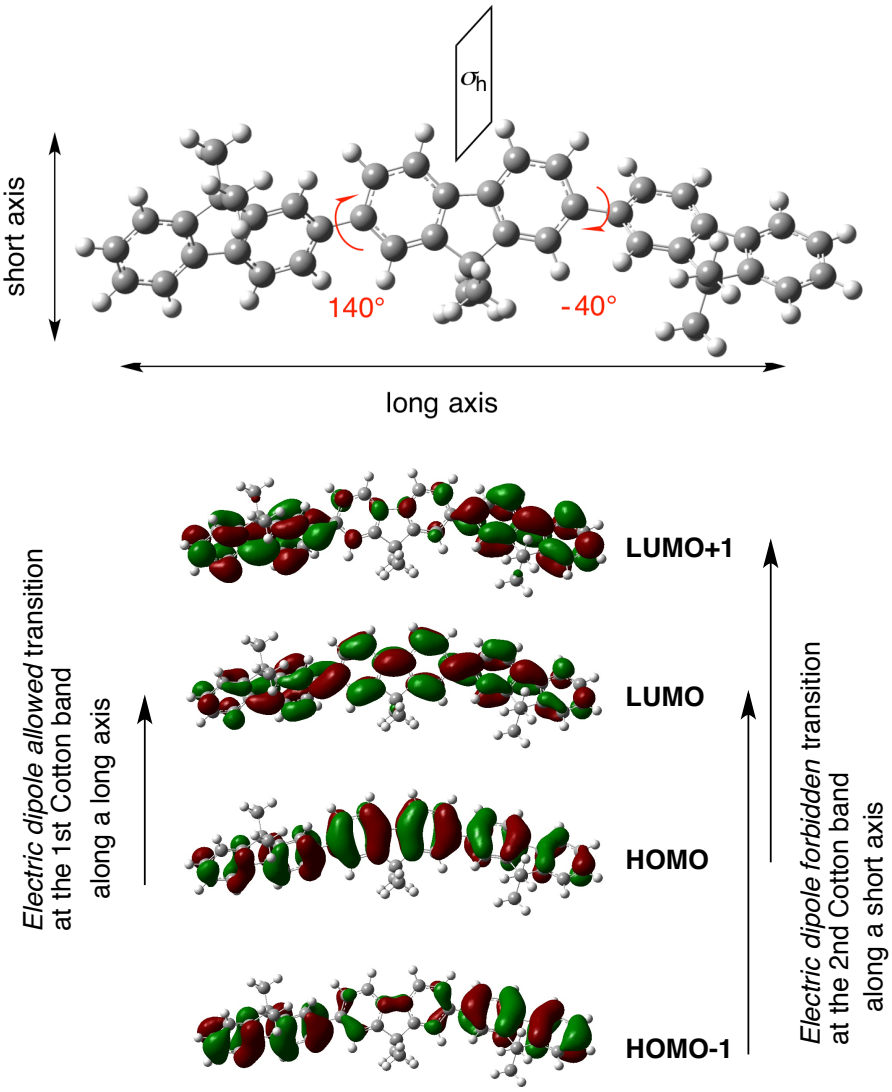


**Figure 5.8.** ID88 model with dihedral angles of 140° and -40°. (Bottom) Isosurfaces of the highest occupied molecular orbitals (HOMOs) and lowest unoccupied molecular orbitals (LUMOs).

These results indicate that the 9,9-dimethlfluorene trimer as a computational model is valid using TD-DFT simulations. The twisted fluorene rings with dihedral angles (e.g., 140° and 40°) revealed apparent bisignate CD bands at 375 nm and 300 nm and a mono sign CPL band at 385 nm. The origin of the bisignate CD was, thus, not due to the so-called exciton couplet of the dimeric- and self-assemblies being assorted chirally. The twist geometry was induced solely by the embedded long sequences of D-glucose residues possessing the main helicity and point chirality at the glucose residues.

5.1.4 C-H/O=C Interactions between Dioctylfluorene and **CTA** Oliogomers by Computer Modeling

In the previous section, we showed the helicity and/or chirality transfer of **PF8**, leading to retention and inversion in the CD and CPL signals from **CTA** and **CABu**. Herein, we focus on the mechanism of the optical activity by **PF8** depending on the dihedral angles of the main chain and possible intermolecular interactions between **PF8** and **CTA**. MD simulations were carried out using the Materials Studio Forcite module with a universal force field (UFF).[7,8] The **CTA** contains three achiral methyl ester groups that contributed to the intermolecular C-H/O=C hydrogen bonds. The hydrogen bonds should have led to certain chiral and helical structures.

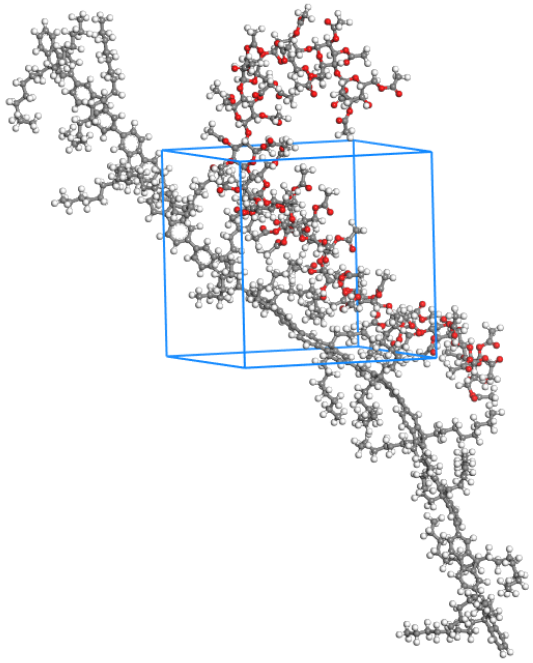

**Figure 5.9.** An optimized molecular model of **CTA** and **PF8** equilibrated at 300 K obtained with the Forcite module from Materials Studio.

In these simulations, we designed a hybridized system of **CTA** with 12-units and **PF8 with** 12-units in order to interpret the intermolecular interactions, followed by the induction of helical and/or chiral motifs, as shown in Figure 5.9. The optimized **CTA**

with 12-units and **PF8** with 12-units were obtained from Forcite Geometry Optimization. The two structures were connected to form a polymer hybrid system.

After generating the initial hybrid polymer structure, the geometry was refined using a self-consistent iterative procedure at pressures of 0.01 GPa and 0.1 MPa until the calculations converged. To optimize the energy minimization, the polymer hybrid system was annealed at high temperatures using Forcite Anneal Dynamics; the model was finally equilibrated at 300 K and one atmosphere of pressure for 150 ps using the NPT method of classical MD.[9]

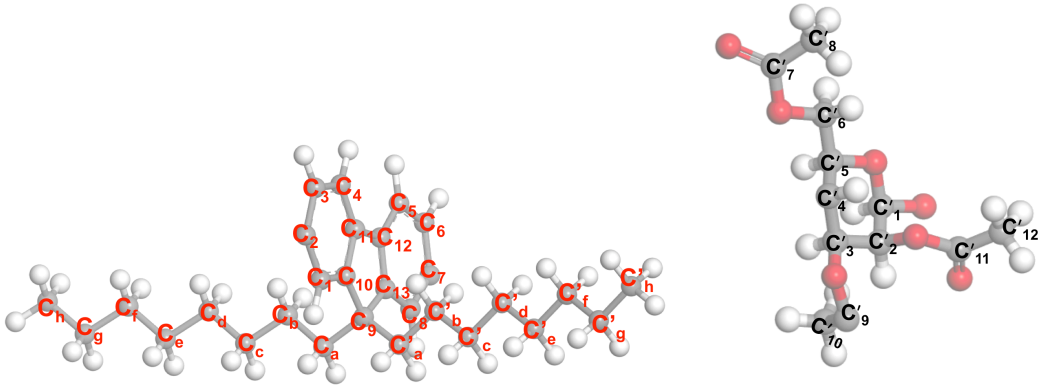

**Figure 5.10.** Model structures of **PF8** and **CTA**.

We indicate the backbone numbering and side-chain atoms in Figure 5.10. To consider the effects of the helicity and chirality transfer as well as the twist of the polyfluorene, the **CTA** backbone generally revealed three unique C=O bonds in the acetyl groups of the backbone.

The MD simulations indicated the existence of the intermolecular C-H/O=C interactions between **CTA** and **PF8 (**Figure 5.11**)**. The distances between H and O that ranged from 2.49 and 2.86 Å were greatly shortened compared to their van der Waals interaction distance of 3.0 Å.[10,11] Huge numbers of C-H/O=C interactions caused by the

**CTA** framework were thus responsible for transforming the helicity and/or chirality, followed by induction of the left–right imbalance, leading to optically active **PF8** for the detection of the CD and CPL signals (Table 5.1).

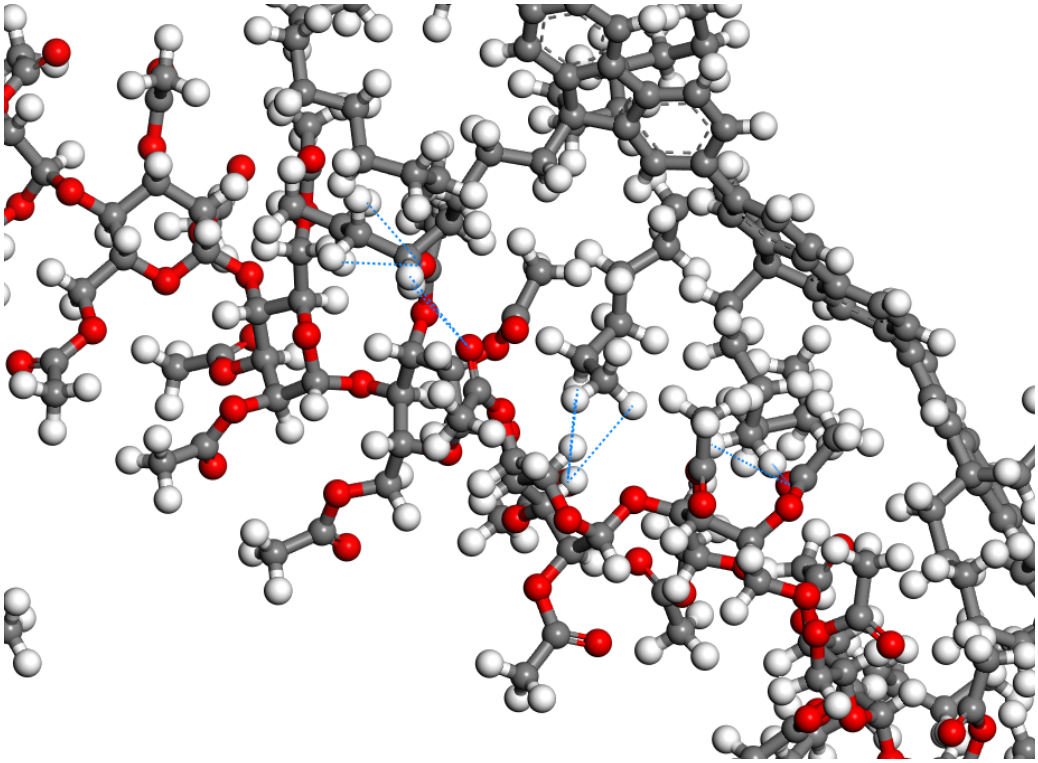

**Figure 5.11.** Simulated C-H/O=C interactions between **PF8** and **CTA**.

**Table 5.1.** The distances between selected C–*H* and *O*=C groups with C–H/O=C interactions. Distance 1 is the distance from one proton of an n-octyl group to the *O*=C, while distance 2 is the distance from another proton to the *O*=C from the MD calculation.

| Group name | Distance 1 (Å) | Distance 2 (Å) |
|---|---|---|
| $C'_9$=O/H-$C_a$ | 2.75 | 3.40 |
| $C'_9$=O/H-$C_b$ | 2.84 | 4.37 |
| $C'_9$=O/H-$C_c$ | 2.61 | 4.31 |
| $C'_7$=O/H-$C_e$ | 2.86 | 4.42 |
| $C'_{11}$=O/H-$C_e$ | 2.70 | 4.40 |
| $C'_{11}$=O/H-$C_g$ | 2.49 | 2.60 |

5.1.5 1D-/2D-NMR for Intermolecular C-H/O=C Interactions

We conducted 1D CP-MAS solid-state NMR experiments that allowed us to directly prove the existence of intermolecular C-*H*/*O*=C interactions between **CTA** and **PF8**, as predicted by the MD/MM calculations. The CP-MAS solid-state $^{13}$C-NMR spectra were analyzed by considering the **CTA** and **PF8** structures (Figure 5.12). The chemical shifts of **CTA** and **PF8** by 1D CP/MAS solid-state $^{13}$C NMR are shown in Table 5.2, 5.3.[12-15]

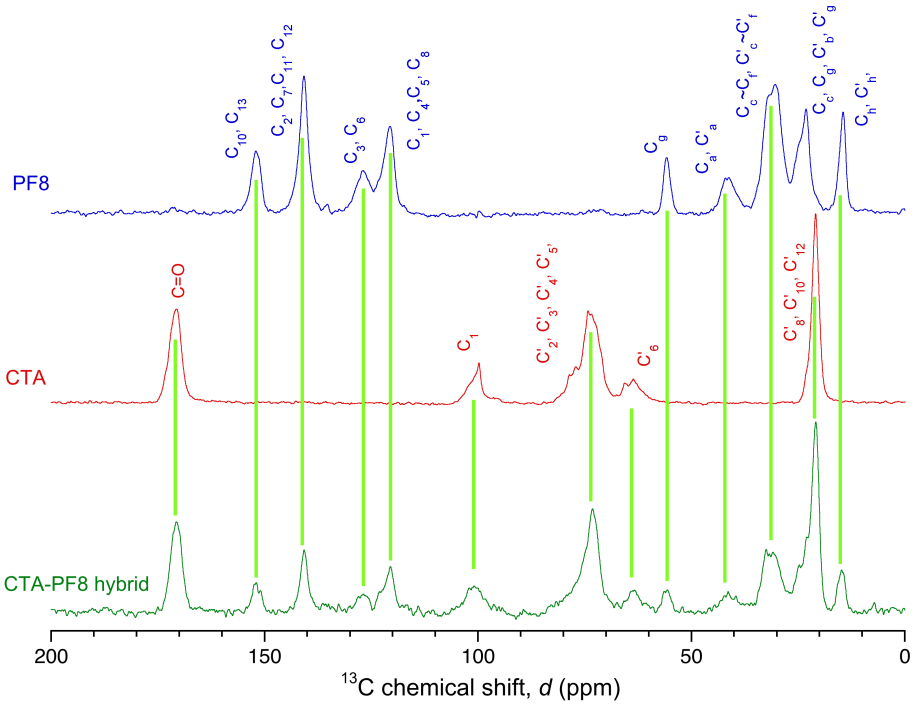


**Figure 5.12.** 1D CP/MAS solid-state $^{13}$C NMR spectra of the **CTA-PF8** hybrid (green), **CTA** (red), and **PF8** (blue).

**Table 5.2.** Chemical shifts of **CTA** from 1D CP/MAS solid-state $^{13}$C NMR.

| Group name | Chemical shifts (ppm) |
|---|---|
| C=O | 170.6 |
| $C'_1$ | 102.1 |
| $C'_2$, $C'_3$, $C'_4$, $C_5$ | 73.1 |
| $C'_6$ | 63.8 |

**Table 5.3.** Chemical shifts of **PF8** from 1D CP/MAS solid-state $^{13}C$ NMR.

| Group name | Chemical shifts (ppm) |
|---|---|
| $C_{10}$, $C_{13}$ | 152.06 |
| $C_2$, $C_7$, $C_{11}$, $C_{12}$ | 140.7 |
| $C_3$, $C_6$ | 126.8 |
| $C_1$, $C_4$, $C_5$, $C_8$ | 120.6 |
| $C_9$ | 55.67 |
| $C_a$, $C'_a$ | 41.75 |
| $C_f$,$C_c$,$C_d$,$C_e$<br>$C'_f$, $C'_c$, $C'_d$, $C'_e$ | 30.41 |
| $C_g$, $C_{f,}$<br>$C'_g$, $C'_f$ | 23.2 |
| $C_h$, $C'_h$ | 14.43 |

We also conducted 2D $^1H$–$^{13}C$ HETCOR solid-state NMR experiments that allowed us to prove the intermolecular C-H/O=C interactions between **CTA** and **PF8**.[16,17] The predicted interactions were detected by integrating phase modulated Lee Goldburg (PMLG) homonuclear decoupling in 2D $^1H$–$^{13}C$ HETCOR NMR,[18] which measured the $^{13}C$–$^1H$ magnetic dipolar coupling between the $^{13}C$=O and $^1H$-C groups due to the nuclear Overhauser effect (NOE).[19] This method was established to discuss the internuclear distances and to determine the molecular structures.

The PMLG 2D $^1H$–$^{13}C$ HETCOR NMR spectra of the **CTA-PF8** hybrid provided clear evidence of an intense cross peak between the methylene protons of the *n*-octyl groups of **PF8** ($\delta_H$ = 2.55 ppm) and $^{13}C$=O ($\delta_C$ = 170.6 ppm, achiral acetyl of **CTA**), marked in the red region of Figure 5.13. Because polarization transfer from $^1H$ to $^{13}C$ atoms usually occurs at distances shorter than 5.0 Å,[20] the intense cross peak, obeying the scaling law of interatomic distance $d^{-6}$,[21] directly supported the presence of the closest distances (< 5.0 Å) between $^1H$-C (due to *n*-octyl methylene of **PF8**) and $^{13}C$=O (due to acetyl of **CTA**) (Figure 5.14, Table 5.4).[10,11]

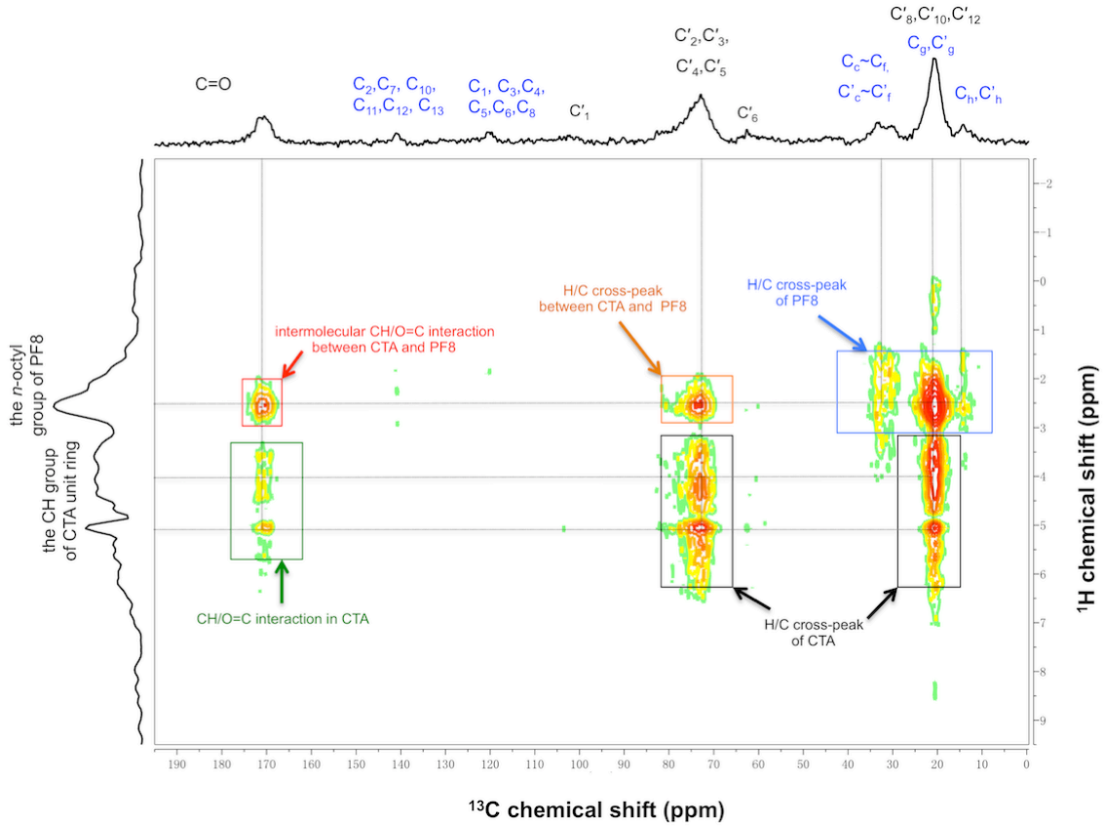


**Figure 5.13.** The PMLG 2D solid-state $^{1}H$-$^{13}C$ HETCOR NMR spectrum of the CTA-PF8 hybridized solid (proton pulsed, C13 observed). The 1D CP/MAS $^{13}C$ NMR spectrum is displayed above this 2D spectrum.

The 2D $^{1}H$–$^{13}C$ NMR spectra of the **CTA-PF8** hybrid clearly underline the close distances and contact positions of the polymers. We modeled the interactions and calculated the distances from the guest protons to O=C. The close contact between the CH group of **PF8** and O=C group of **CTA** provided strong evidence.

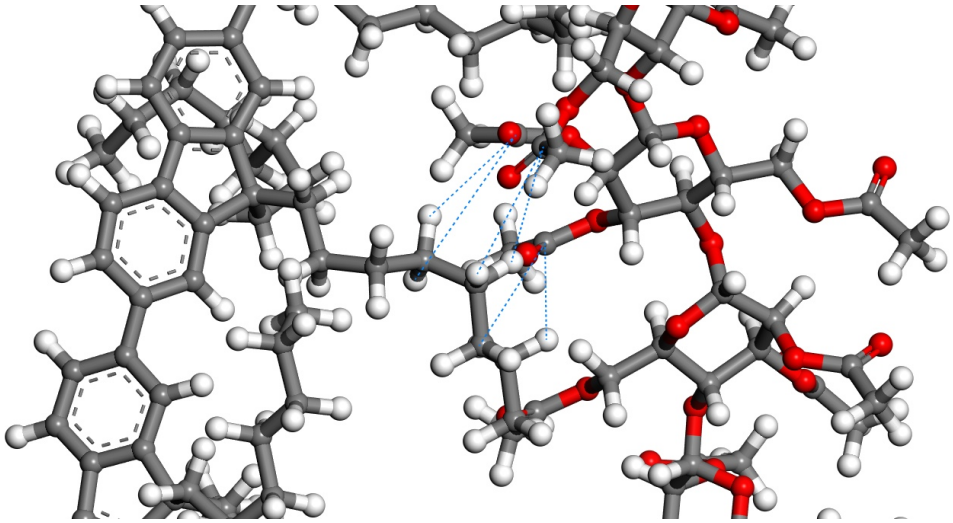

**Figure 5.14.** The distances between selected C–*H* and O=*C* groups of the C–H/O=C interactions.

**Table 5.4.** Distance 1 is the distance from one proton of an n-octyl group to *O*=C, while Distance 2 is the distance from another proton to O=*C* from the MD calculation.

| Group name | Distance 1 (Å) | Distance 2 (Å) |
|---|---|---|
| $C'_9$=O/H-$C_a$ | 3.40 | 3.47 |
| $C'_9$=O/H-$C_b$ | 3.60 | 4.51 |
| $C'_9$=O/H-$C_c$ | 3.25 | 4.40 |
| $C'_7$=O/H-$C_e$ | 2.88 | 4.60 |
| $C'_{11}$=O/H-$C_e$ | 3.73 | 4.02 |
| $C'_{11}$=O/H-$C_g$ | 3.09 | 3.09 |

## 5.2 Intermolecular and Intramolecular Interactions of CTPC and Fluorene Systems

### 5.2.1 Side-Chain Dependence of CTPC

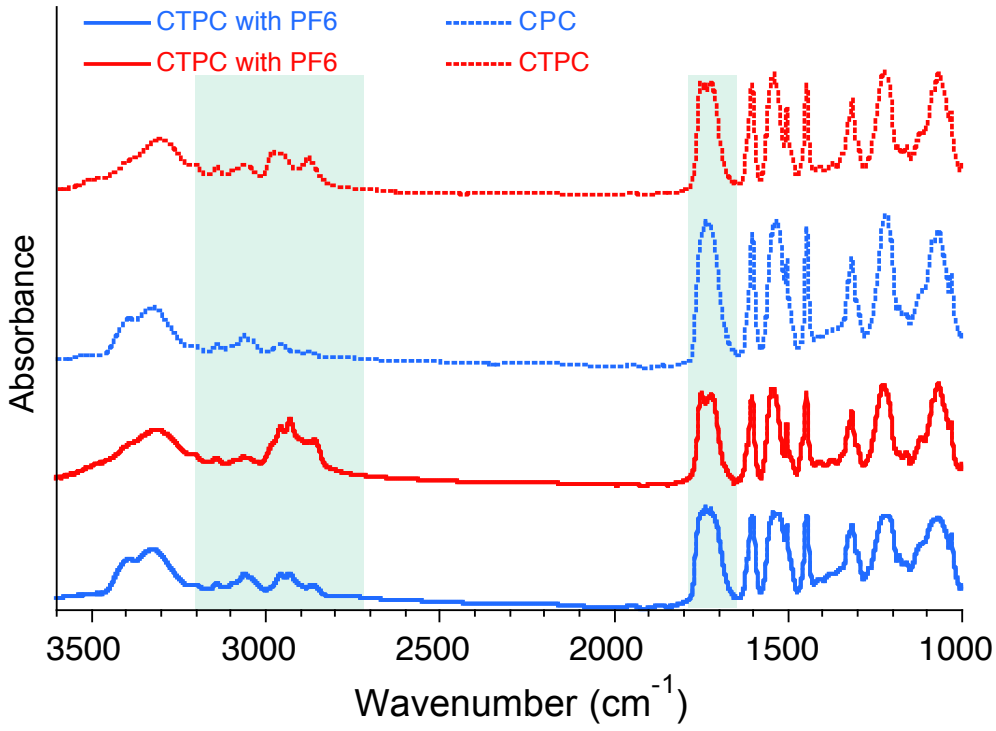


**Figure 5.15.** FTIR spectra of the **CTPC** films after treatment with THF (red lines) and $CH_2Cl_2$ (blue lines).

Because cellulose derivatives are rich in hydrogen bonds, H-bonds may be formed on the side chains of **CTPC** in different solvents. Therefore, we employed FTIR to characterize the H-bond interactions (Figure 5.15). By investigating the IR properties, the intrachain and interchain structures of the branches were unambiguously identified. The IR spectra of the NH stretching region for **CTPC** supported this suggestion. The FTIR band related to the NH band with a strong shift at 3322 and 3301 $cm^{-1}$ can be observed in Figure 5.16a. Simultaneously, the absorption features changed at 1540 and 1527 $cm^{-1}$ (Figure 5.16b). The δ(NH) band shifted to a higher wavenumber in THF, and the ν(NH) band shifted to a lower wavenumber in $CH_2Cl_2$. The shifts are indicative of the hydrogen bond interactions between the amides[22] and imply that the optical activities of the

fluorene oligomers and polymers depended on the structural changes of the **CTPC** branch chains. We considered the **CTPC** to be a promising polymeric switch and demonstrated its helix inversion induced by the change of solvents (Scheme 5.2).

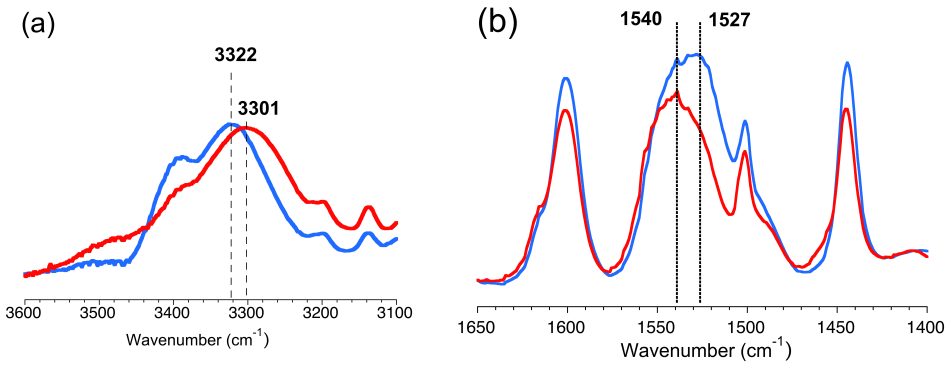


**Figure 5.16.** FTIR spectra of the CPTC films after treatment with two solutions at room temperature. The spectra are shown for ν(NH) (a) and δ(NH) (b). The blue curve refers to dissolved in $CH_2Cl_2$, and the red curve refers to dissolved in THF.

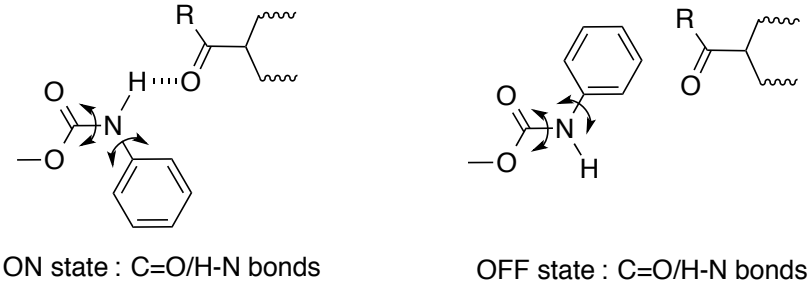


**Scheme 5.2.** The NH/O=C switch on the side-chain of **CTPC**.

5.2.2 WAXD Analysis for Intermolecular Interactions

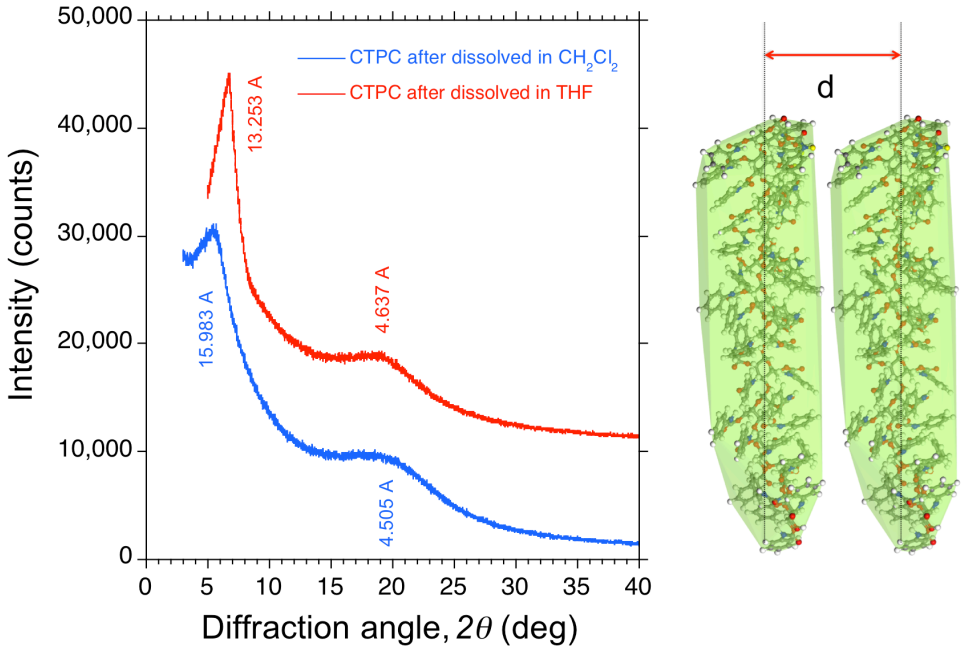


**Figure 5.17** WAXD profiles of **CTPC** after dissolved in THF (red) and $CH_2Cl_2$ (blue) solutions.

In the WAXD intensity profiles of the anisotropic **CTPC**-THF/$CH_2Cl_2$, we can find that the intensity curves provided two diffraction peaks at lower angular positions of 2θ = 4° to 7°. The distances between the polymer chains were measured from the low-angle peaks as 13.253 Å (THF) and 15.983 Å ($CH_2Cl_2$) (Figure 5.17). The differences between the distances and the diffraction peak sharpness were based on the orderliness of the periodic helical structure.[5] The ordered structure in the THF illustrated stronger CD signals than the structure in $CH_2Cl_2$. The changes in the spectral features, once again, confirmed that the solvent induced the preferred direction of the **CTPC** structure and maintained the chiral structure in the branch chains.[23,24]

5.2.3 DSC Analysis of NH/O=C Interactions

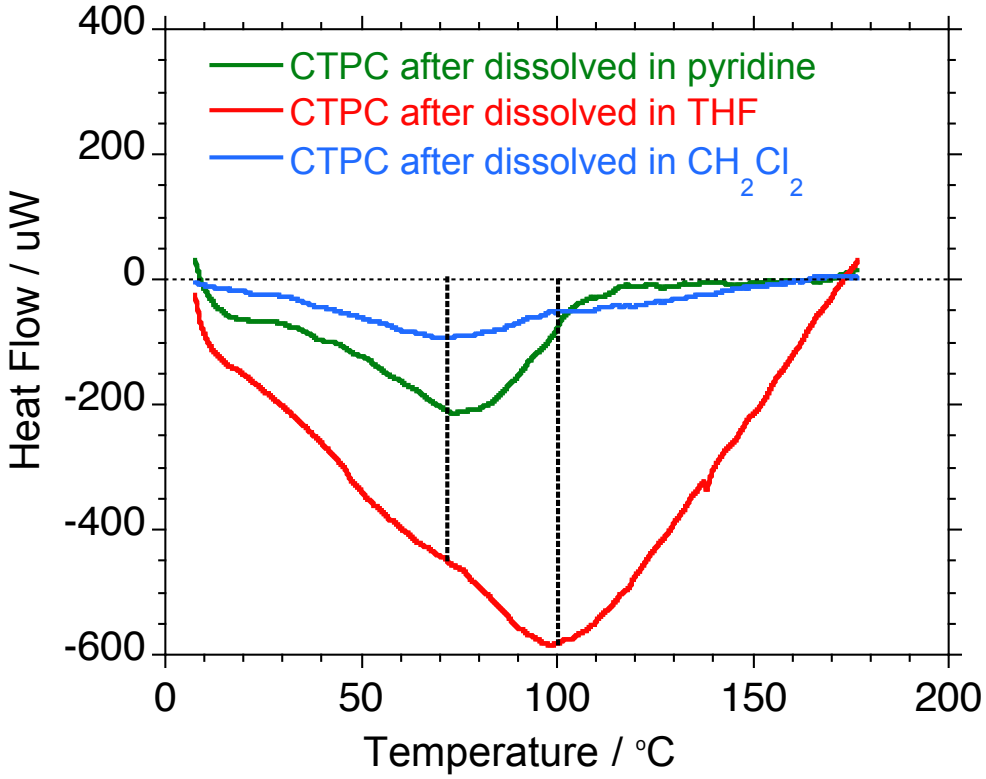


**Figure 5.18.** DSC profiles of the **CTPC** without treatment (green) after dissolved in THF (red) and $CH_2Cl_2$ (blue) solutions.

We conducted DSC analyses to characterize the NH-O=C interactions and calculate the enthalpy change: $\Delta H$ (= 9.85 kcal/mol, THF) > $\Delta H$ (= 2.86 kcal/mol, pyridine) > $\Delta H$ (= 1.88 kcal/mol, $CH_2Cl_2$) (Figure 5.18). The differences in the DSC data were based on the decomposition energy of the NH/O=C interactions. As we know, the $\Delta H$ of a C=O/H-N interaction is 3–7 kcal/mol. The cleavage of two urethane bonds derived from a secondary hydroxyl group (glucose-O-C=O/H-N-Ph) directly attached to the pyranose ring of CTPC was attributed to the DSC endothermic signal near 100°C. One urethane bond (glucose- $CH_2$-O-C-O/H-N-Ph) derived from a primary hydroxyl group directly linked via methylene was attributed to the DSC endothermic signal in the vicinity of 50-70°C. The NH-O=C interactions (on state) in the THF illustrated a stronger CD signal

and ordered structure in the side chains.[25]

The changes in the DSC data, once again, confirmed that the solvent induced the preferred direction of the **CTPC** structure and maintained the chiral structure in the side chains. In the THF, it was difficult to cleave the NH/O=C bonds in the side chains of **CTPC**, so the $\Delta H$ was large. The $\Delta H$ was small when the NH/O=C bonds in the side chains of **CTPC** with $CH_2Cl_2$ were easily cleaved.

5.2.4 Solubility for Side-Chain Dependence of CTPC

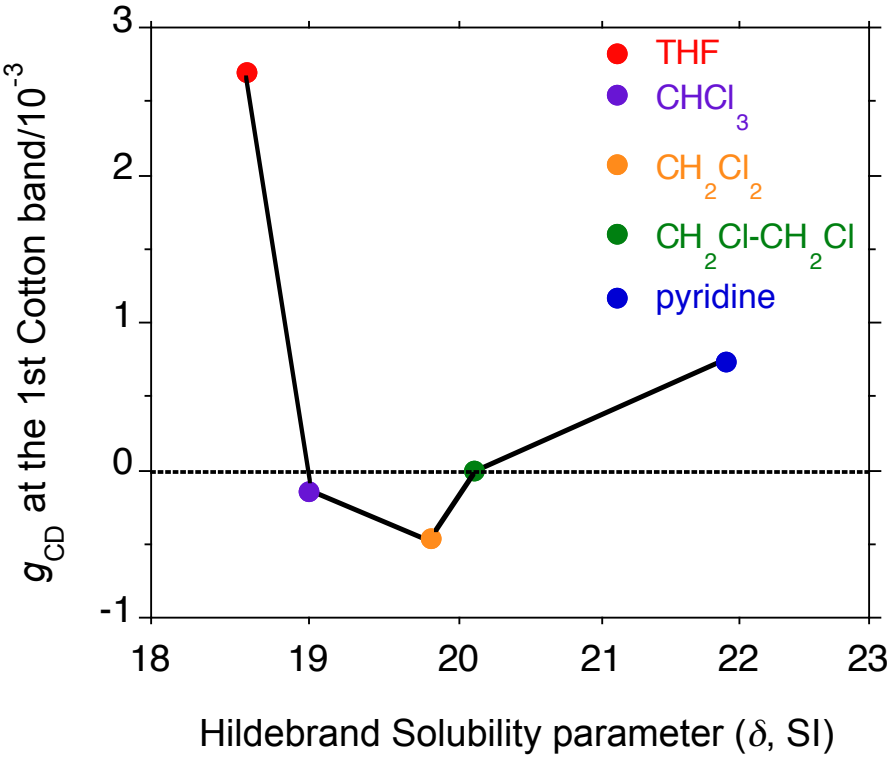


**Figure 5.19.** The $g_{CD}$ values at the first Cotton band of the CD spectra of the CTPC-PF6 film as a function of the relative permittivity after dissolved in THF (red), $CHCl_3$ (purple), $CH_2Cl_2$ (orange), $CH_2Cl_2$-$CH_2Cl_2$ (green) and pyridine (blue).

We measured the CD experiments using the solvent Hansen solubility parameter: THF (18.6), $CHCl_3$ (19.0), $CH_2Cl_2$ (19.8), $CH_2Cl$-$CH_2Cl_2$ (20.1), and pyridine (21.9). The (+) fluorene structure was transferred in THF and pyridine as solvents for **CTPC**. The (-) fluorene structure was transferred with $CHCl_3$, $CH_2Cl_2$, and $CH_2Cl$-$CH_2Cl$. We think that the difference between the solubility parameters of **CTPC** and its solvent is an important factor. A smaller difference between the solubility parameters indicates stronger the interactions between the solvent and **CTPC** due to hydrogen bonds. A larger difference indicates weaker interactions between the solvent and **CTPC**, making it easier for hydrogen bonding to promote the formation of helical structures in **CTPC**.[26]

5.2.5 Computer-Assisted Modeling of **CTPC** and Oligofluorene

In the previous sections, we showed the chirality transfer from **CTPC** to fluorenes, leading to retention and inversion in the CD and CPL signals. We focused on the transfer mechanism depending on the conformation changes of the side chains on **CTPC** and possible intermolecular interaction between the fluorenes and **CTPC**. MD simulations were carried out using a Materials Studio Forcite module with a universal force field (UFF).[8] **CTPC** contains three phenylcarbamate groups that contribute to the N-H/O=C hydrogen bonds. The hydrogen bonds should have led to certain chiral and helical structures.

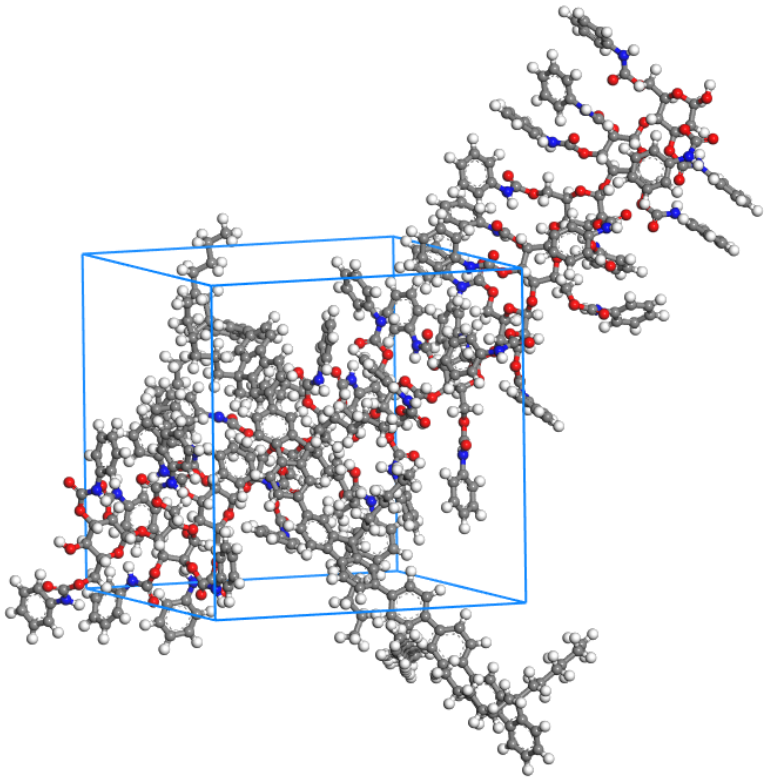

**Figure 5.20.** An optimized molecular model of **CTA** and **PF6** equilibrated at 300 K obtained with the Forcite module in Materials Studio.

In these simulations, we designed a hybridized system of **CTPC** with 12-units and **PF6** with 12-units in order to interpret the intermolecular interactions, followed by the

induction of helical and/or chiral motifs, as shown in Figure 5.20. The optimized **CTPC** with 12-units and **PF6** with 12-units were obtained by Forcite Geometry Optimization. The two structures were connected to form a polymer hybrid system.

After generating the initial polymer structure, the geometry was refined using a self-consistent iterative procedure at pressures of 0.01 GPa and 0.1 MPa until the calculations converged. To optimize the energy minimization, the polymer hybrid system was annealed at high temperatures using Forcite Anneal Dynamics; the model was finally equilibrated at 300 K and one atmosphere of pressure for 150 ps using the NPT method from classical MD.[9]

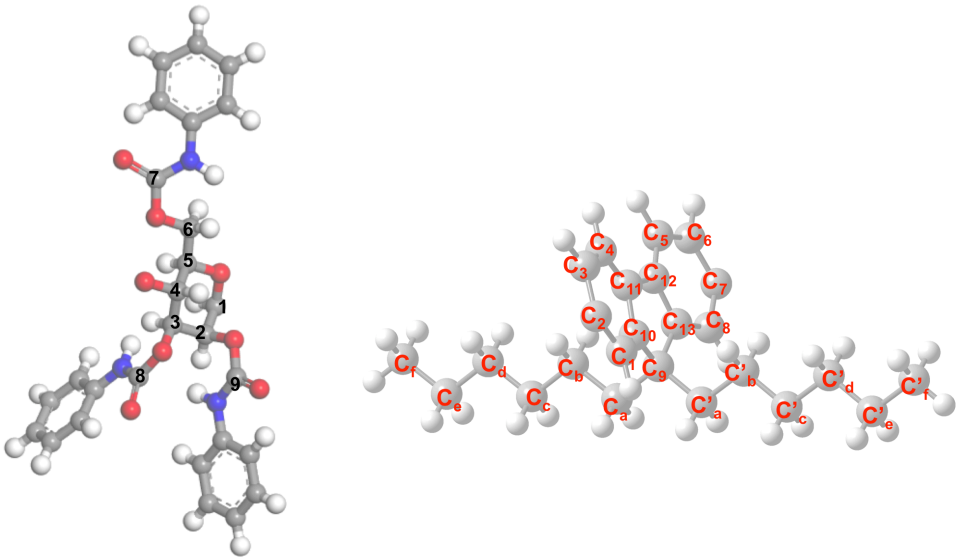


**Figure 5.21.** Model structures of **PF6** and **CTPC**.

We numbered the backbone and side-chain atoms in Figure 5.21. To consider the effects of the helicity and chirality transfer as well as the twists of polyfluorene, the **CTPC** backbone generally revealed three unique HN-C=O bonds in the acetyl groups in the backbone.

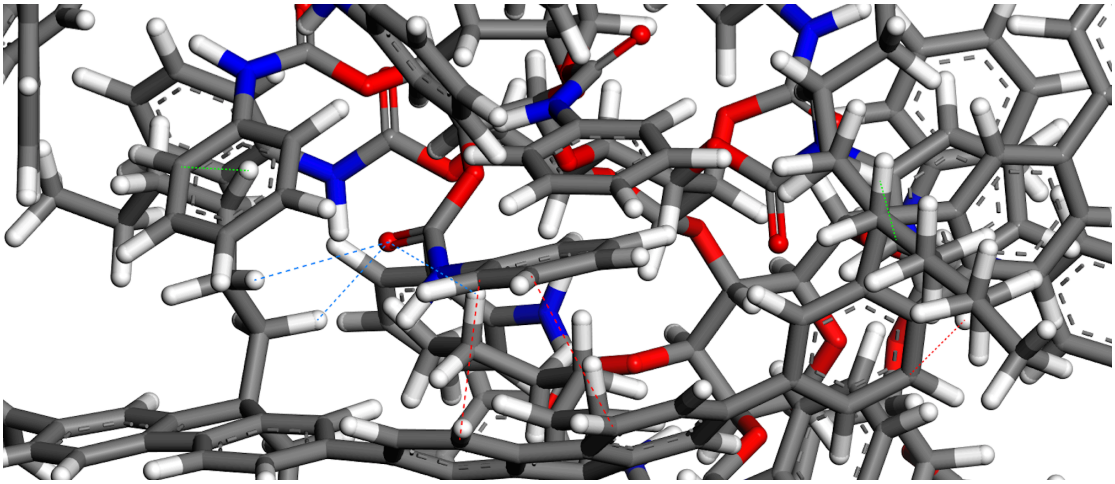

**Figure 5.22.** Simulated C-H/O=C interactions (dotted line), CH/π interactions (green dotted line), and π/π interactions (red dotted line) between **PF6** and **CTPC**.

The MD simulations indicated the existence of intermolecular C-H/O=C interactions, CH/π interactions, and π/π interactions between **CTPC** and **PF6 (**Figure 5.22**)**. The distances between H and O ranged from 2.77 to 2.99 Å. The distances between H and the *Phenyl* groups were greatly shortened compared to the van der Waals interaction distance of 3.0 Å,[10,27,28] and the distances between the *Phenyl* groups were shorter than 3.5 Å.[29] A huge number of interactions in the **CTPC** framework were thus responsible for transferring the helicity and/or chirality, followed by induction of the left–right imbalance, leading to optically active **PF6** as indicated by the CD and CPL signals (Table 5.5, 5.6, 5.7).

**Table 5.5.** The distances between selected C–*H* and *O*=C groups in the C–H/O=C interactions. Distance 1 is the distance from one proton of an n-octyl group to *O*=C, while distance 2 is the distance from another proton to *O*=C from the MD calculation.

| Group name | Distance 1 (Å) | Distance 2 (Å) |
|---|---|---|
| C9=O/H-$C_a$ | 2.77 | 4.40 |
| C9=O/H-$C_b$ | 2.74 | 4.46 |
| C9=O/H-$C_e$ | 2.99 | 3.47 |

**Table 5.6.** The distances between selected C–*H* and *Phenyl* groups in the CH/π interactions. Distance 1 is the distance from one proton of an n-octyl group to a *Phenyl* group, while distance 2 is the distance from another proton to a *Phenyl* group from the MD calculation.

| Group name | Distance 1 (Å) | Distance 2 (Å) |
|---|---|---|
| C8 *Phenyl* groups /H-$C_b$ | 2.90 | 3.60 |
| C9 *Phenyl* groups /H-$C_b$ | 2.74 | 4.46 |
| C8 *Phenyl* groups /H-$C_c$ | 3.00 | 4.70 |

**Table 5.7.** The distances between selected *Phenyl* groups for π/π interactions from the MD calculation.

| Group name | Distance 1 (Å) |
|---|---|
| C8 *Phenyl* groups /$C_4$ *Phenyl* groups | 3.39 |
| C8 *Phenyl* groups /$C_5$ *Phenyl* groups | 3.19 |
| C9 *Phenyl* groups /$C_5$ *Phenyl* groups | 2.93 |

## 5.3 Reference


(1) Onofrei, M. D.; Dobos, A. M.; Ioan, S. In *Polymer Nanocomposites: Fundamentals and Applications*, Thakur, V. K. Ed., Wiley: Weinheim, Germany, Chapter 14, Nanocellulose Polymer Nanocomposites, pp 355–391.

(2) Dubois, J. C.; Barny, P. L.; Mauzac, M.; Noel, C. In. *Handbook of Liquid Crystals, Fundamentals High Regular weigt Liquid Crystal*, Demus, D., Goodby, J. W., Gray, G. W., Spiess, H. S., Vill, V., Eds.; Wiley-VCH Press: New York, **1998**; Vol 3, Chapter 2, pp 207–269.

(3) Eliel, E. L.; Wilen, S. H.; Mander, L. N. In *Stereochemistry of Organic Compounds*, Wiley-Interscience: New York, NY, **1994**. Chapter 13, pp 991–1118.

(4) Ghosh, A.; Fischer, P. *Phys. Rev. Lett.*, **2006**, *97*, 173002–173004.

(5) Kuse, Y.; Asahina, D.; Nishio, Y. *Biomacromolecules* **2009**, *10*, 166–173.

(6) Nazeeruddin, M. K. De Angelis, F. Fantacci, S. Selloni, A. Viscardi, G. Liska, P. Ito, S. Takeru, B. Grätzel, M. *J. Am. Chem. Soc.* **2005**, *127,* 16835–16847.

(7) Bader, R. F. W. *J. Phys. Chem. A* **1998**, *102*, 7314–7323.

(8) Margelefsky, E. L.; Zeidan, R. K.; Davis, M. E. *Chem. Soc. Rev.* **2008**, *37*, 1118–1126.

(9) Kim, K. C.; Moschetta, E. G.; Jones, C. W.; Jang, S. S. *J. Am. Chem. Soc.* **2016**, *138*, 7664–7672.

(10) Steiner, T.; Desiraju, G. R. *Chem. Commun.* **1998**, 891–892.

(11) Takahashi, O.; Kohno, Y.; Nishio, M. *Chem. Rev.* **2010**, *110*, 6049–6076.

(12) Yamamoto, H.; Horn, F. *Cellulose* **1994**, *1*, 57–66.

(13) VanderHart, D. L.; Hyatt, J. A.; Atalla, R. H.; Tirumalai, V. C. *Macromolecules* **1996**, *29*, 730–739.

(14) Kono, H.; Erata, T.; Takai, M. *J. Am. Chem. Soc.* **2002**, *124*, 7512–7518.

(15) Knaapila, M.; Winokur, M. J. *Adv. Polym. Sci.* **2008**, *212*, 227−272.

(16) Yates, J. R.; Pham, T. N.; Pickard, C. J.; Mauri, F.; Amado, A. M.; Gil, A. M.; Brown, S. P. *J. Am. Chem. Soc.* **2005**, *127*, 10216–10220.

(17) Sozzani, P.; Comotti, A.; Bracco, A.; Simonutti, R. *Chem. Commun*. **2004**, 768–769.

(18) Vinogradov, E.; Madhu, P. K.; Vega, S. *Chem. Phys. Lett*. **1999**, *314*, 443–450.

(19) Freeman, R.; Hill, V.; Kaptein, R. *J. Magn. Reson.* **1972**, *7*, 327–329.

(20) Bertini, I.; Emsley, L.; Lelli, M.; Luchinat, C.; Mao, J.; Pintacuda, G. *J. Am. Chem. Soc.* **2010**, *132*, 5558–5559.

(21) Brus, J.; Jegorov, A. *J. Phys. Chem.* A, **2004**, *108,* 3955–3964.

(22) Socrates, G. Infrared and Raman characteristic group frequencies: table and charts. Ltd WJS, **2001**, pp1–347.

(23) Tsui, H. W.; Wang, N. H. L.; Franses, E. I. *J. Phys. Chem. B*, **2013**, *117*, 9203–9216.
(24) Mirzaei, M.; Hadipour, N. L.; Ahmadi, K. *BIOPHYS. CHEM.* **2007**, *125*, 411–415.
(25) Takahashi, O.; Kohno, Y.; Nishio, M. *Chem. Rev*. **2010**, *110*, 6049–6076.
(26) J. Brandrup, E. H. Immergut, and E. A. Grulke, *Polymer Handbook*, 4, VII/707, Wiley (1999).
(27) Tsuzuki, S.; Honda, K.; Uchimaru, T.; Mikami, M.; Tanabe, K. *J. Am. Chem. Soc.* **2000**, *122*, 11450–11458
(28) Zhao, C.; Parrish, R. M.; Smith, M. D.; Pellechia, P. J.; Sherrill, C. D.; Shimizu, K. D. *J. Am. Chem. Soc.* **2012**, *134*, 14306–14309
(29) Hunter, C. A.; Sanders, J. K. *J. Am. Chem. Soc.* **1990**, *112*, 5525–5534

## Chapter 6. Concluding Remarks

Knowing and understanding the chiral/helical interactions existing between non-charged molecules and polymers and between non-charged polymers and polymers remains unclear due to non-restricted intra and intermolecular rotational freedom. Herein, we highlighted the CPL and bisignate CD signals of 9,9-dialkylfluorene oligomers and polymers, known as achiral chromophoric luminophores, as a function of the repeating ring number. The CPL and CD signals were induced by cellulose triacetate (**CTA**), cellulose acetate butyrate (**CABu**) and cellulose triphenylcarbamate (**CTPC**) as non-chromophoric helical/chiral polymers. This dissertation contains three sections:

The first section revealed experimental evidence of the **CTA**/**CABu** transfer system. When $n$ = 3–7, **CTA** and **CABu** induced the same (+) CD sign due to the D-glucose chirality. However, when $n \geq 47$, they induced the opposite CD signs. On the other hand, when $n \geq 3$, **CTA** and **CABu** induced the opposite CPL signs. However, when $n$ = 2–7, **CABu** induced opposite CD and CPL signs, and when $n \geq 3$, **CTA** induced the same CD and CPL sign.

In the second section, we observed clear helical inversion that was dependent on solvent effects in **the CTPC** system with preferences for P- or M-helixes with twisted units due to chirality transfer. Changing the helical structure of the amide groups induced a chirality switch of the branch chains in **CTPC.** This effect was confirmed by the CD and CPL spectra of the fluorenes embedded in the hybridized film.

In the final section, the mechanisms of chirality transfer were discussed. **CTA** and **CABu** had a common D-glucose framework of β(1→4) linkages, but prefer right- and left-handed helicity, respectively. A conflict between the D-glucose local chirality and main chain helicity was responsible for the *n*-dependent CD and CPL signs. The first

clear detection of an intense cross peak in the solid-state $^{1}H$-$^{13}C$ HETCOR NMR spectrum indicated the existence of intermolecular C–H/O=C interactions between H-C due to the *n*-octyl methylene of fluorene with $n$ = 201 and C=O due to acetyl groups attached to the chiral D-glucose of **CTA**. This idea was consistent with the results from the MM/MD simulations.

Also in this last section, the induced chirality transfer from the **CTPC** branches was found. Although **CTPC** adopted left-handed helical conformations in the solid state, the helix preference of **PF6** was tailored by the choice of the solvent. The solvent polarity was crucial to the switch on-off ability of hydrogen bonding between N-H and O=C-O due to the carbamoyl groups of **CTPC,** as confirmed by the IR and WAXD analyses and MM/MD simulations.

## Appendix

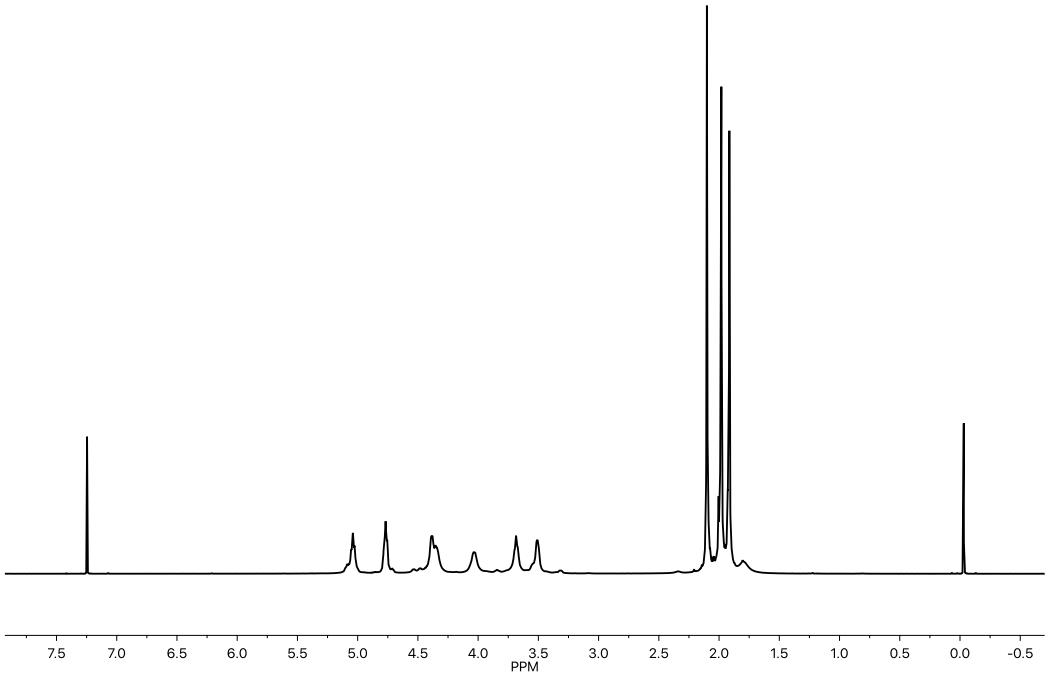


**Figure A1.** $^{1}$H NMR spectrum of CTA in $CDCl_3$ at 25°C. Elemental analysis: Obsd *C* 46.80 and *H* 5.36 (%). Calcd for $[(C_{12}H_{16}O_8 \bullet H_2O)_n]$ C 47.06 and H 5.92 (%)**.**

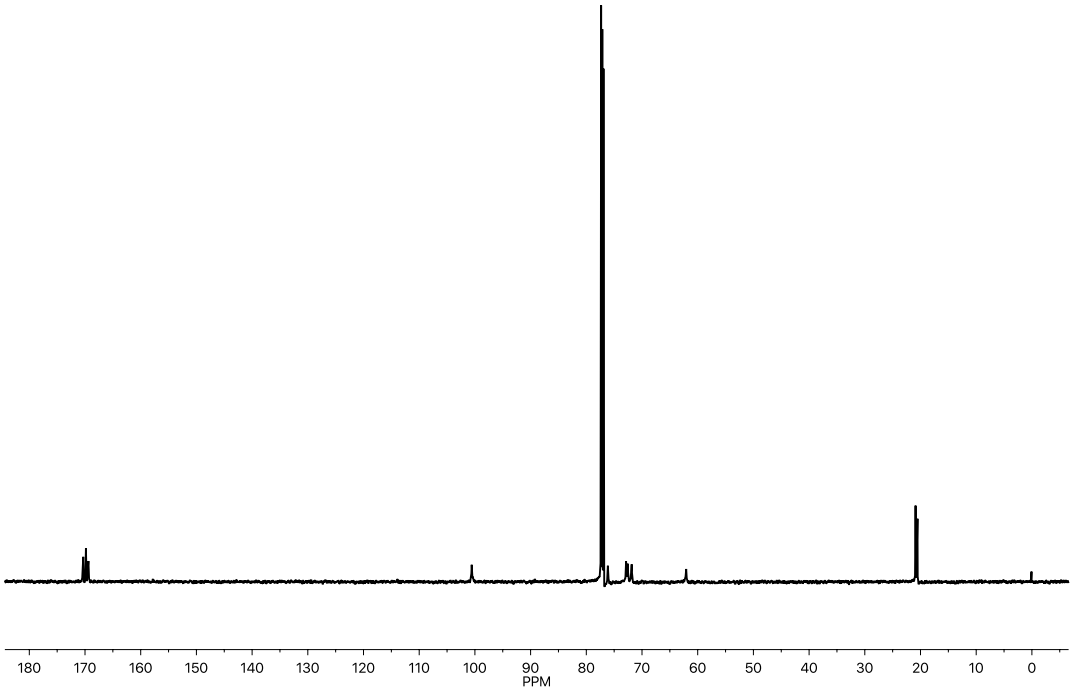


**Figure A2.** $^{13}$C NMR spectrum of **CTA** in $CDCl_3$ at 25°C.

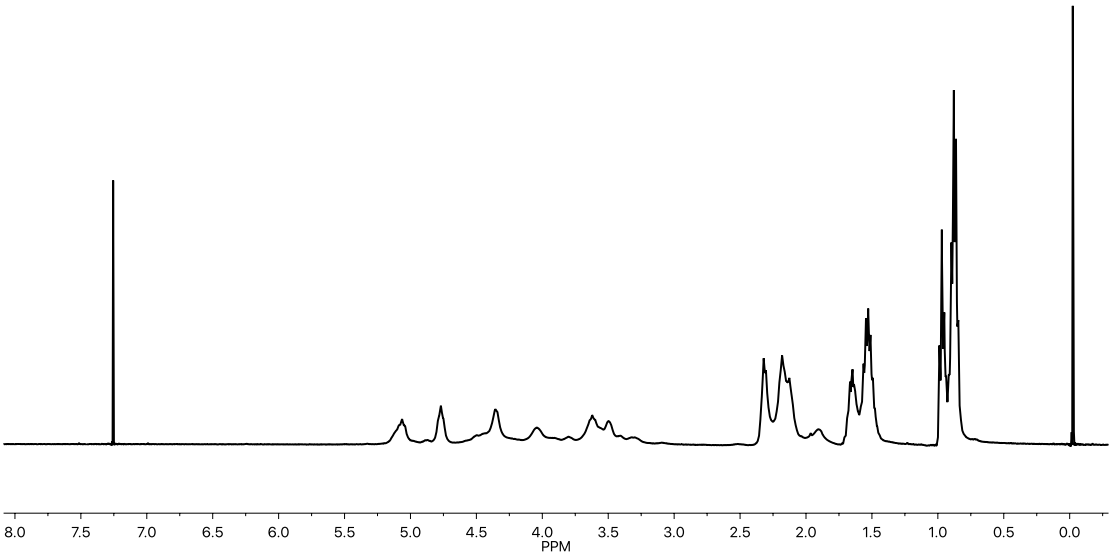


**Figure A3.** $^{1}$H NMR spectrum of **CABu** in $CDCl_3$ at 25°C. Elemental analysis: Obsd *C* 56.87 and *H* 7.43 (%).

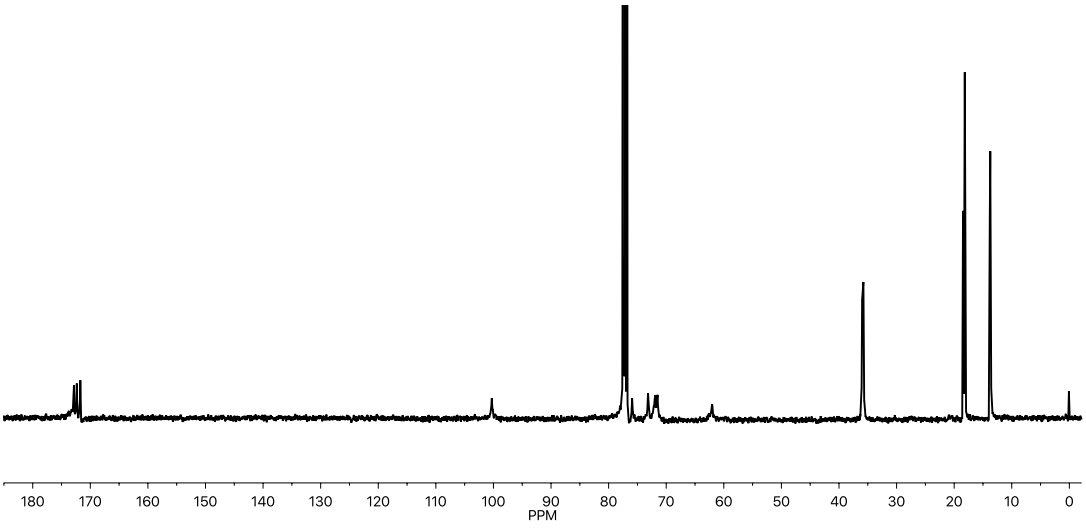


**Figure A4.** $^{13}$C NMR spectrum of **CABu** in $CDCl_3$ at 25°C.

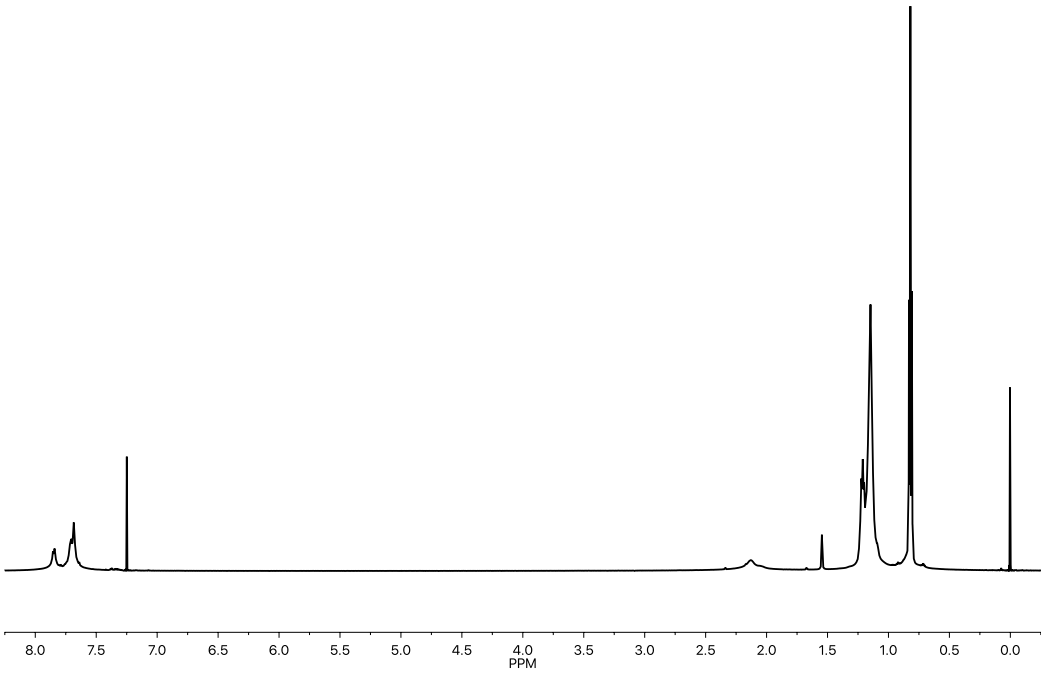


**Figure A5.** $^{1}$H NMR spectrum of **PF8** in $CDCl_3$ at 25°C. Elemental analysis: Obsd *C* 89.63 and *H* 10.34 (%). Calcd for $(C_{29}H_{40})_n$ *C* 89.63, *H* 10.37 (%).

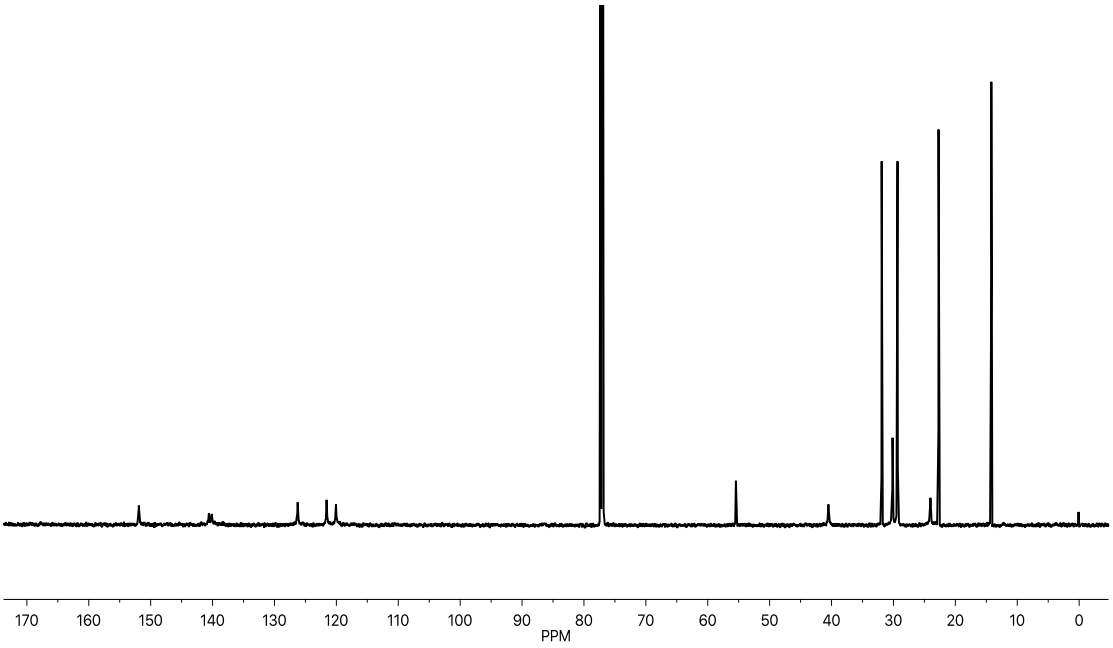


**Figure A6.** $^{13}$C NMR spectrum of **PF8** in $CDCl_3$ at 25°C.

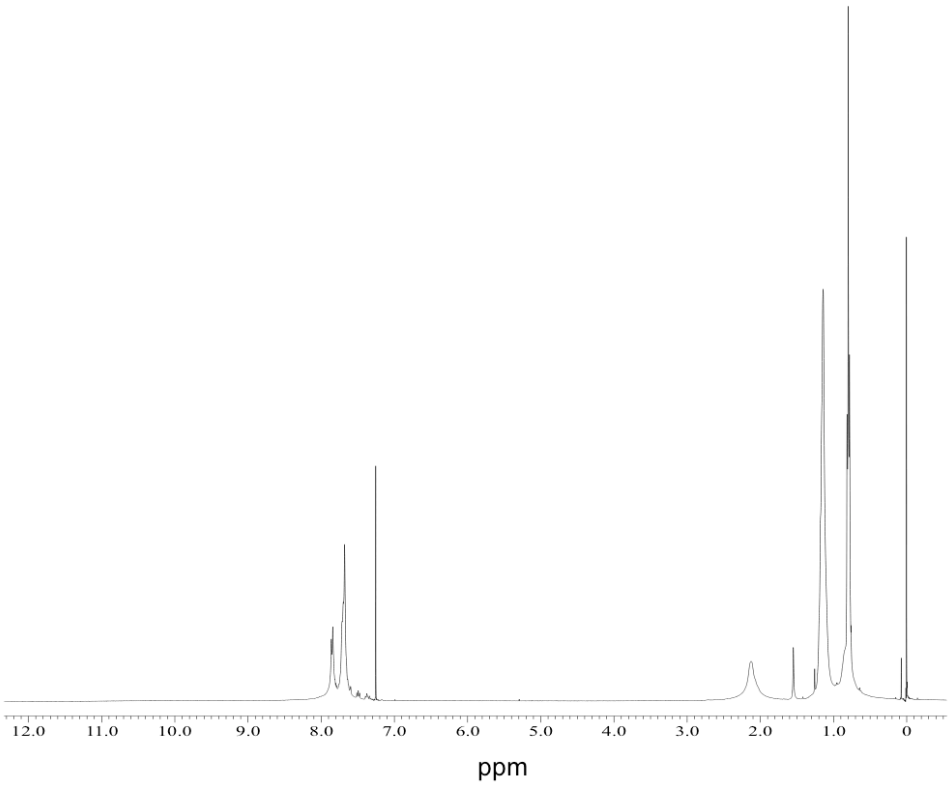


**Figure A7.** $^{1}H$ NMR spectrum of **PF6** in $CDCl_3$ at 25°C.

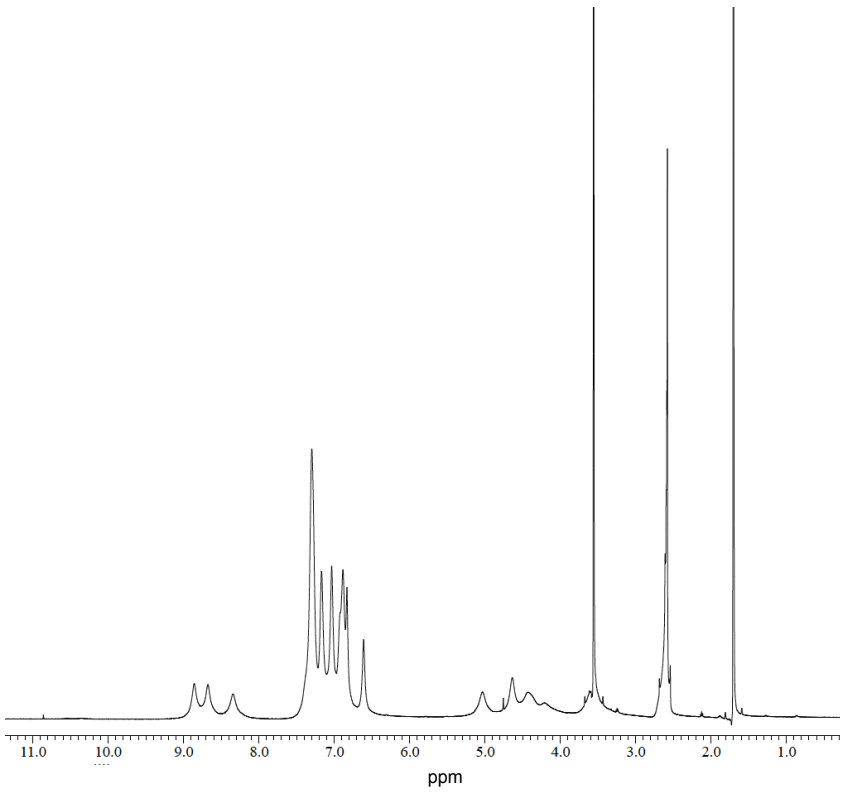


**Figure A8.** $^{1}H$ NMR spectrum of **CTPC** in THF-$d_8$ at 25°C.

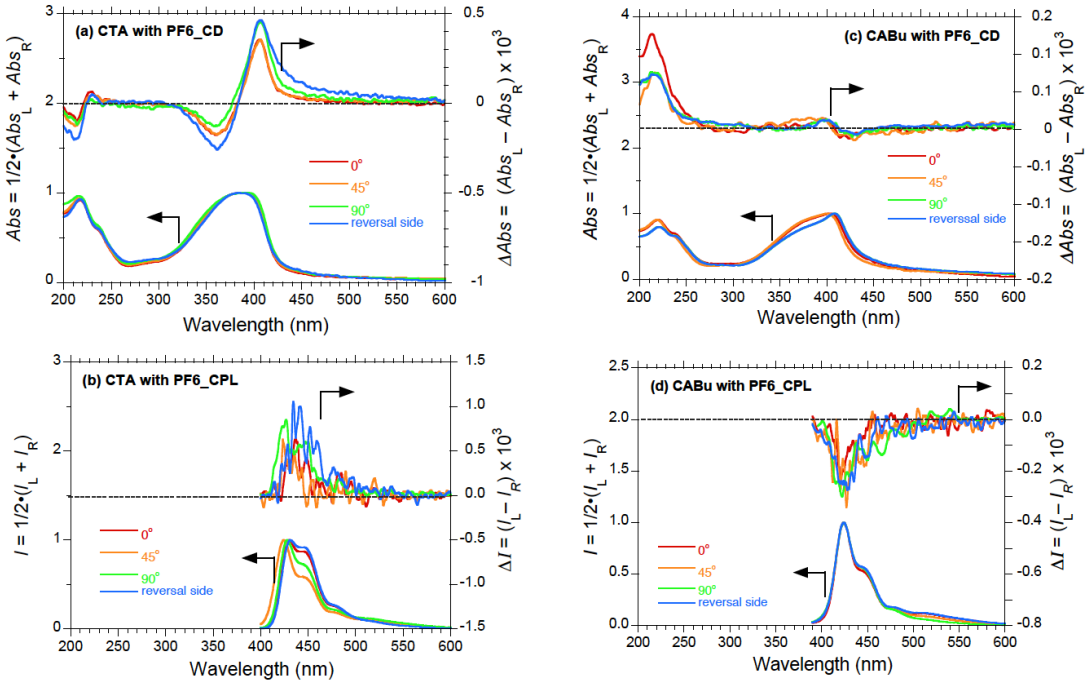


**Figure A9.** Verification of the rotation-angle-dependent CD and CPL (0°, 45°, and 90° and its reversal side at one specific angle) of the hybridized **CTA** and **CABu** films with **PF6** deposited on a round-shaped quartz plate using a spin-coating technique. The spectra indicated that the resulting films with our methodology were in amorphous states without anisotropic orientation, leading to no artifacts in the CD and CPL spectra. Other **CTA** and **CABu** films with oligofluorenes and **PF8** were confirmed this result during all CD and CPL measurements.

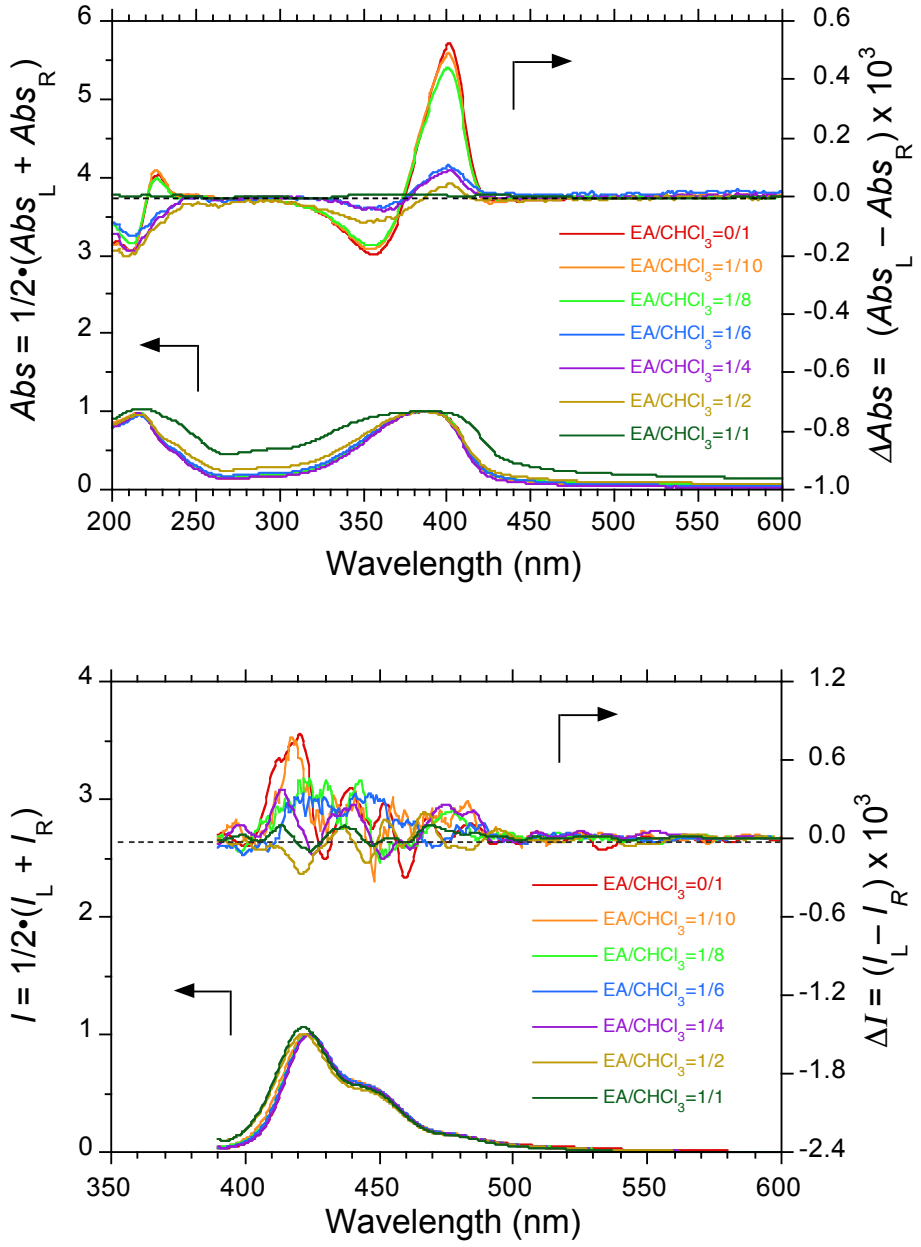


**Figure A10. Figure 3.4.** Normalized CD/UV-vis and CPL/PL spectra of the **CTA** thin films including **PF6** at 293 K on a quartz substrate.

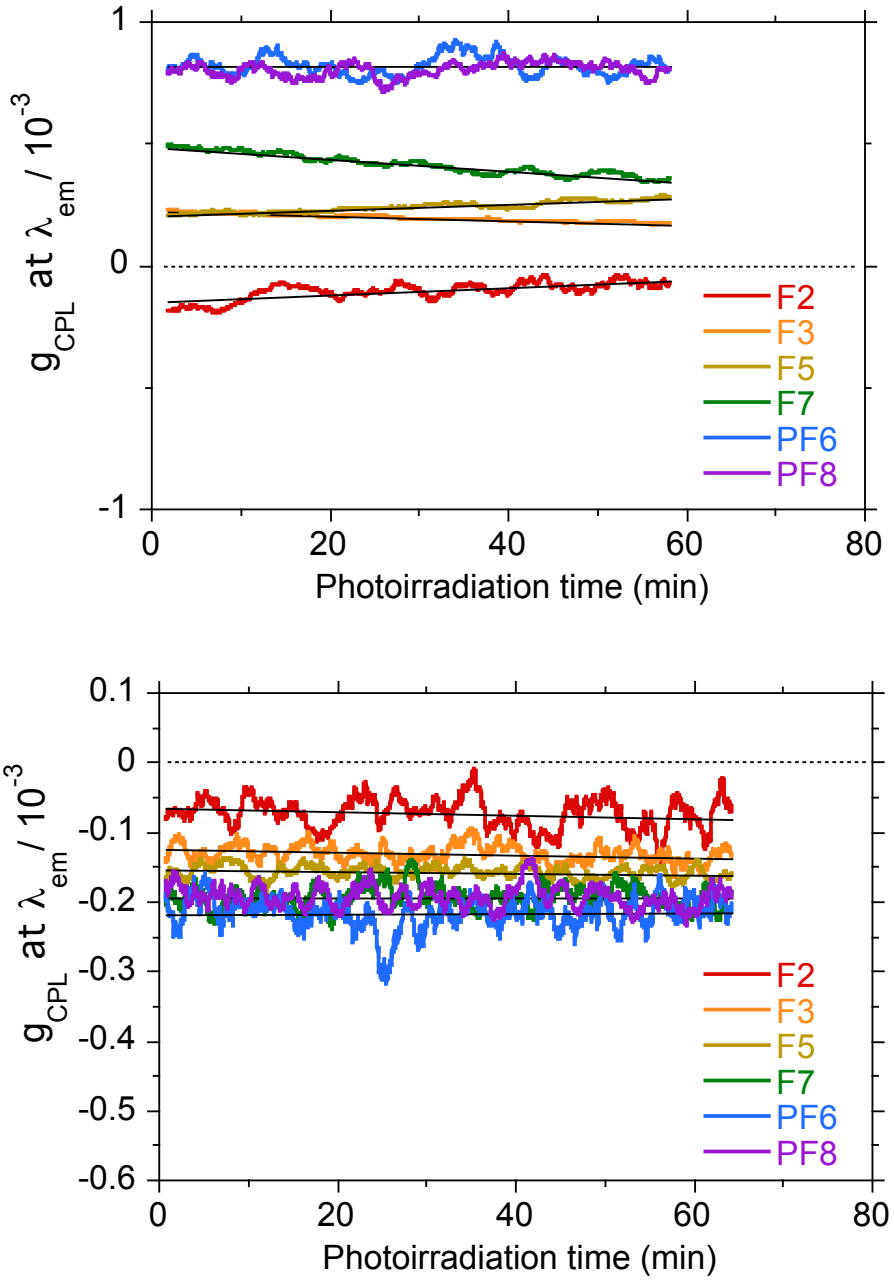


**Figure A11.** The change in the $g_{CPL}$ values of **F2**, **F3, F5**, **F7, PF6** and **PF8** in **CTA** (top) and **CABu** (bottom) films at 293 K on a quartz substrate upon unpolarized light irradiation at the $Max_{CPL}$ wavelength. The raw data were obtained with a built-in program of a JASCO CPL-200 spectrofluoropolarimeter and plotted as $g_{CPL}$ = ellipticity (mdeg) /14320/ PL (DC in volts).

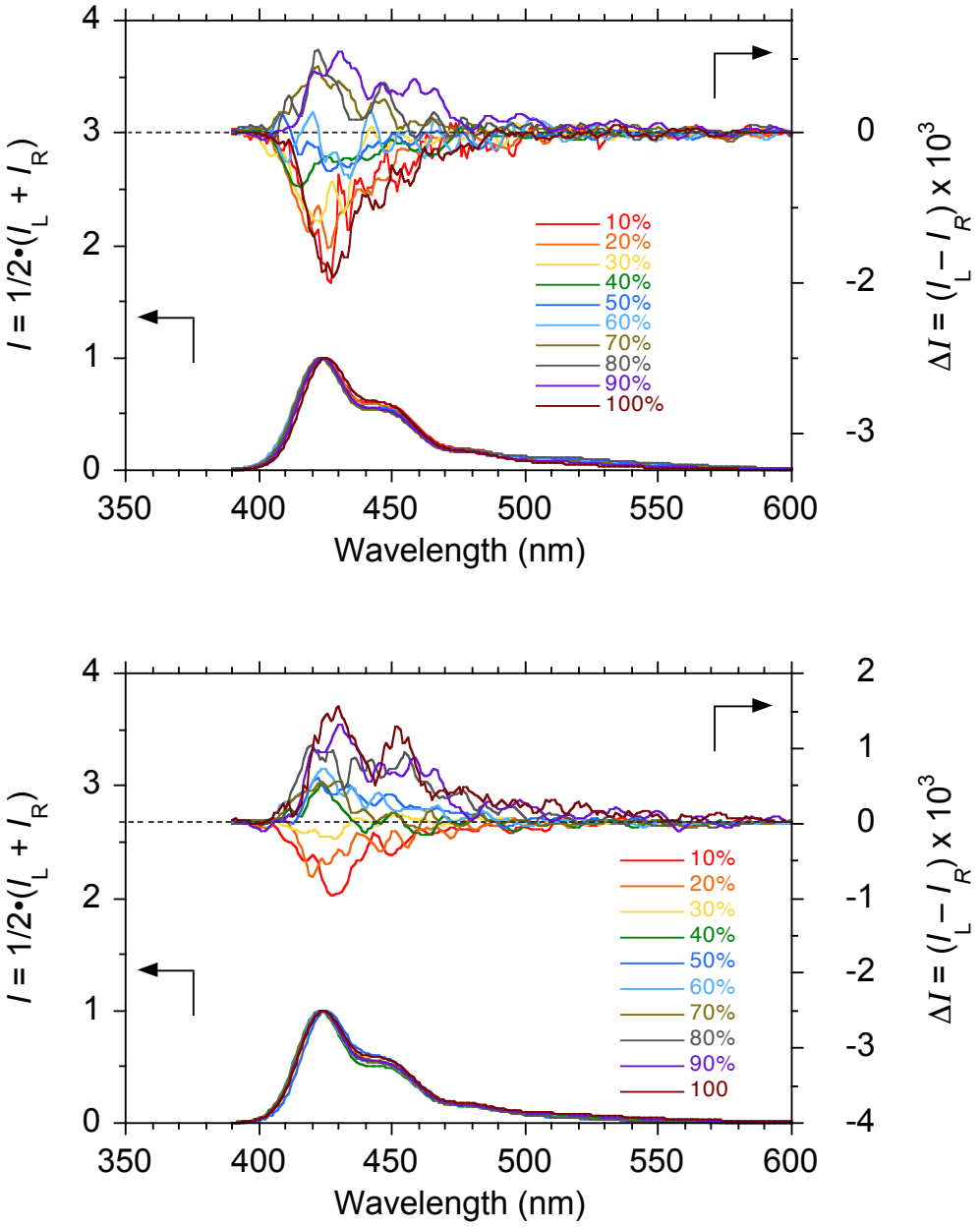


**Figure A12.** Normalized CPL/PL spectra of the **CTPC** thin films including PF6 as a function of the THF volume fraction. Excitation occurred at 355 nm. The original CH2Cl2 solution (top) and original THF solution (bottom) are shown.

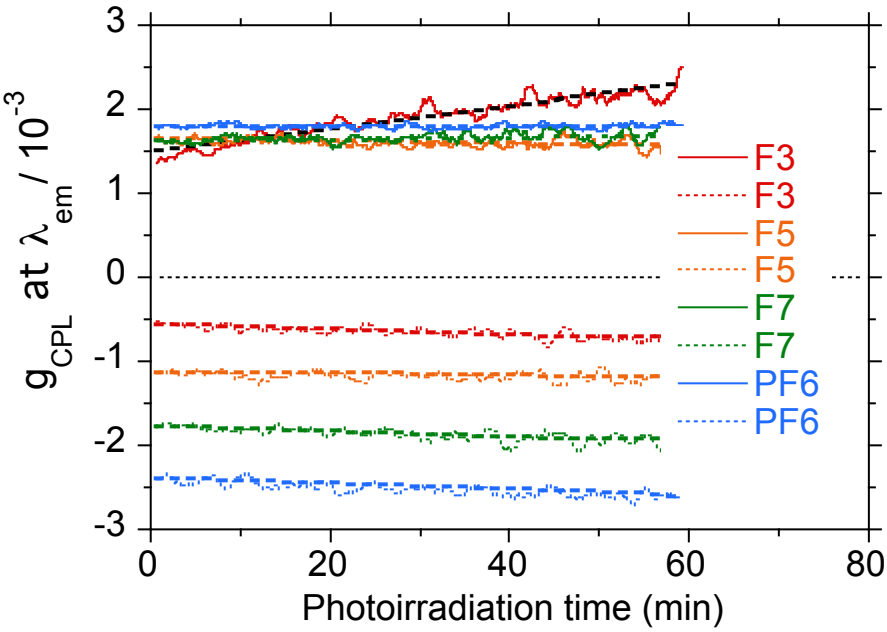


solid red lines after dissolved in THF,

dotted blue lines after dissolved in $CH_2Cl_2$

**Figure A13.** The changes of the $g_{CPL}$ values of **F3** (red), **F5** (orange), **F7** (green), and **PF6** (blue) in **the CTPC** films at 293 K on a quartz substrate upon unpolarized light irradiation at the CPL lext wavelength. The raw data were obtained with a built-in program of a JASCO CPL-200 spectrofluoropolarimeter and plotted with $g_{CPL}$ = ellipticity (mdeg) /14320/ PL (DC in Volt).

| | Angle 1 | Angle 2 | | Angle 1 | Angle 2 |
|---|---|---|---|---|---|
| ID1 | 0° | 0° | ID51 | −100° | 0° |
| ID2 | 0° | 20° | ID52 | −100° | 20° |
| ID3 | 0° | 40° | ID53 | −100° | 40° |
| ID4 | 0° | 60° | ID54 | −100° | 60° |
| ID5 | 0° | 80° | ID55 | −100° | 80° |
| ID6 | 0° | 100° | ID56 | −100° | 100° |
| ID7 | 0° | 120° | ID57 | −100° | 120° |
| ID8 | 0° | 140° | ID58 | −100° | 140° |
| ID9 | 0° | 160° | ID59 | −100° | 160° |
| ID10 | 0° | 180° | ID60 | −100° | 180° |
| ID11 | −180° | 0° | ID61 | −80° | 0° |
| ID12 | −180° | 20° | ID62 | −80° | 20° |
| ID13 | −180° | 40° | ID63 | −80° | 40° |
| ID14 | −180° | 60° | ID64 | −80° | 60° |
| ID15 | −180° | 80° | ID65 | −80° | 80° |
| ID16 | −180° | 100° | ID66 | −80° | 100° |
| ID17 | −180° | 120° | ID67 | −80° | 120° |
| ID18 | −180° | 140° | ID68 | −80° | 140° |
| ID19 | −180° | 160° | ID69 | −80° | 160° |
| ID20 | −180° | 180° | ID70 | −80° | 180° |
| ID21 | −160° | 0° | ID71 | −60° | 0° |
| ID22 | −160° | 20° | ID72 | −60° | 20° |
| ID23 | −160° | 40° | ID73 | −60° | 40° |
| ID24 | −160° | 60° | ID74 | −60° | 60° |
| ID25 | −160° | 80° | ID75 | −60° | 80° |
| ID26 | −160° | 100° | ID76 | −60° | 100° |
| ID27 | −160° | 120° | ID77 | −60° | 120° |
| ID28 | −160° | 140° | ID78 | −60° | 140° |
| ID29 | −160° | 160° | ID79 | −60° | 160° |
| ID30 | −160° | 180° | ID80 | −60° | 180° |
| ID31 | −140° | 0° | ID81 | −40° | 0° |
| ID32 | −140° | 20° | ID82 | −40° | 20° |
| ID33 | −140° | 40° | ID83 | −40° | 40° |
| ID34 | −140° | 60° | ID84 | −40° | 60° |
| ID35 | −140° | 80° | ID85 | −40° | 80° |
| ID36 | −140° | 100° | ID86 | −40° | 100° |
| ID37 | −140° | 120° | ID87 | −40° | 120° |
| ID38 | −140° | 140° | ID88 | −40° | 140° |
| ID39 | −140° | 160° | ID89 | −40° | 160° |
| ID40 | −140° | 180° | ID90 | −40° | 180° |
| ID41 | −120° | 0° | ID91 | −20° | 0° |
| ID42 | −120° | 20° | ID92 | −20° | 20° |
| ID43 | −120° | 40° | ID93 | −20° | 40° |
| ID44 | −120° | 60° | ID94 | −20° | 60° |
| ID45 | −120° | 80° | ID95 | −20° | 80° |
| ID46 | −120° | 100° | ID96 | −20° | 100° |
| ID47 | −120° | 120° | ID97 | −20° | 120° |
| ID48 | −120° | 140° | ID98 | −20° | 140° |
| ID49 | −120° | 160° | ID99 | −20° | 160° |
| ID50 | −120° | 180° | ID100 | −20° | 180° |

**Table A1.** The dihedral angles of the trimer model

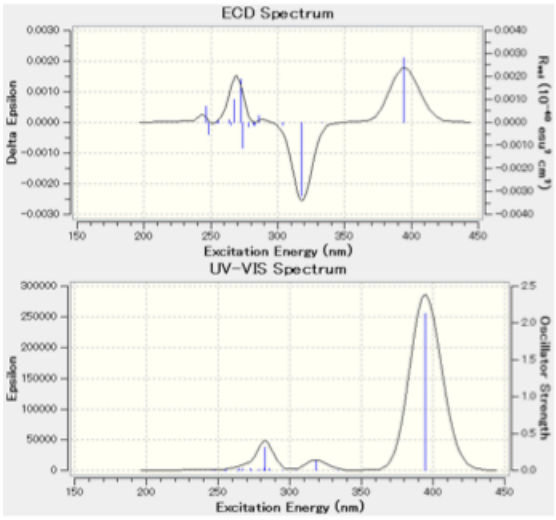


ID01

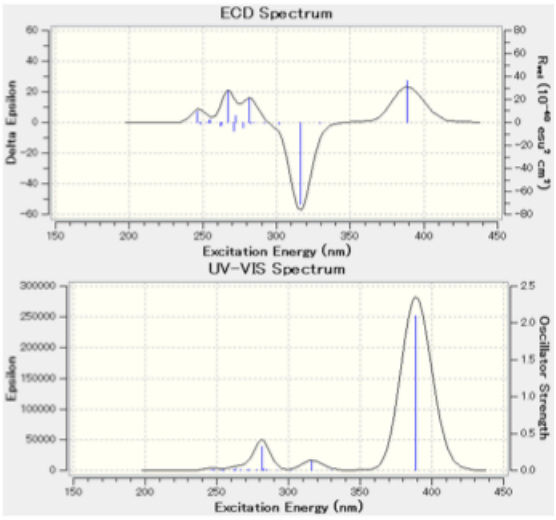


ID02

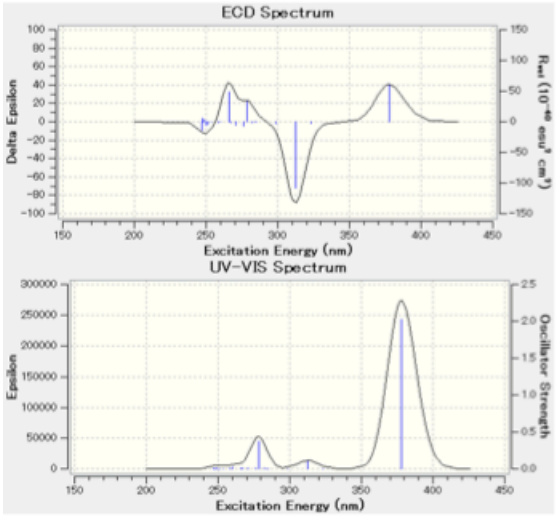


ID03

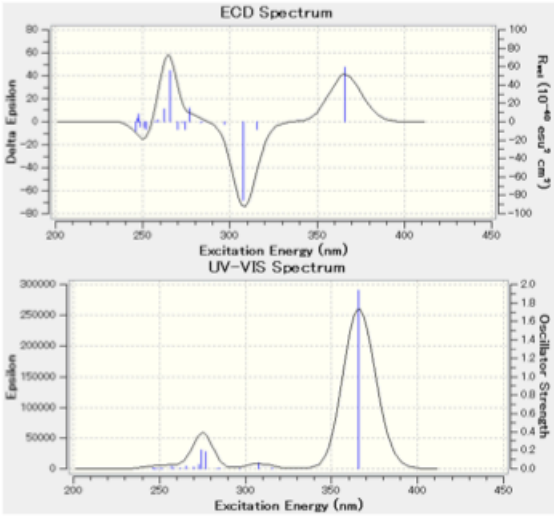


ID04

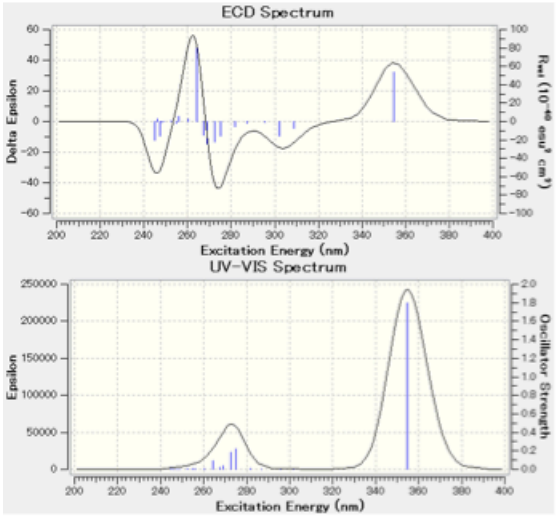


ID05

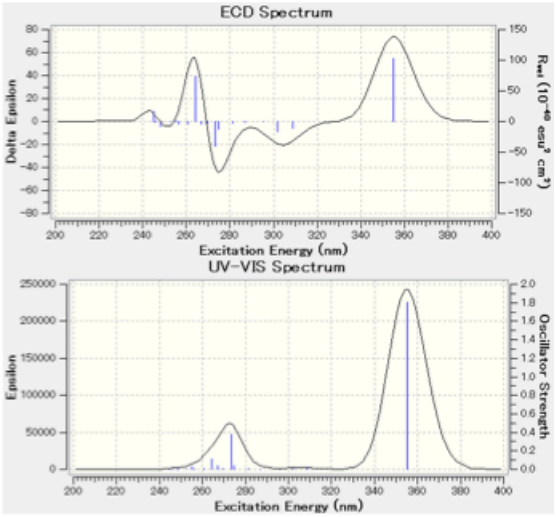


ID06

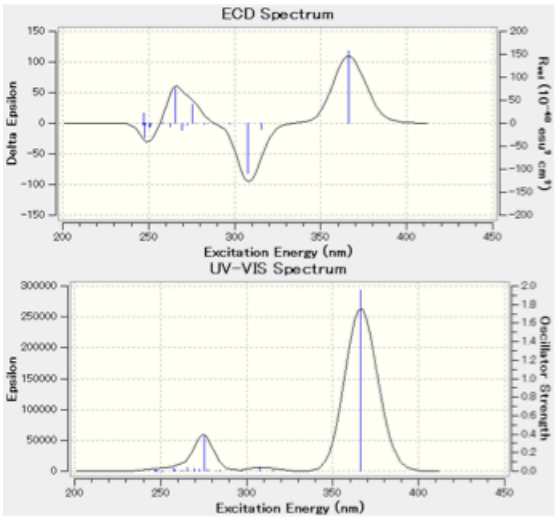


ID07

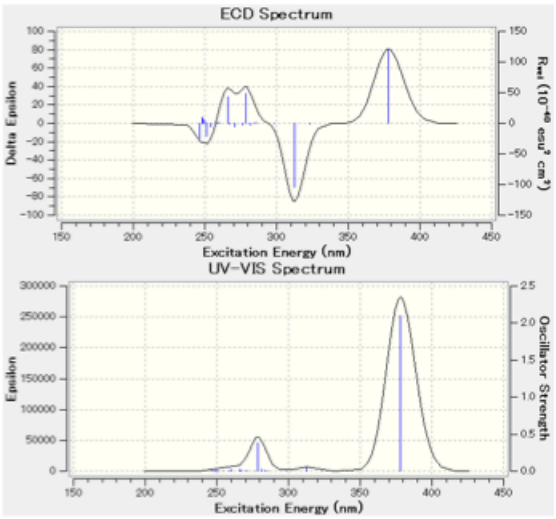


ID08

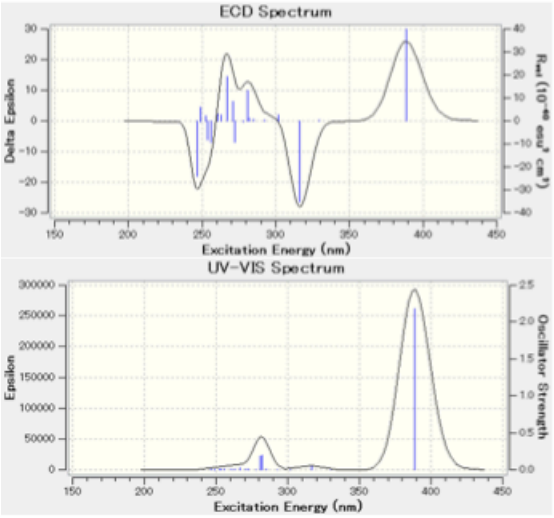


ID09

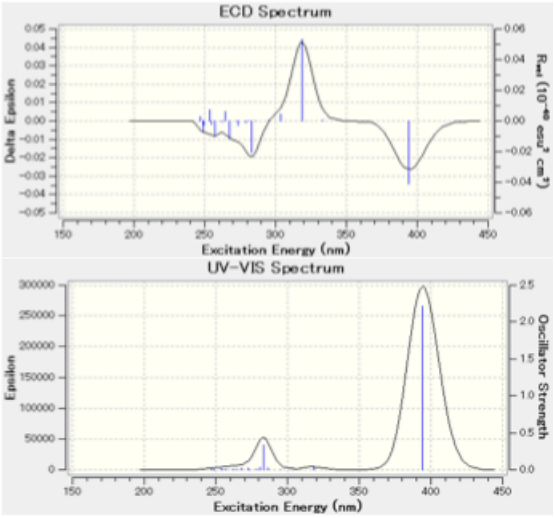


ID10

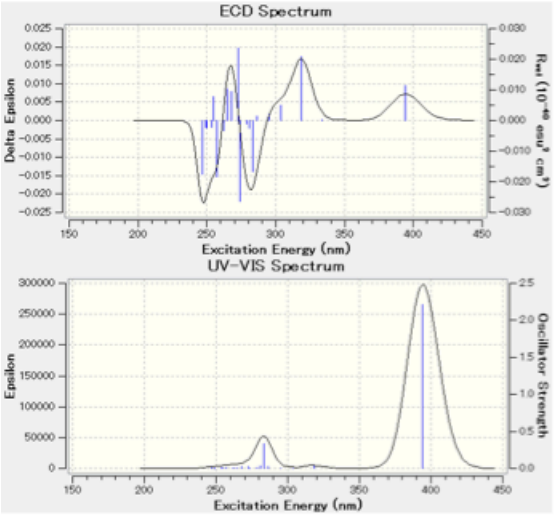


ID11

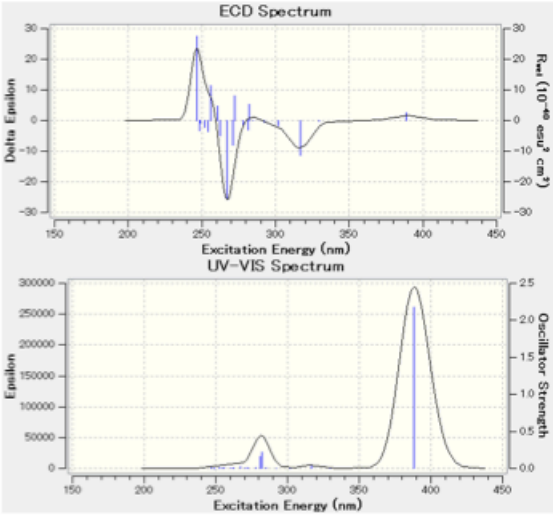


ID12

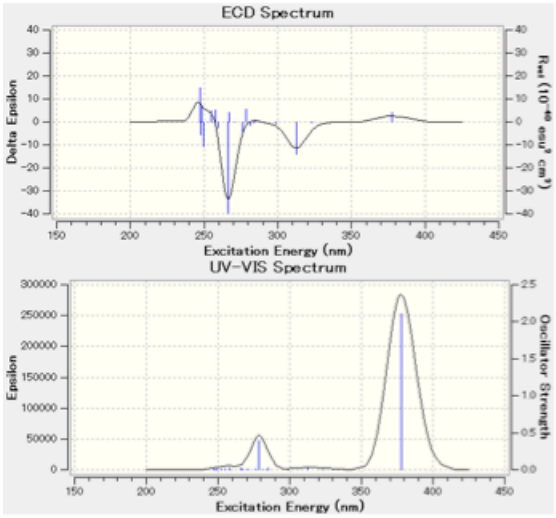


ID13

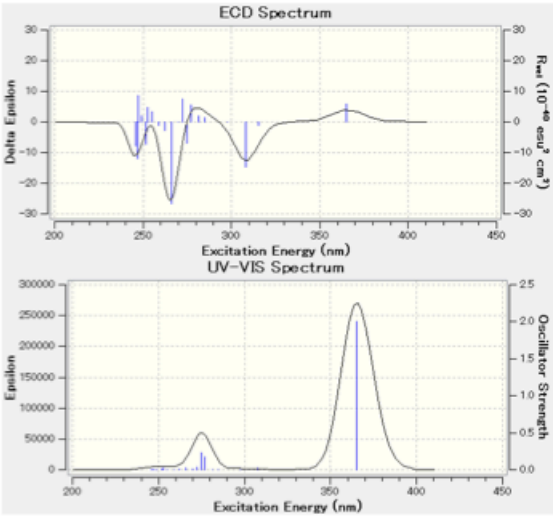


ID14

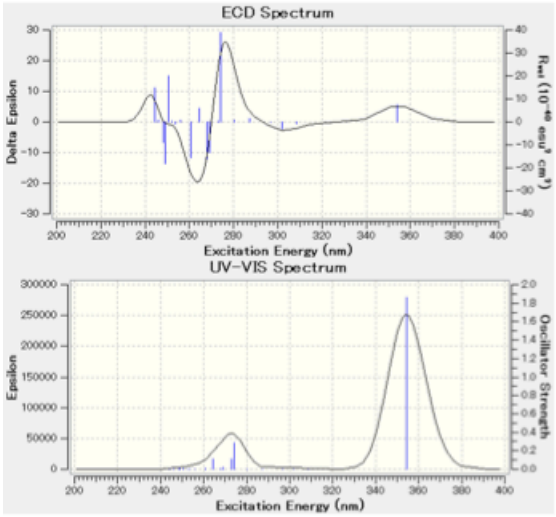


ID15

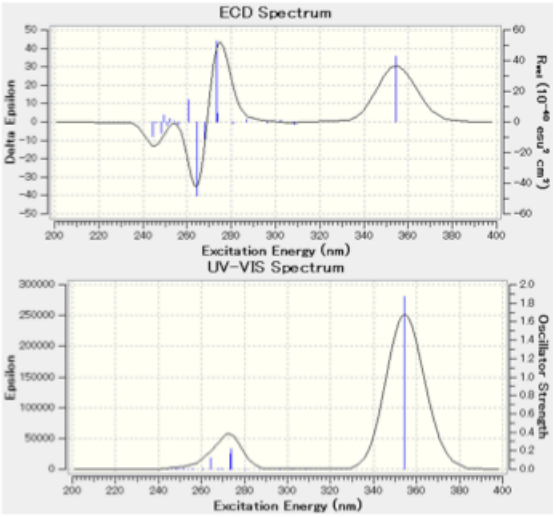


ID16

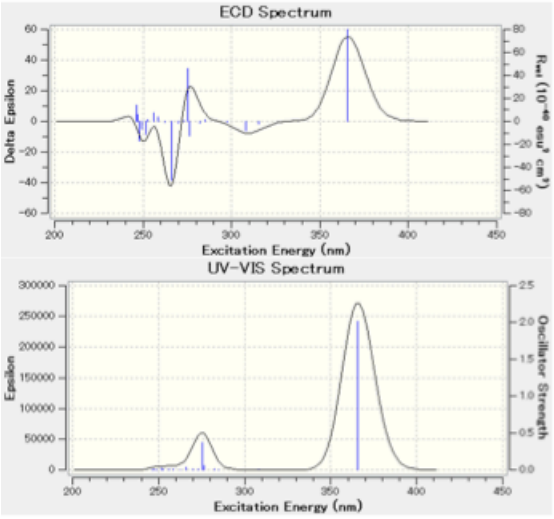


ID17

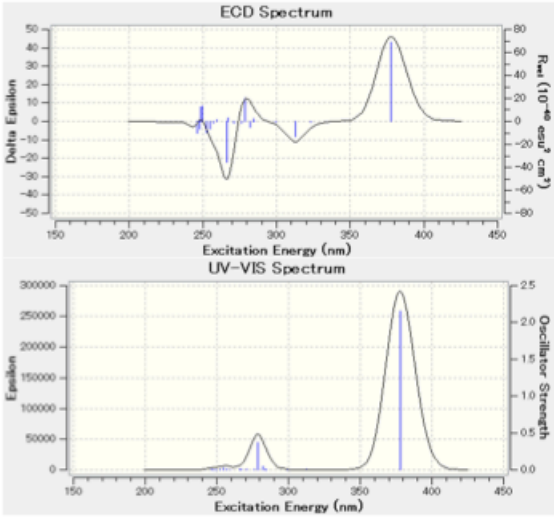


ID18

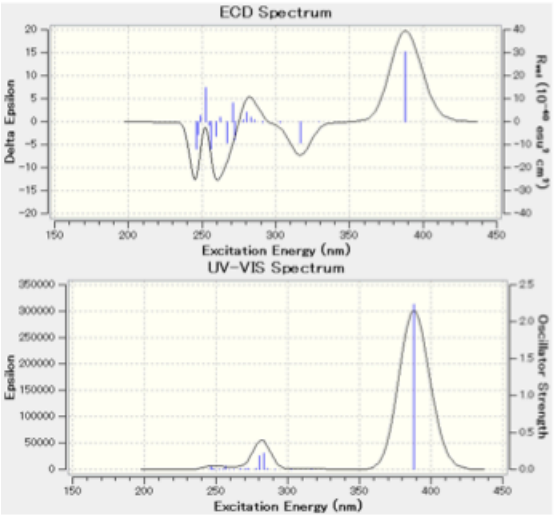


ID19

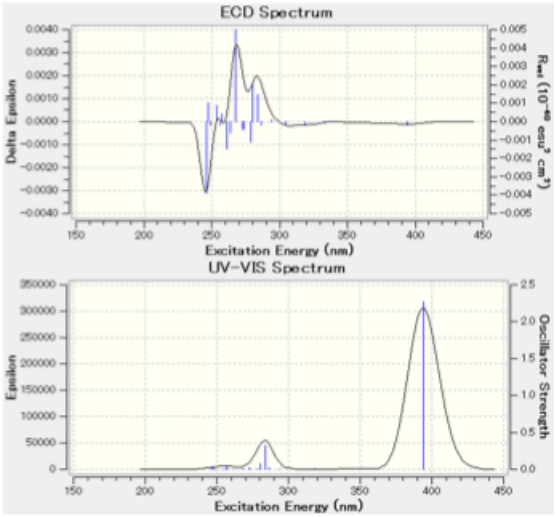


ID20

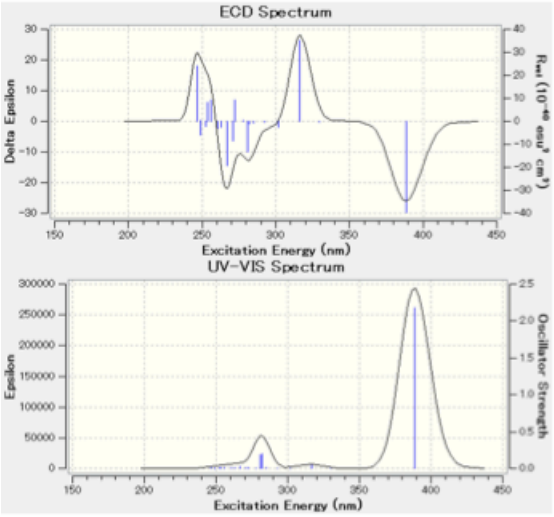


ID21

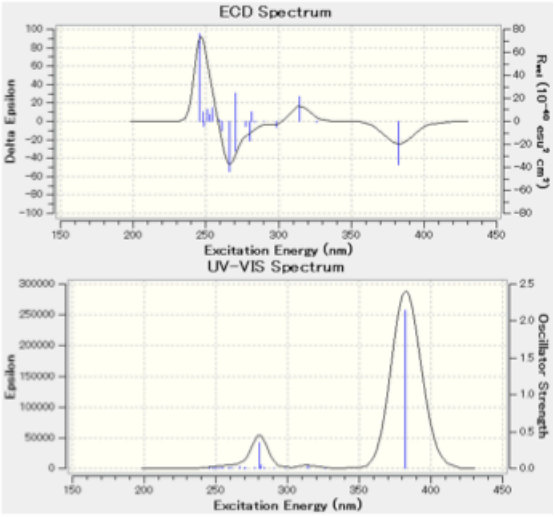


ID22

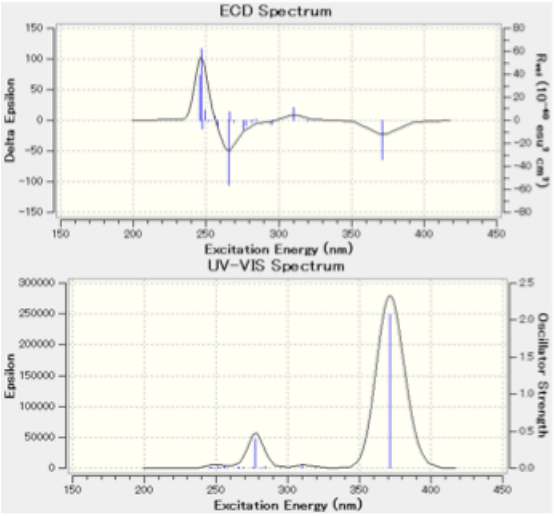


ID23

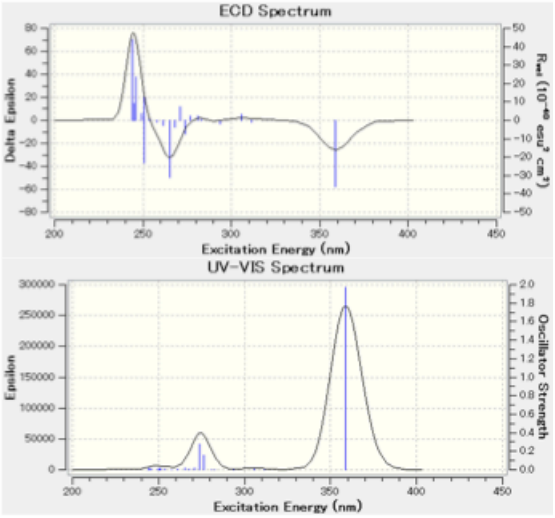


ID24

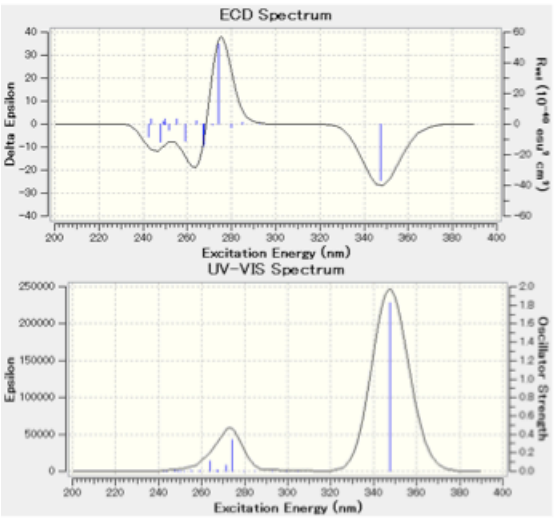


ID25

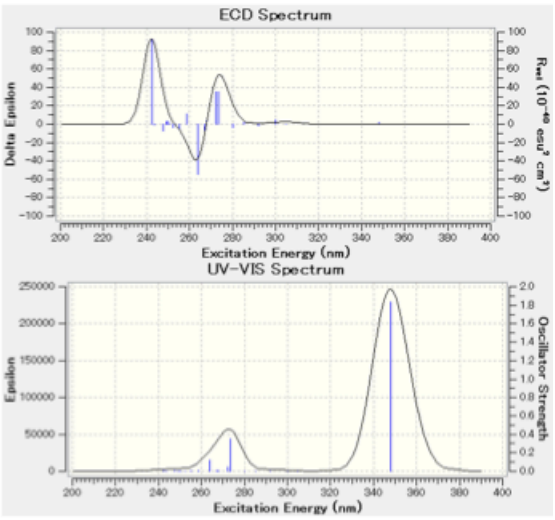


ID26

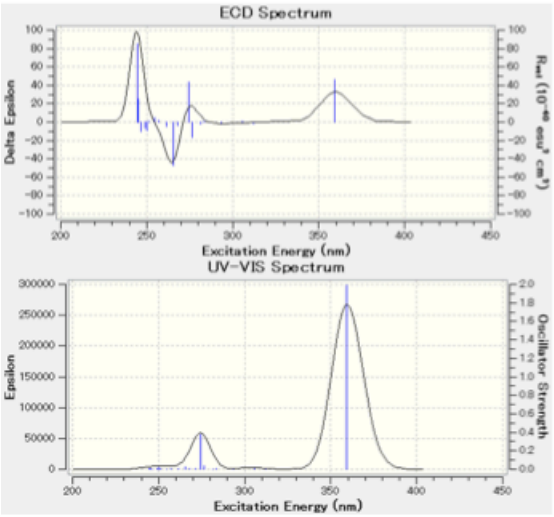


ID27

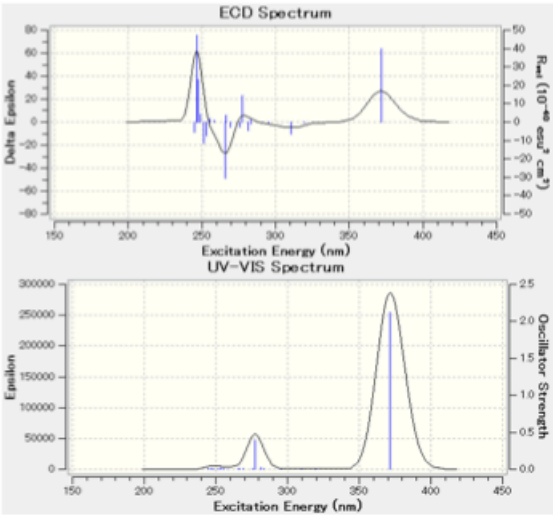


ID28

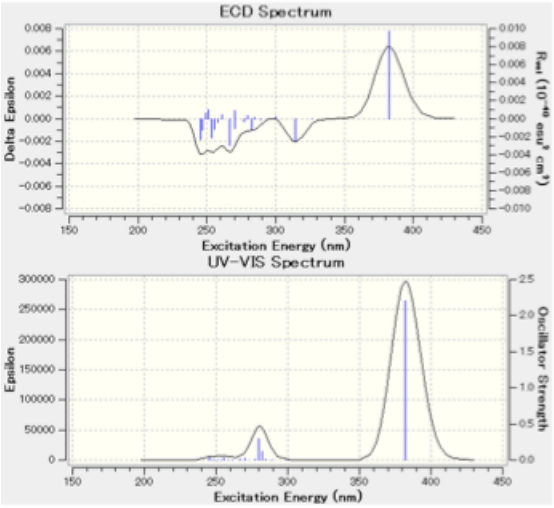


ID29

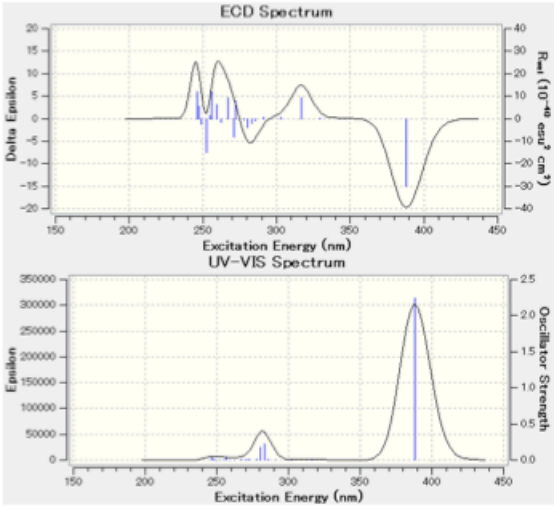


ID30

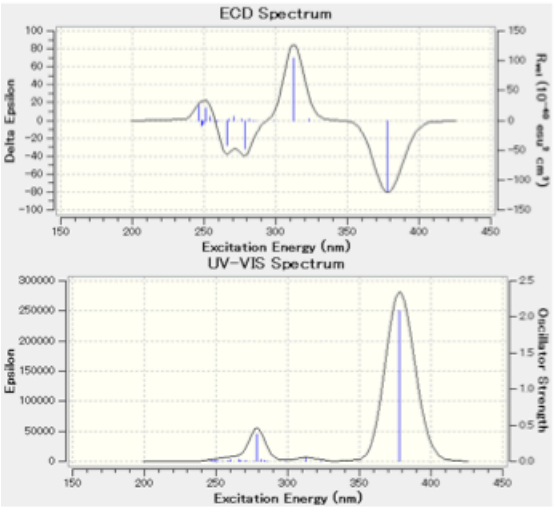


ID31

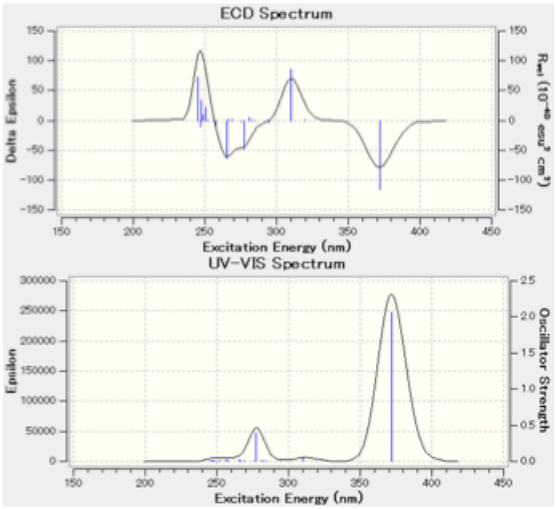


ID32

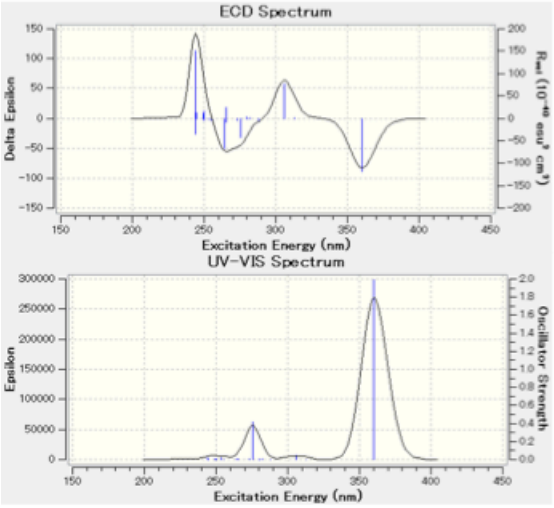


ID33

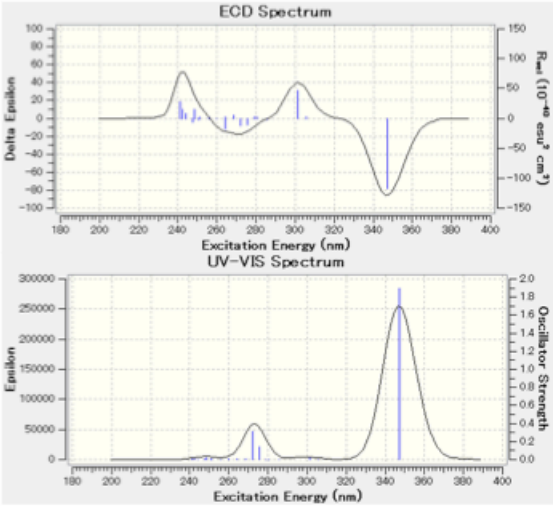


ID34

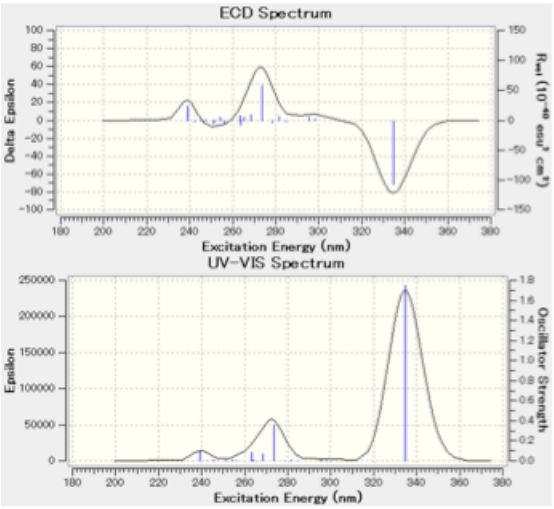


ID35

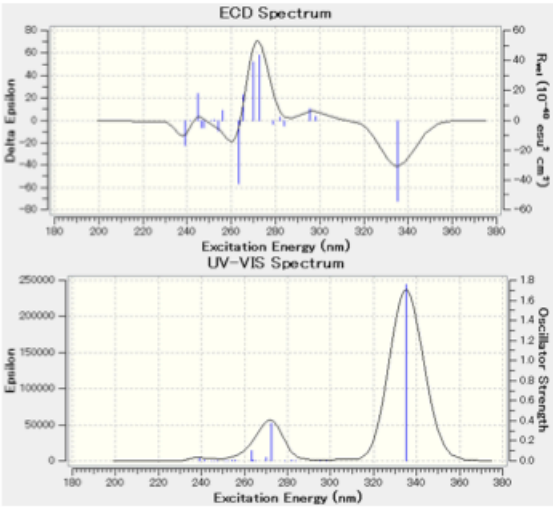


ID36

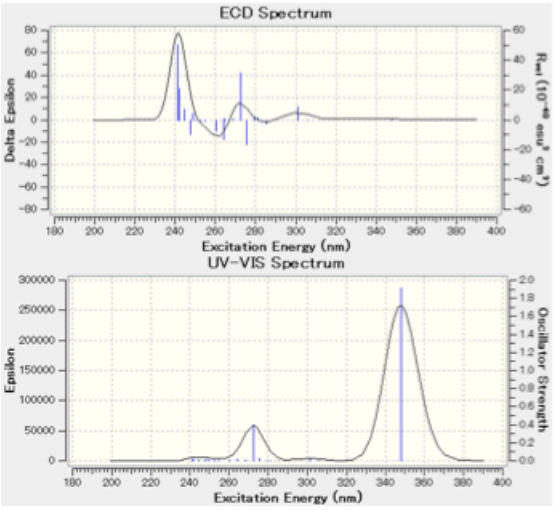


ID37

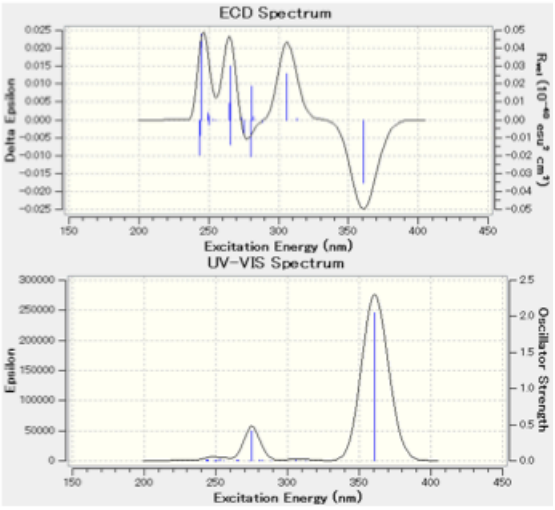


ID38

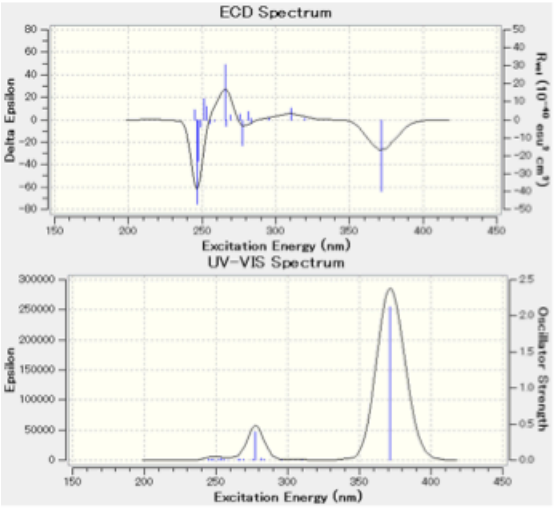


ID39

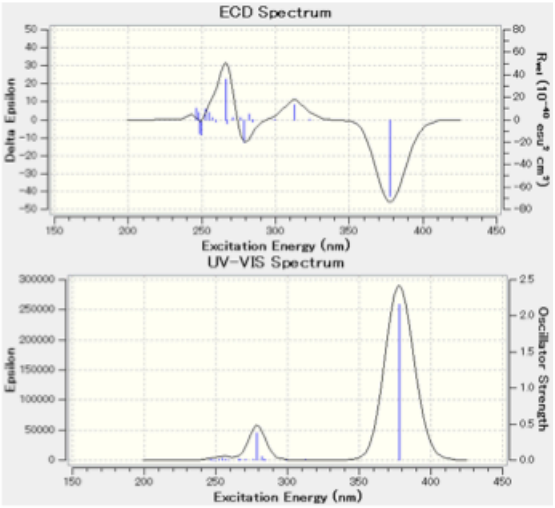


ID40

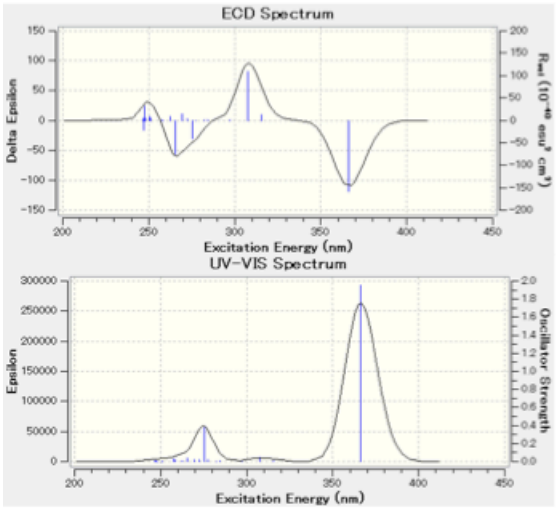


ID41

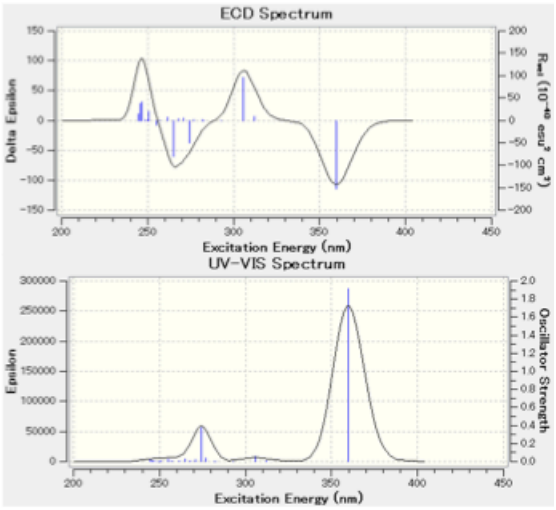


ID42

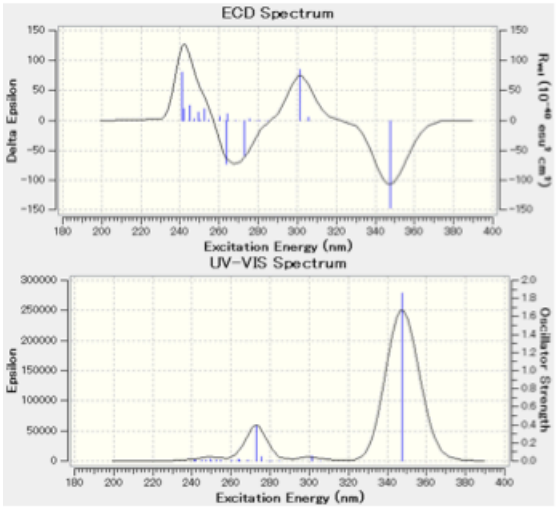


ID43

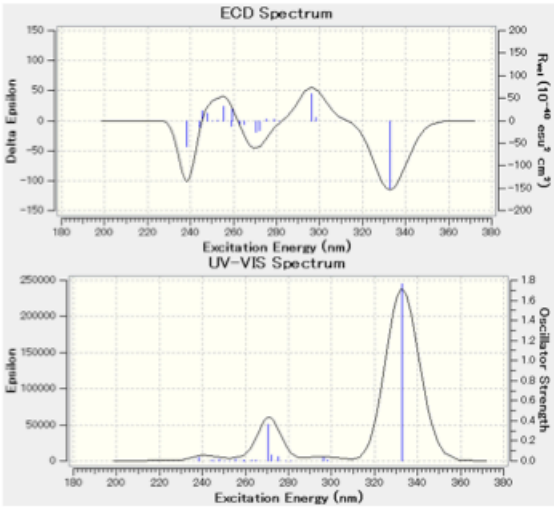


ID44

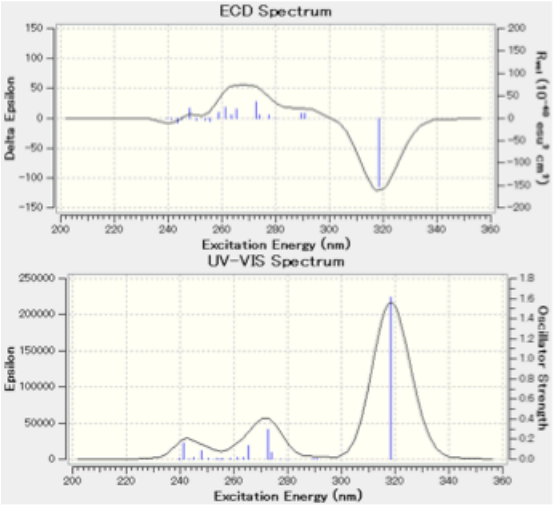


ID45

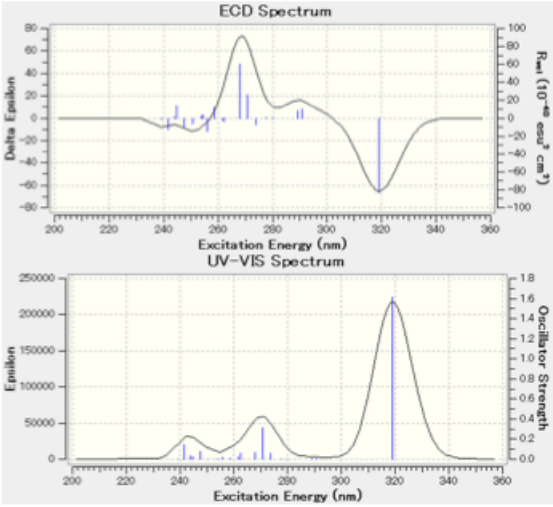


ID46

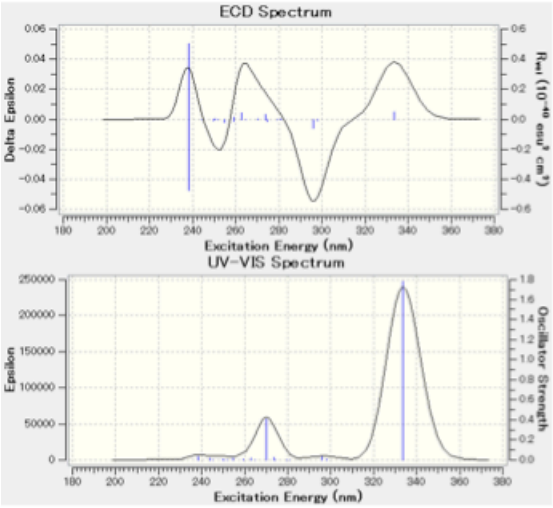


ID47

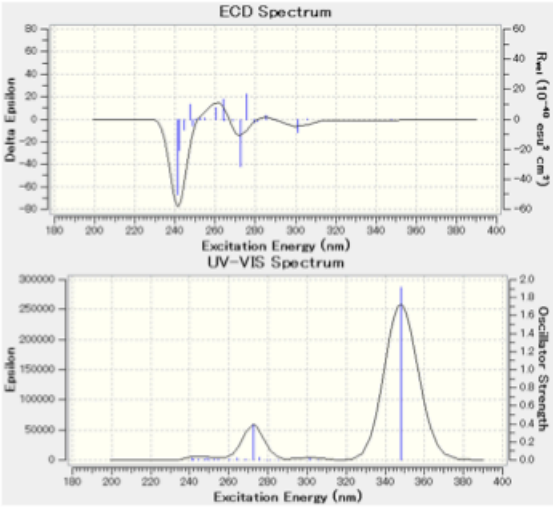


ID48

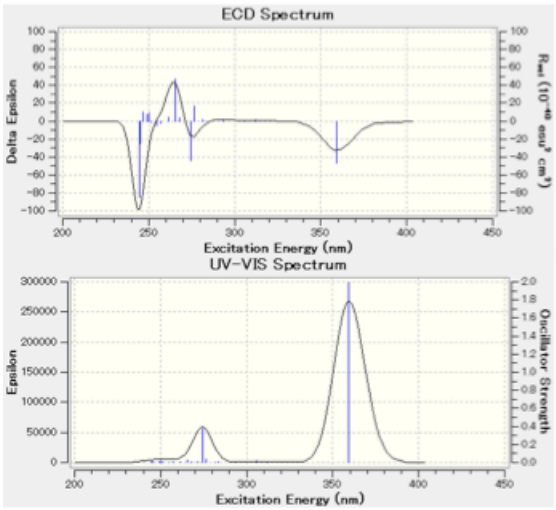


ID49

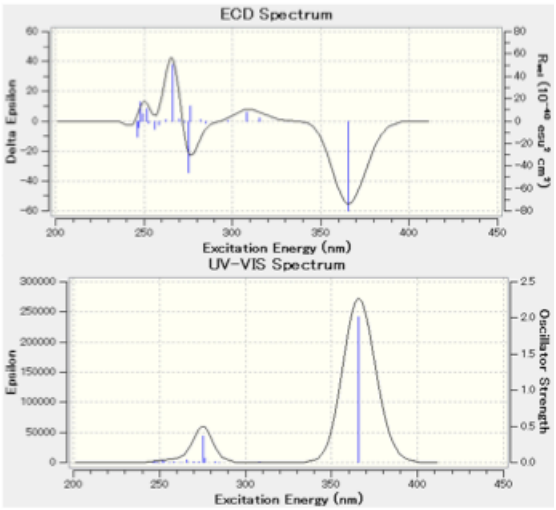


ID50

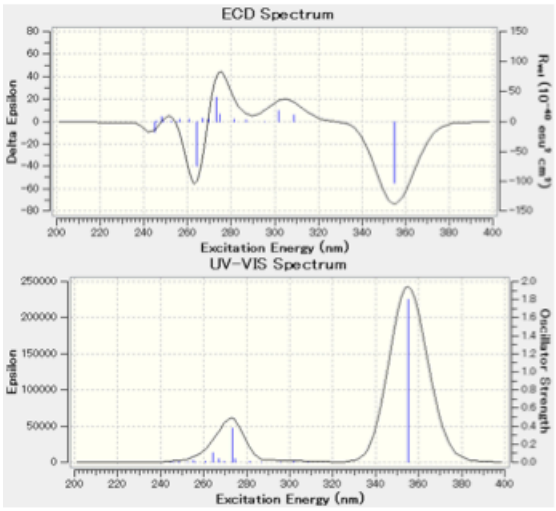


ID51

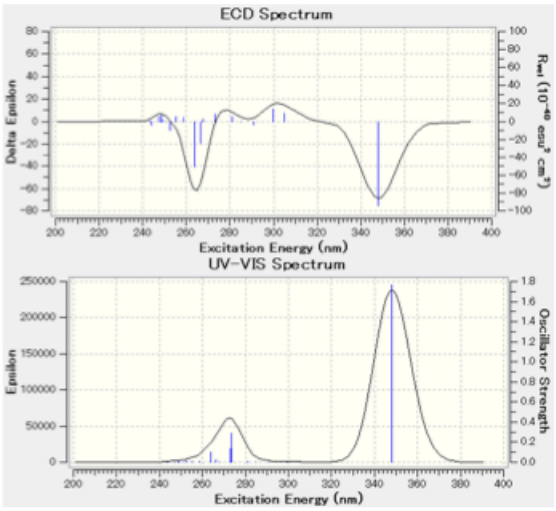


ID52

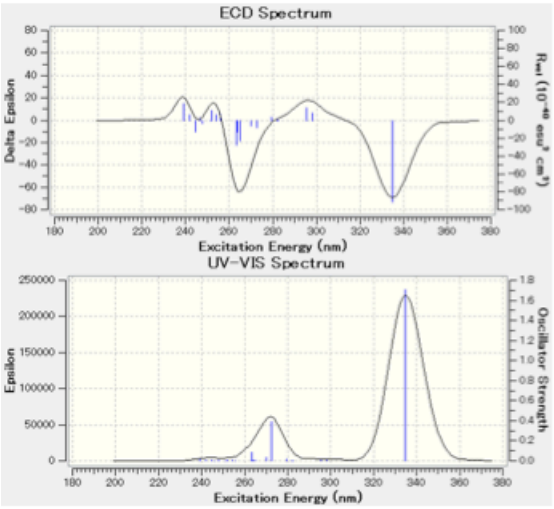


ID53

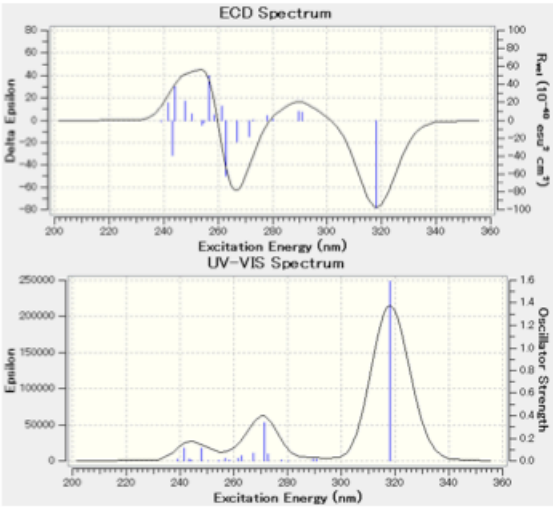


ID54

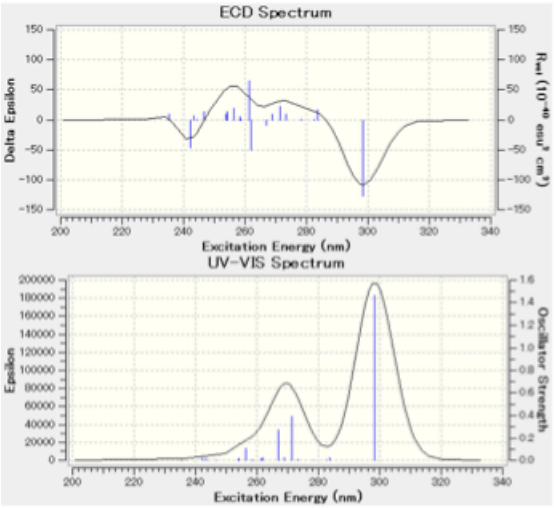


ID55

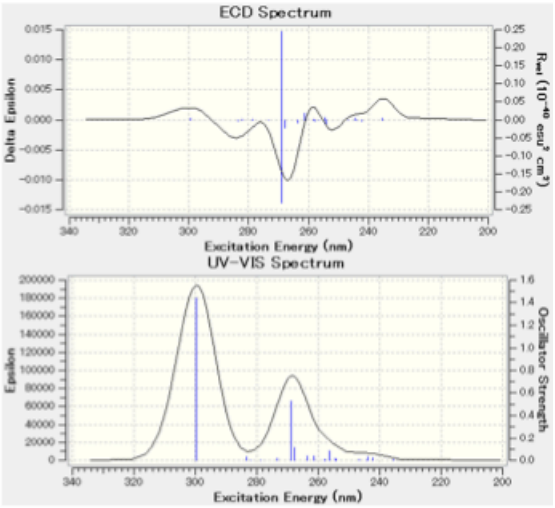


ID56

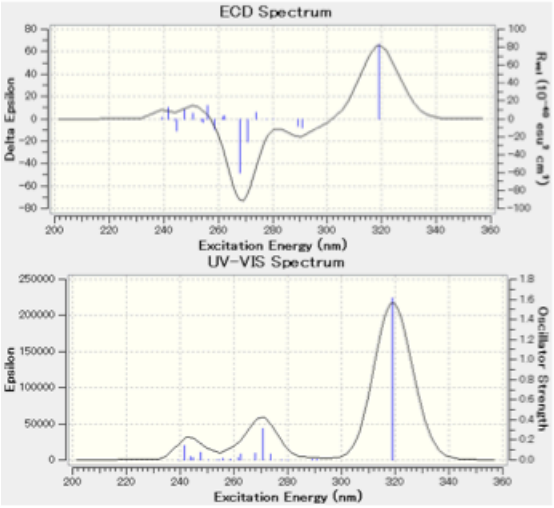


ID57

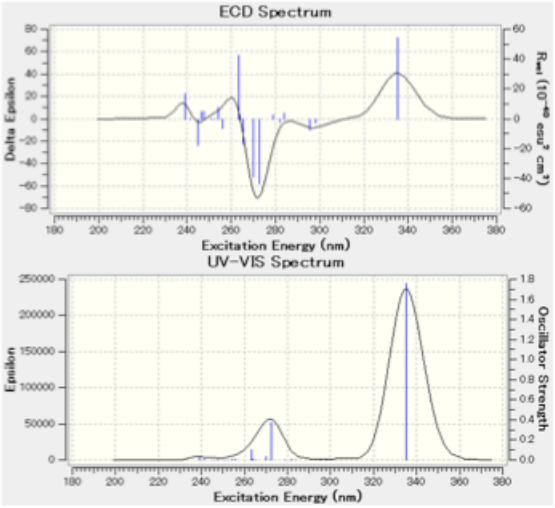


ID58

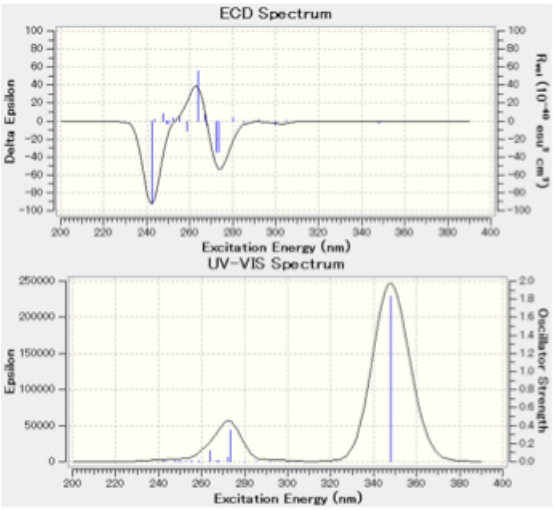


ID59

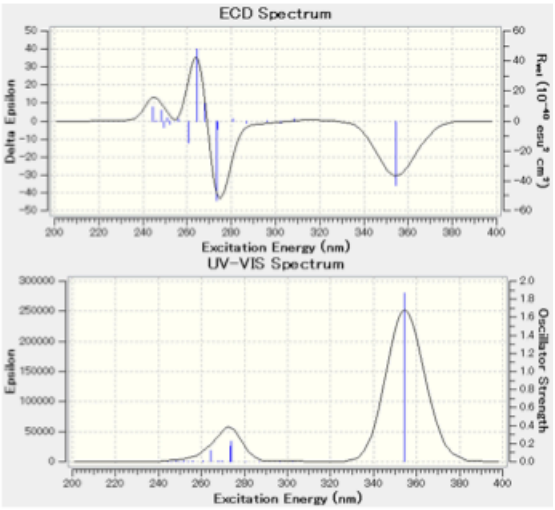


ID60

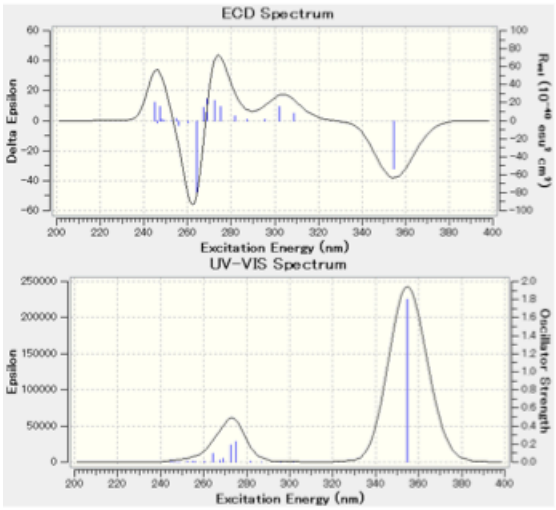


ID61

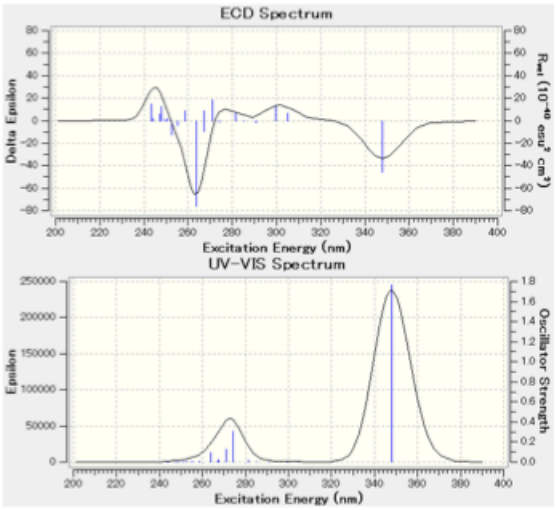


ID62

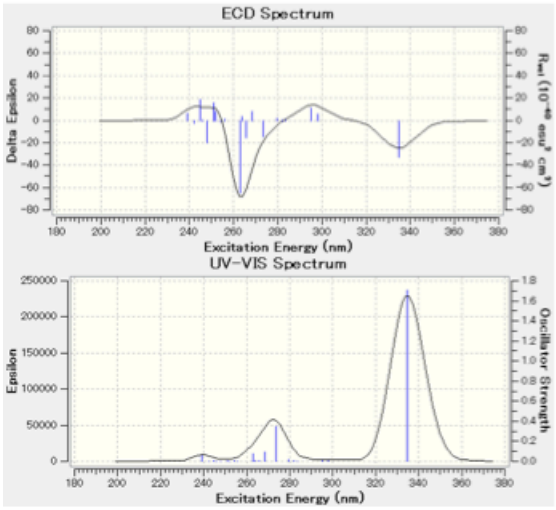


ID63

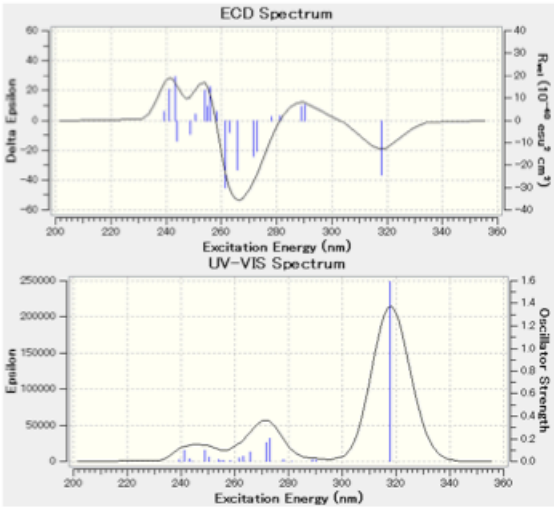


ID64

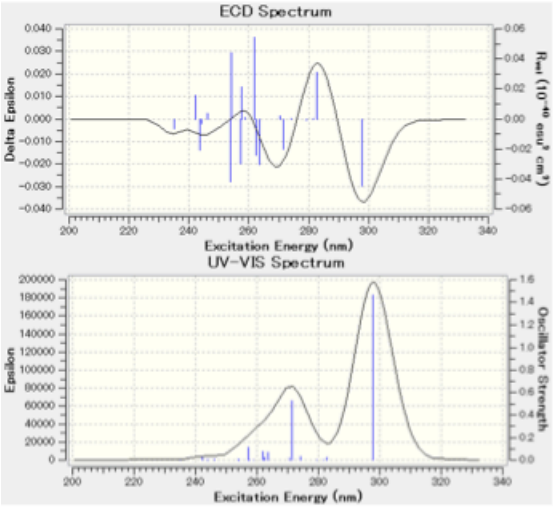


ID65

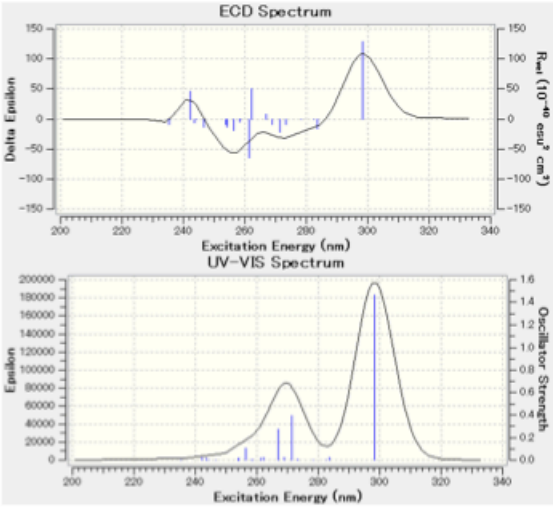


ID66

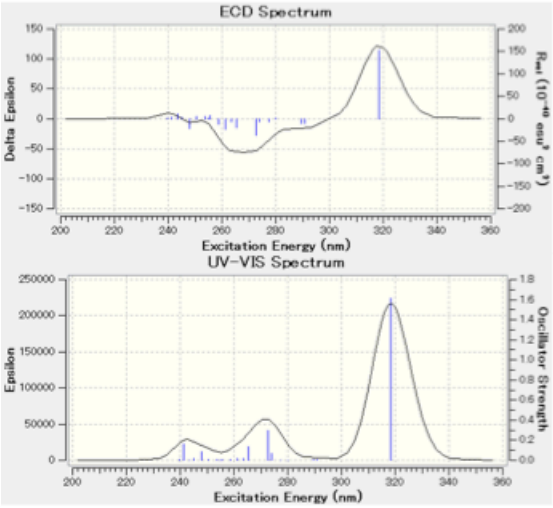


ID67

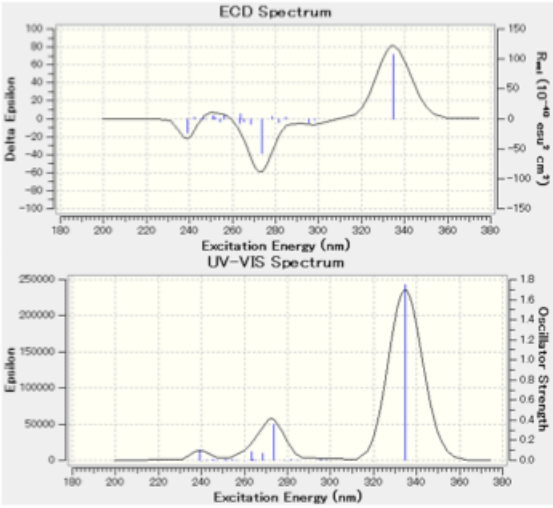


ID68

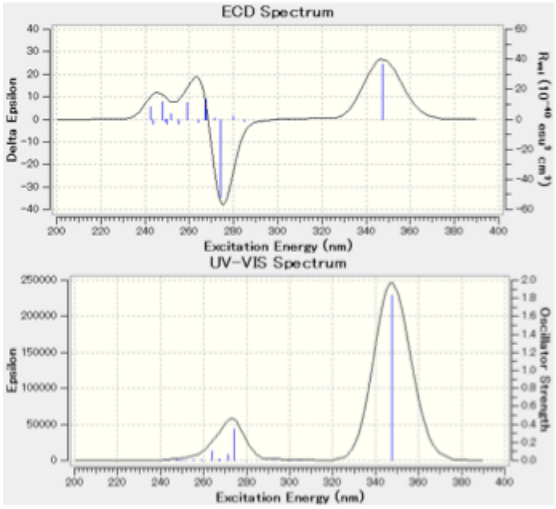


ID69

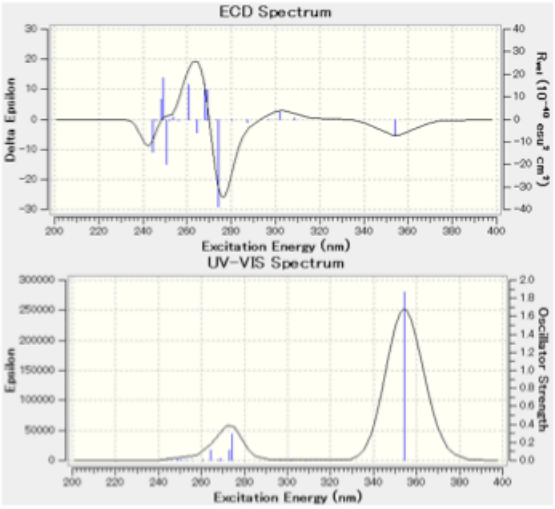


ID70

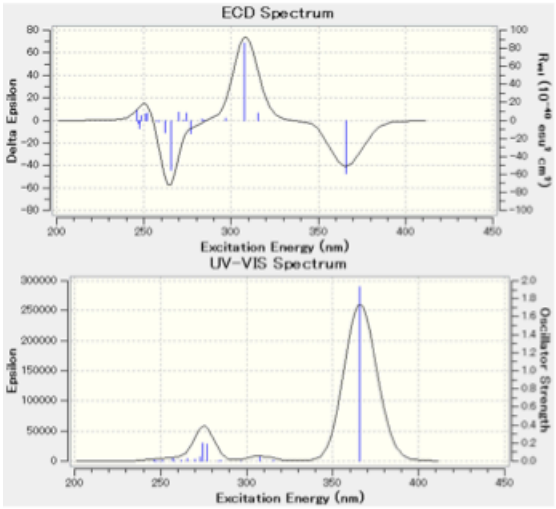


ID71

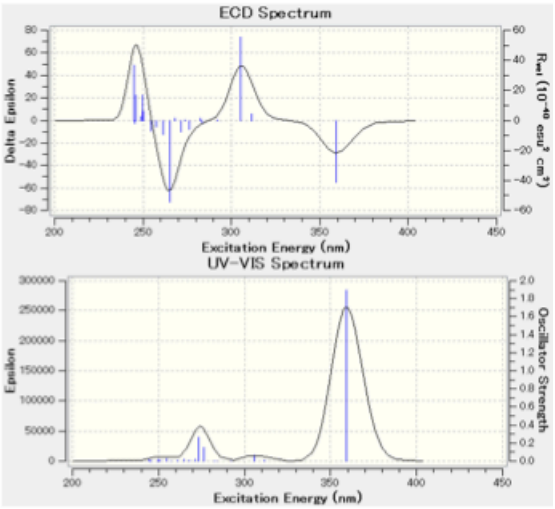


ID72

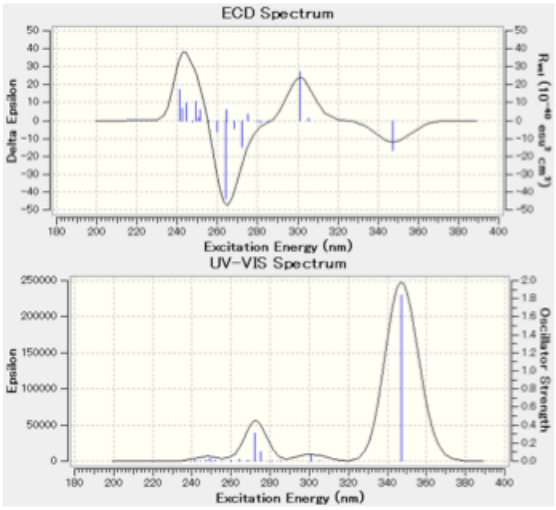


ID73

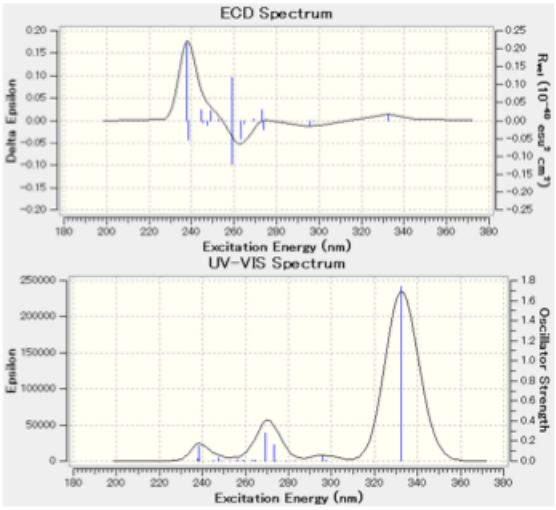


ID74

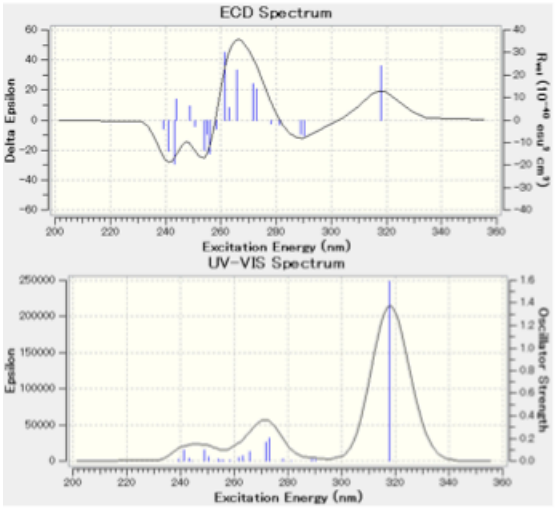


ID75

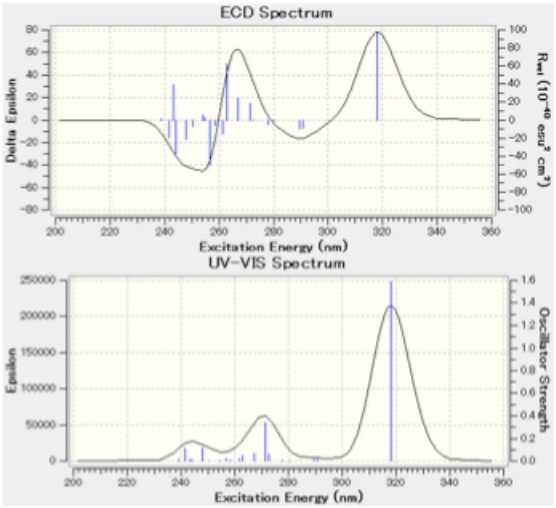


ID76

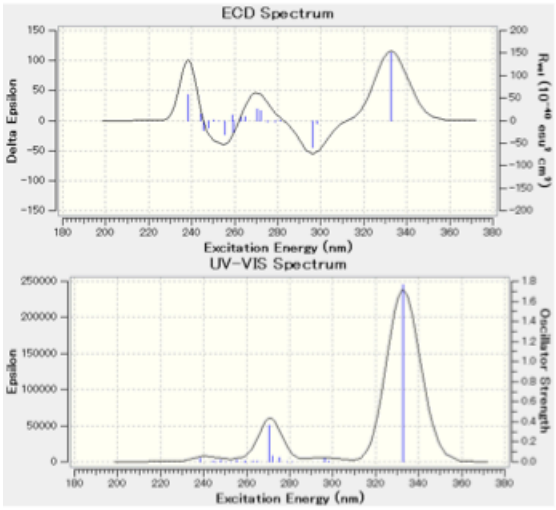


ID77

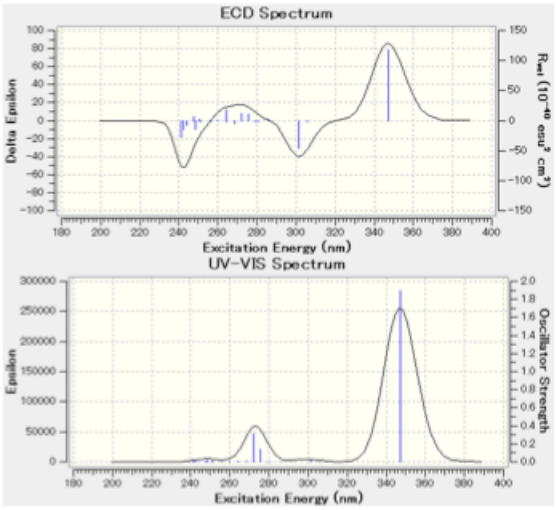


ID78

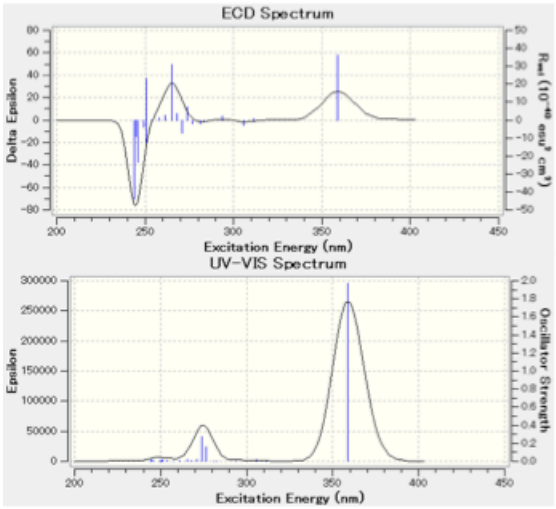


ID79

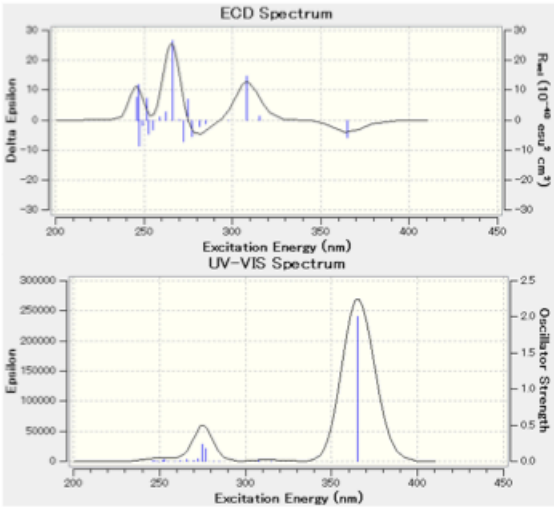


ID80

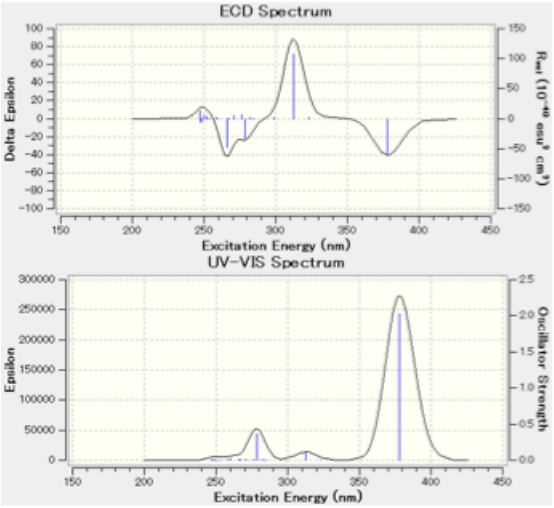


ID81

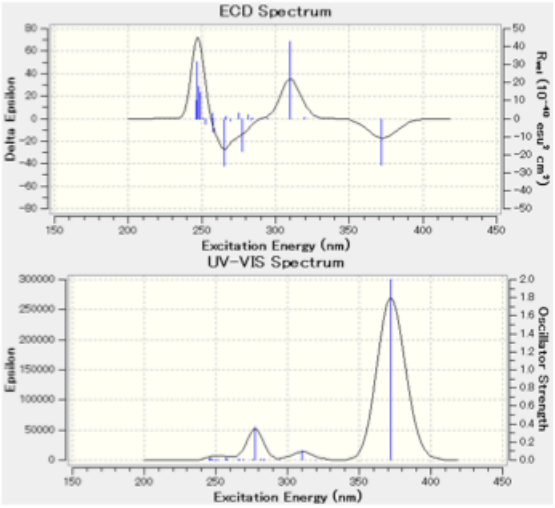


ID82

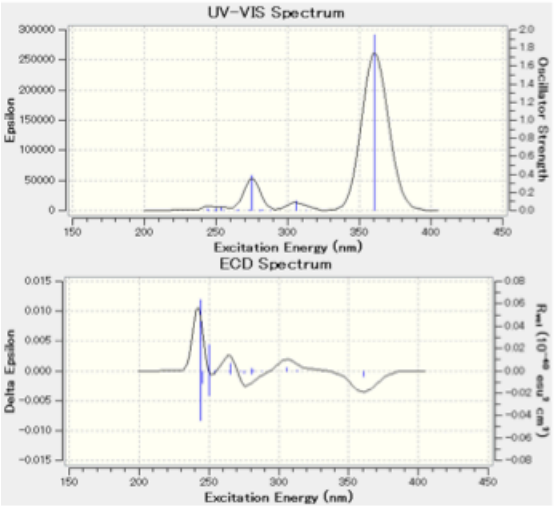


ID83

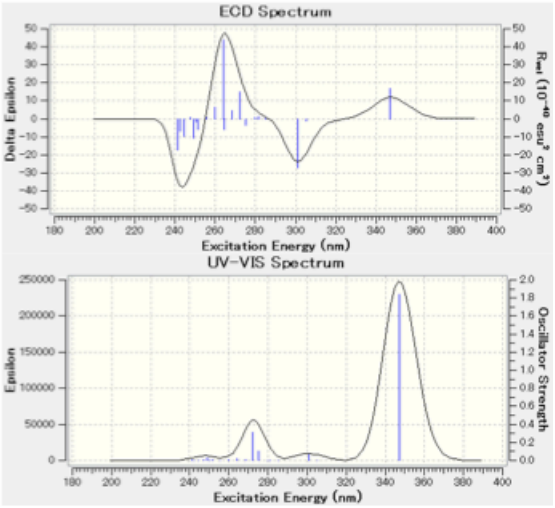


ID84

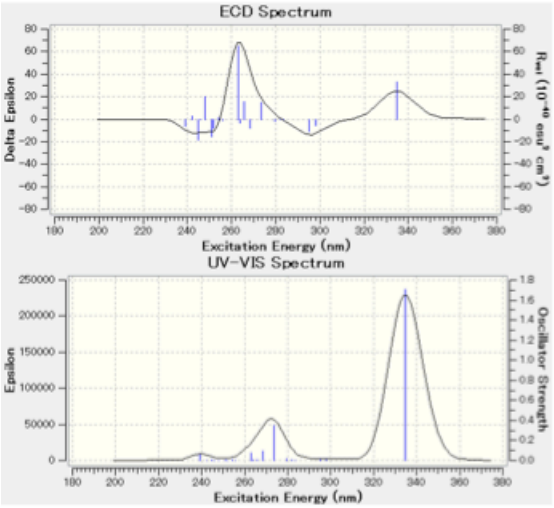


ID85

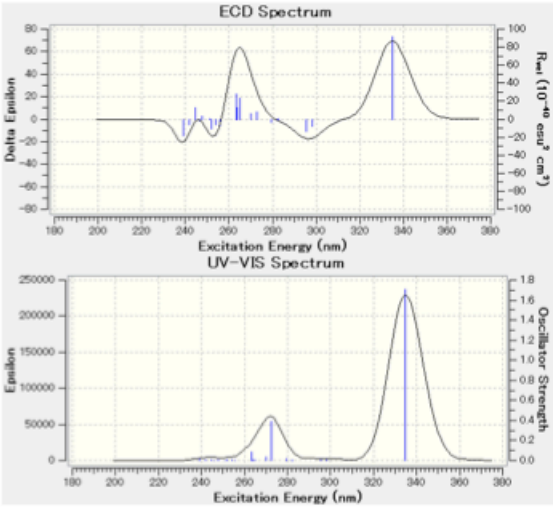


ID86

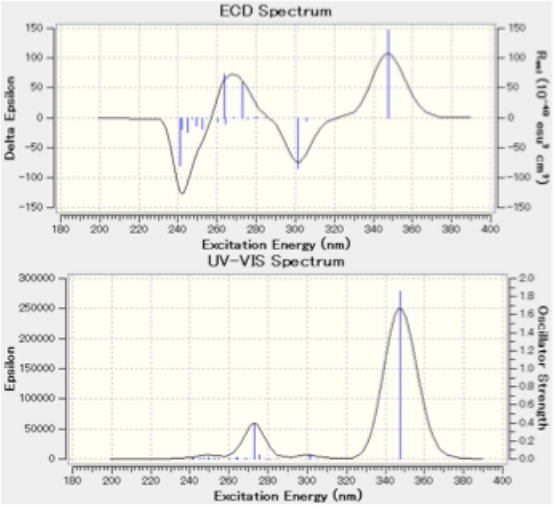


ID87

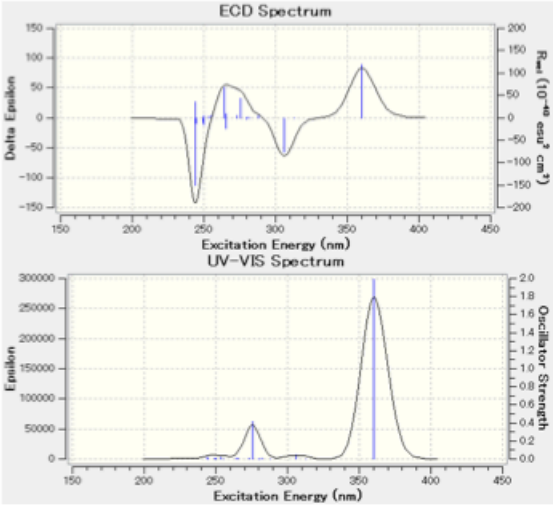


ID88

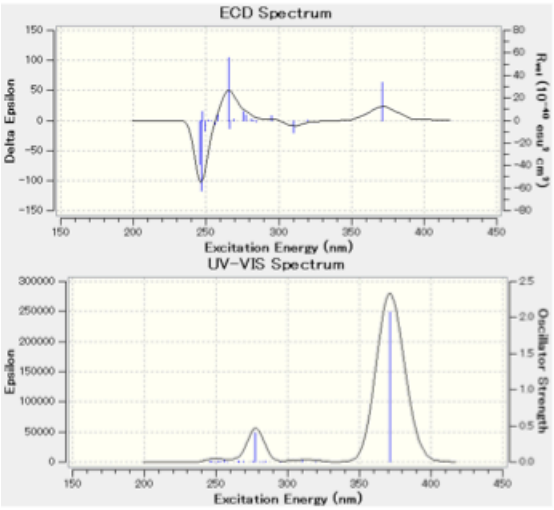


ID89

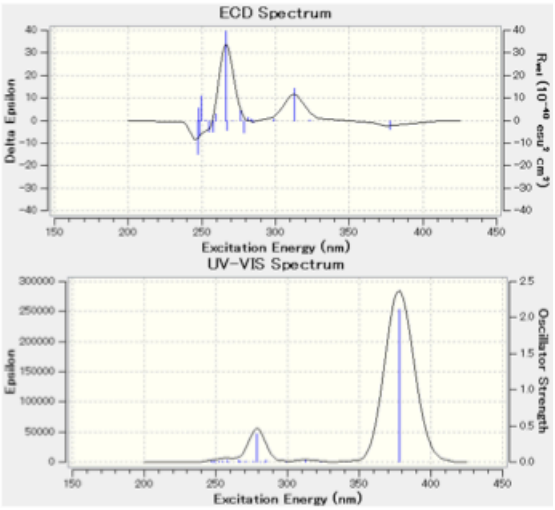


ID90

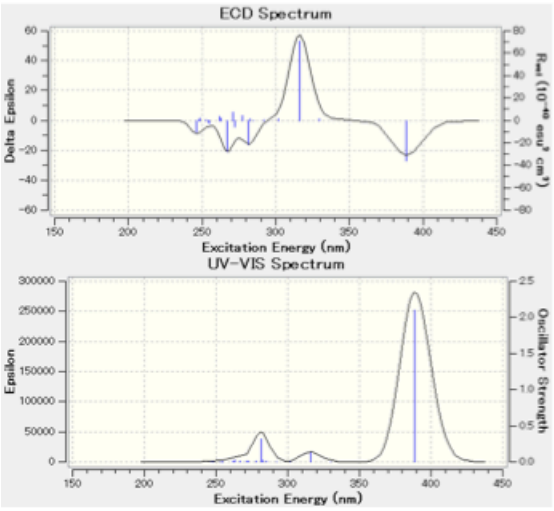


ID91

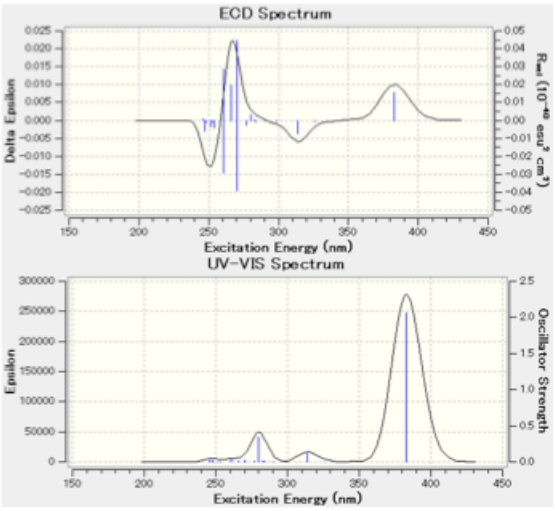


ID92

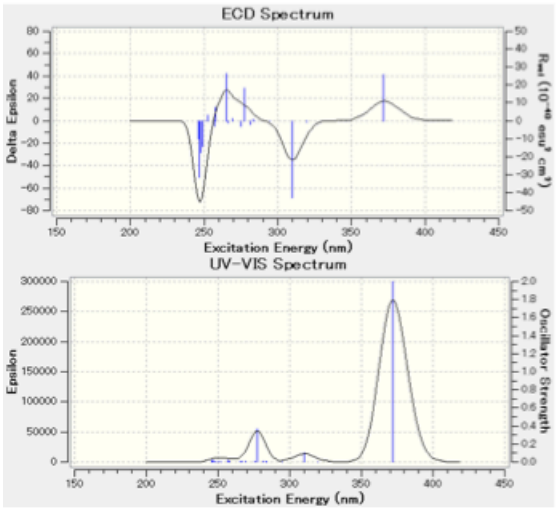


ID93

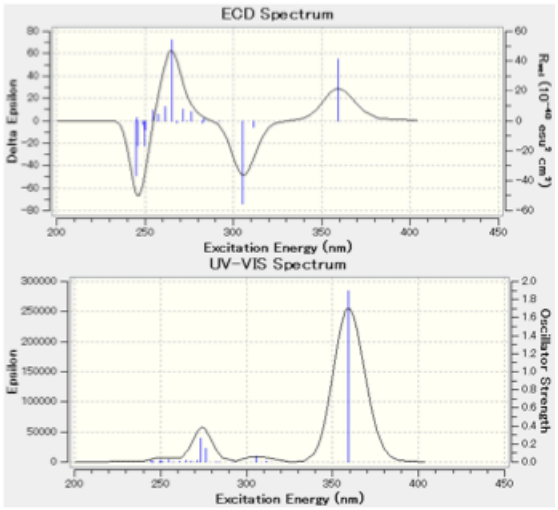


ID94

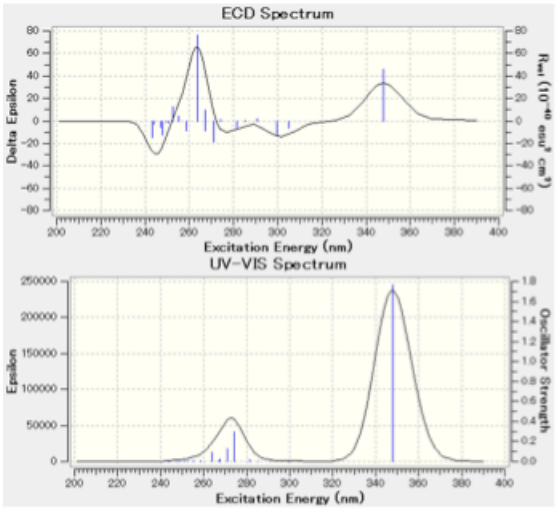


ID95

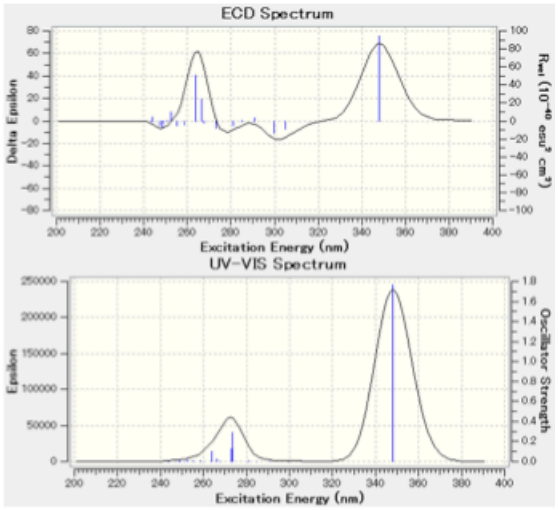


ID96

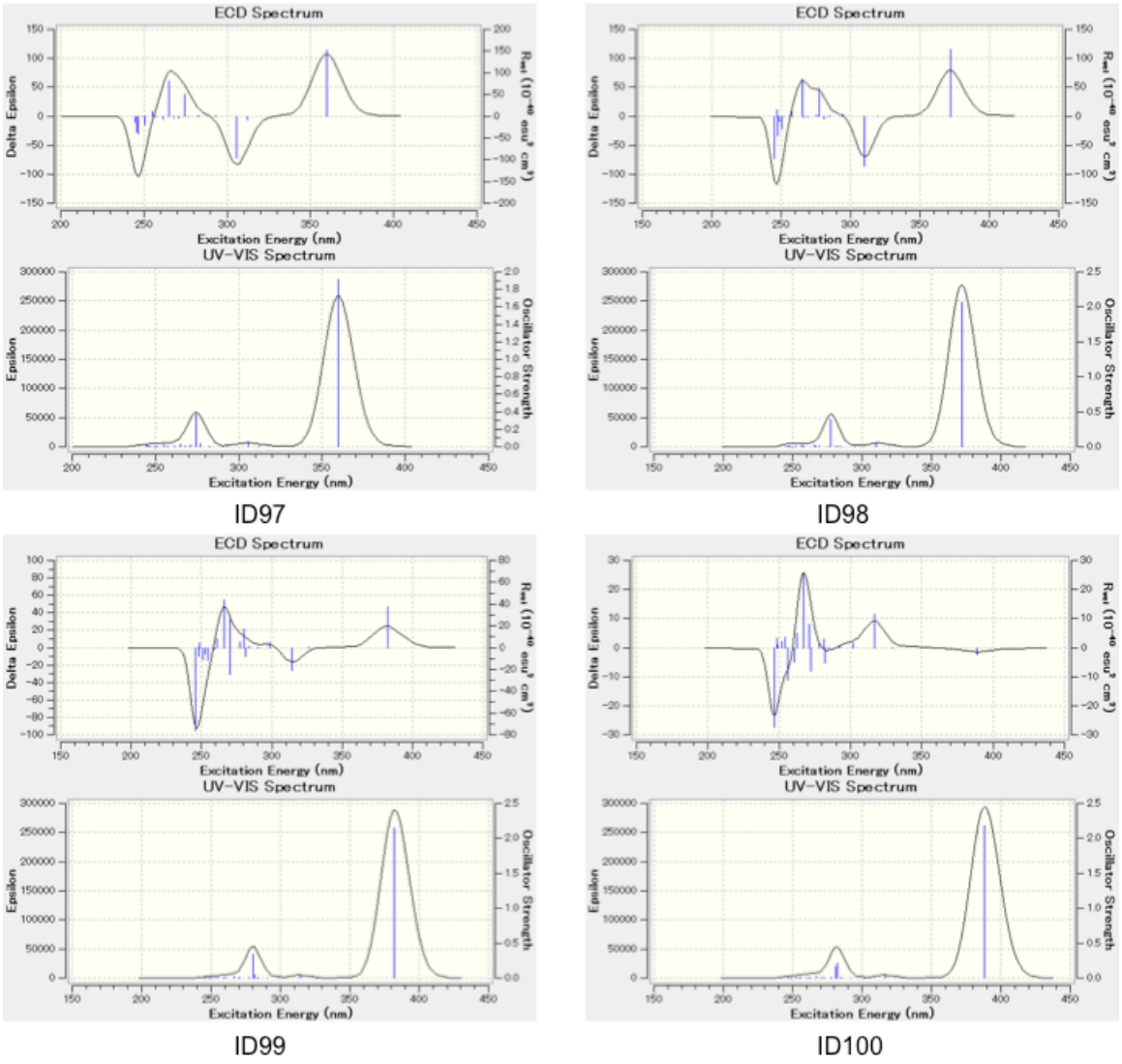


**Figure A14.** Simulated CD and UV-vis spectra of trimer models.

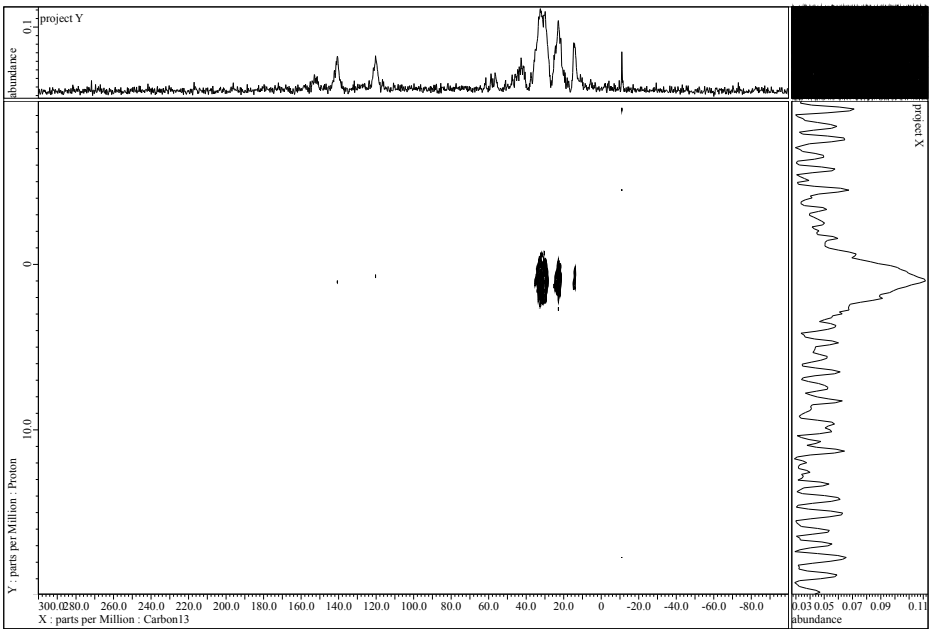


**Figure A15.** The solid-state 2D $^{1}$H-$^{13}$C HETCOR NMR spectrum of **PF8** (proton pulsed, carbon-13 observed).

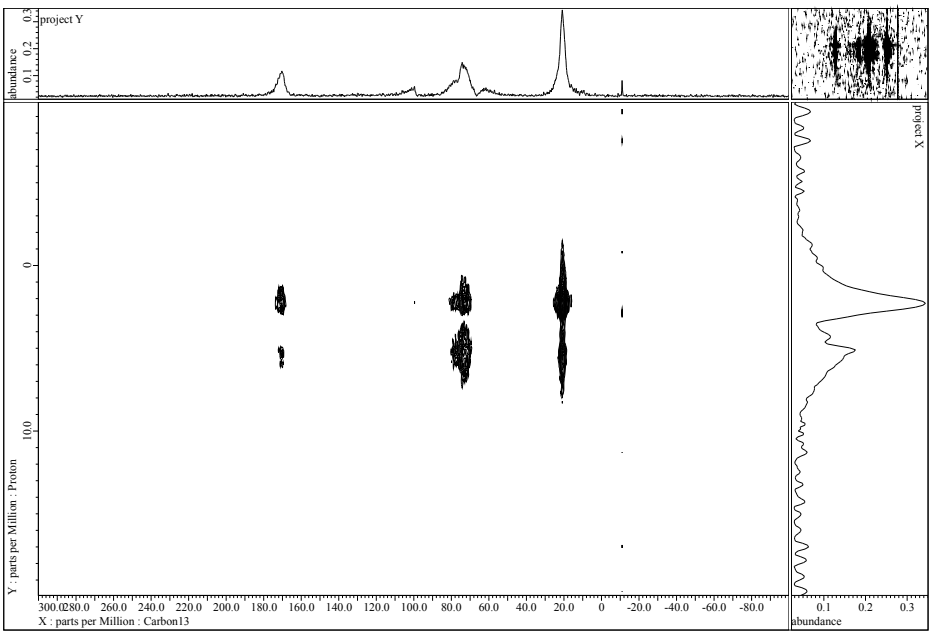


**Figure A16.** The solid-state 2D $^{1}$H-$^{13}$C HETCOR NMR spectrum of **CTA** (proton pulsed, carbon-13 observed).

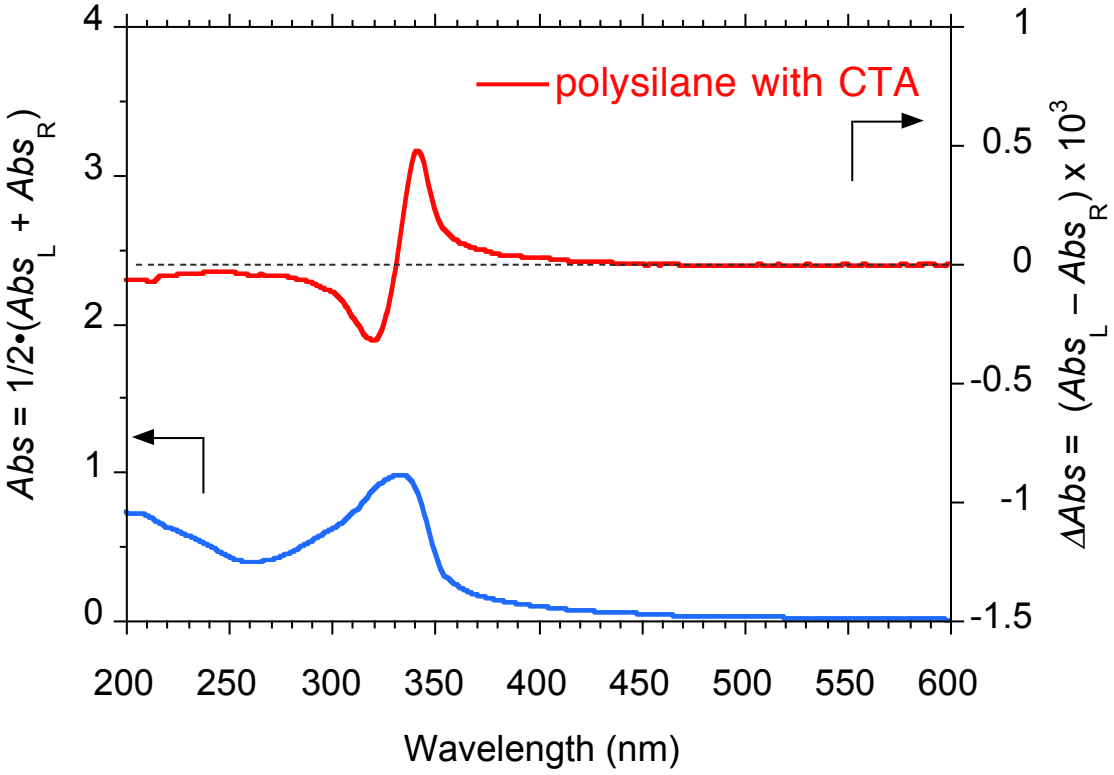


**Figure A17.** Normalized CD/UV-vis spectra of polysilane with **CTA**.

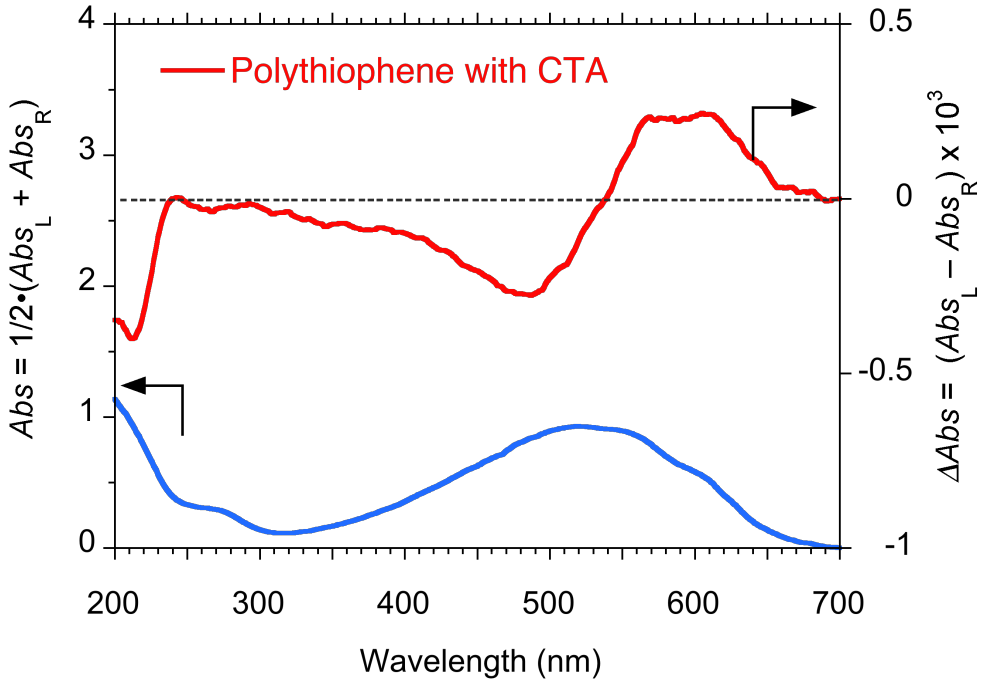


**Figure A18.** Normalized CD/UV-vis spectra of polythiophene with **CTA**.

**List of Publications and Conferences**

1. Sibo Guo, Nozomu Suzuki, and Michiya Fujiki
   Oligo- and polyfluorenes meet cellulose alkyl esters: Retention, inversion, and racemization of circularly polarized luminescence (CPL) and circular dichroism (CD) via intermolecular C-H/O=C interaction.
   *Macromolecules* (ACS), (2017) doi.org/10.1021/acs.macromol.6b02762.
2. Sibo Guo and Michiya Fujiki
   Ambidextrous chirality transfers capability of cellulose triphenylcarbamate to achiral fluorene oligomers and polymer revealed by solvent-induced swapping in CPL and CD signs (in preparation).
3. Tomoyuki Amako, Kazuki Nakabayashi, Nozomu Suzuki, Sibo Guo, Nor Azura Abdul Rahim, Takunori Harada, Michiya Fujiki, and Yoshitane Imai, Pyrene Magic: Chiroptical Enciphering and Deciphering 1,3-Dioxolane Bearing Two Wirepullings to Drive Two Remote Pyrenes.
   *Chemical Communications* (RSC), **51**, 8237−8240 (2015).
4. Kazuki Nakabayashi, Sayaka Kitamura, Nozomu Suzuki, Sibo Guo, Michiya Fujiki, and Yoshitane Imai. Non-Classically Controlled Signs in a Circularly Polarised Luminescent Molecular Puppet: The Importance of the Wired Structure Connecting Binaphthyl and Two Pyrenes.
   *European Journal of Organic Chemistry* (Wiley), 64−69 (2016).
5. Shoma Nakanishi, Kazuki Nakabayashi, Takaya Mizusawa, Nozomu Suzuki, Sibo Guo, Michiya Fujiki, and Yoshitane Imai. Cryptochiral Binaphthyl-bipyrene Luminophores Linked with Alkylene Esters: Intense Circularly Polarised Luminescence, but Ultraweak Circular Dichroism.
   *RSC Advances* (RSC), **6**, 99172−99176 (2016).

**Presented Works**

A. Presentations at International Conferences

1. ○Sibo Guo, Nor Azura Abdul Rahim, Nozomu Suzuki, Michiya Fujiki.
   Luminescent achiral polyfluorene meets chiral surface of cellulose triacetate during co-aggregation process.
   Pacifichem2015 (2015-Dec-17/18, Honolulu, Hawaii, US).
2. ○Nor Azura Abdul Rahim, Sibu Guo, Nozomu Suzuki, Michiya Fujiki.
   Emerging optically active luminescent poly(dioctylfluorene) aggregates by polymer chirality transfer with helical polysilanes
   Pacifichem2015 (2015-Dec-17/18, Honolulu, Hawaii, US).
3. ○Michiya Fujiki, Abd Jalil Jalilah, Nor Azura Abdul Rahim, Sibo Guo, Nozomu Suzuki.
   Chiroptically enhanced luminescent p-conjugated polymer aggregates in controlled optofluidic medium.
   Pacifichem2015 (2015-Dec-17/18, Honolulu, Hawaii, US).

B. Presentations at Domestic Conferences

1. ○郭思博・藤木道也

   第 63 回高分子学会年会, 口頭, 2014, 5/28-5/30, 名古屋

**Acknowledgements**

First of all, I would like to extend my sincere gratitude to my supervisor, Prof. Michiya Fujiki for his instructive advice and useful suggestions on my thesis. His deep knowledge in the field of polyfluorene, chirality transfer, and spectroscopy broadened my ideology in science. Without his consistent and illuminating instruction, this thesis could not have reached its present form. I am deeply grateful of his help in the completion of this thesis.

I also acknowledge other faculty advisors in Nara Institute of Science and Technology (NAIST). My gratitude to Prof. Masao Tanihara who offered valuable advises on the direction of the research. His questions were great valuable and led me to new ideas to explain the experimental results. I am also thankful to Prof. Hiroko Yamada for her kind suggestion that was not limited to my confronting obstacle but also noted the potential future problems. I extend my gratitude also to Prof. Jun-ichi Kikuchi, who kindly responded when I had difficulty in formulating theoretical calculation method of my work. His valuable comments have strengthened my research emphasis.

I am also thankful to talented technical staffs in NAIST. I am thankful to Fumio Asanoma who helped me with the measurement using 1D-NMR, and 2D-NMR such as HETOCOR, HMQC, and CP-MAS $^{13}C$ NMR. Not only the measurement but also the discussion about my research was beneficial to verify hypothesis.

I am also thankful to Dr. Nozomu Suzuki, who was graduated from NAIST and moved to Rikkyo University as an assistant professor. He was a good senior student and he suggested not only about my research but also how to develop the career as a PH. D. student.

I am also thankful to the members of the Advanced Polymer Science Laboratory, including students who have already graduated from NAIST. Not only our laboratory

discussions but also for the enjoyable time we spent outside the laboratory.

Finally, I appreciate the support from my relatives. Especially I thank my wife, Meinan Zhao. I will always admire your patience and considerateness to take care of our life.

February 2017

Sibo Guo